A STUDY OF LOW-FREQUENCY DUCT NOISE CONTROL BASED ON HELMHOLTZ RESONATORS IN THE PRESENCE OF GRAZING FLOW

XUE RONG

PhD

The Hong Kong Polytechnic University

2025

The Hong Kong Polytechnic University

Department of Building Environment and Energy Engineering

A study of low-frequency duct noise control based on Helmholtz resonators in the presence of grazing flow

Xue Rong

A thesis submitted in partial fulfillment of the requirements for the

Degree of Doctor of Philosophy

December 2024

CERTIFICATE OF ORIGINALITY

I hereby declare that this thesis is my own work and that, to the best of my knowledge and belief, it reproduces no material previously published or written, nor material that has been accepted for the award of any other degree or diploma, except where due acknowledgement has been made in the text.

(Signed)

Xue Rong (Name of Student)

Abstract

The ventilation ductwork system has become an important part of modern buildings that maintain good indoor air quality. However, transmission noise from a ventilation fan and flow-generated noise from the interaction of moving air and duct flow discontinuities are unavoidable. While the commonly used duct noise silencer can effectively reduce medium to high-frequency noise over a broadband frequency range, low-frequency noise control still remains a challenge to most engineers. The Helmholtz resonator (HR), with simple geometric structures and easy to manufacture and maintain, has become an effective strategy for low-frequency noise attenuation. In the present study, the low-frequency noise attenuation performance of silencers based on HRs in the presence of grazing flow is investigated.

In the first part of this thesis, a dual HR system is designed by connecting a pair of HRs in series (neck-cavity-neck-cavity). The influence of neck length, cavity volume, and flow Mach number on the noise attenuation performance of a dual HR system is investigated. A three-dimensional numerical simulation is implemented to calculate the transmission loss results. The transmission loss (TL) results show the second neck length can influence the second resonance frequency and the TL peak. Changing the cavity volume will significantly influence the noise attenuation ability under lower flow rate conditions than the higher flow rate conditions. The flow field results show that air only enters the first neck and cavity. The flow Mach number has a more significant impact on the first TL peak than on the second TL peak.

In the second part of this thesis, the acoustic behavior of the HR model in the presence of grazing flow is investigated experimentally. The four-microphone method is performed to measure the transmission loss performance of the resonator model under flow speeds of 0-20 m/s, and the particle image velocimetry (PIV) measurement is adopted to evaluate the fluid characteristics of the resonator neck. The flow effect on the acoustic performance of the resonator model is derived by using the curve fit technique. An empirical model is established to predict the transmission loss of the Helmholtz resonator in the presence of the grazing flow. The empirical model is added to the transfer matrix method to predict the transmission loss of the period Helmholtz resonator model under different grazing flow speeds. The PIV experiment results reveal the fluid dynamics in the neck region of the resonator model.

In the third part of this thesis, a lightweight and compact sound-absorbing metamaterial-based Helmholtz Resonator Array (HRA) that exhibits broadband low-frequency noise attenuation performance even under low-speed flow conditions is presented. A semi-empirical theoretical model is developed by integrating Guess's empirical model with a flow correction term to predict the transmission loss performance of the designed HRA under various grazing flow velocities. The designed HRA is composed of 8 single Helmholtz resonator models and is optimized to increase the noise attenuation band. Results show that the designed HRA can achieve around 20 dB/m in the prescribed frequency range of 200 to 800 Hz under grazing flow speeds of 0-20 m/s, and the proposed theoretical model can accurately predict transmission loss performance under different grazing flow speeds. The design strategy of the HRA model offers an effective solution for noise reduction in ventilation duct systems.

Publications from the Thesis

Published papers

Rong Xue, Cheuk Ming Mak, Chenzhi Cai, Kuen Wai Ma, "An infinity tube with an expansion chamber for noise control in the ductwork system", (2023), 305, 23, *Sensors*.

Rong Xue, Cheuk Ming Mak, Dizi Wu, Kuen Wai Ma, "The acoustic performance of a dual Helmholtz resonators system in the presence of a grazing flow", (2023), 22(1-2), 23-40, *International Journal of Aeroacoustics*.

Conference papers

Rong Xue, Cheuk Ming Mak, Chenzhi Cai, Kuen Wai Ma, "A periodic infinity tubes array VS a periodic Helmholtz resonators array", *2022 International congress on acoustics*, Gyeongyu, Korea, 183-190(A03).

Rong Xue, Cheuk Ming Mak, Chenzhi Cai, Kuen Wai Ma, "Design of an instrumentation system for assessing the acoustic attenuation performance of ducted Helmholtz resonators in the presence of grazing flow", *Inter-Noise 2023*, Chiba, Japan, 785-791(7).

Paper under review

Rong Xue, Cheuk Ming Mak, Chenzhi Cai, Kuen Wai Ma, "Sound transmission performance of the periodic Helmholtz resonator array in the presence of grazing flow", *Applied Acoustics* (Under review).

Rong Xue, Cheuk Ming Mak, Chenzhi Cai, Kuen Wai Ma, "Broadband low-frequency noise attenuation performance of a Helmholtz Resonator Array (HRA) in the presence of grazing flow", *Thin-Walled Structures* (Under review).

Acknowledgements

This thesis is the results from my work supported by the financial from the Research Grants Council of the Hong Kong Special Administrative Region, China (Project No. 15207820).

I would like to express my deepest appreciation to my supervisor, Prof. Mak Cheuk Ming, for his invaluable guidance, support, and encouragement throughout my research journey. His critical insights and dedication to research have inspired me a lot, not only in this study but also in my personal life.

I would like to express my thanks to all the members in the Indoor Environmental Quality Laboratory and my friends for their assistance and company during my study and my life. The discussions and shared experiences between them have enriched my academic journey. I would also like to thank all the staff and technicians of the Department of Building Environment and Energy Engineering, for their support and guidance during my experimental work.

Finally, I would like to express my heartfelt gratitude to my family. Your support and encouragement have been a guiding light throughout this journey.

Table of Contents

List of Figures

List of Tables

Nomenclature

Symbol	Description
c	Sound speed of air
C_α	Sound absorption capacity
e	Euler's number
f_0	Resonance frequency of HR in the absence of background flow
f^*	Non-dimensional frequency
f_r	Resonance frequency of HR in the presence of grazing flow
j	Imaginary unit
H_{ab}	Complex transfer function between positions *a* and *b*
H_{ij}	Complex transfer function from the *i*-th channel to the *j*-th channel
$\mathbf{I}$	Identity matrix
k_0	Acoustic wave number
k^+	Wave number of the incident acoustic wave
k^-	Wave number of the reflected acoustic wave
L	Length of the duct between each HR model
l_c	Cavity side length
l_n	Neck length
l'_n	Neck length with end correction
Ma	Flow Mach number
M_0	Dimensionless particle velocity at the neck region
P	Acoustic pressure

P_0	Mean background flow pressure
P_1	Acoustic pressure at position 1
P_2	Acoustic pressure at position 2
P_i	Pressure amplitudes of the incident acoustic wave
P_r	Pressure amplitudes of the reflected acoustic wave
P_t	Pressure amplitudes of the transmitted acoustic wave
R_0	Acoustic resistance
r	Reflection coefficient
r_c	Cavity radius
r_n	Neck radius
s	Distance between two microphones
S_c	Cross-sectional area of the cavity
S_{ii}	Auto-spectrum of the *i*-th channel
S_{ij}	Cross-spectrum between the *i*-th channel and the *j*-th channel
S_n	Cross-sectional area of the neck
t	Wall thickness
T_0	Mean background flow temperature
$\mathbf{T}_{\mathrm{all}}$	Transfer matrix of all section
$\mathbf{T}_{\mathrm{duct}}$	Transfer matrix of the duct section between each HR model
TL	The sound transmission loss
TL/L	Sound transmission loss per unit length
TL_{Array}	Transmission loss of a periodic HR array
u	Acoustic velocity

$\boldsymbol{u}_0$	Mean background flow velocity
U	Background flow speed
U_{max}	Maximum flow velocity
$V1$	Volume of the first cavity
$V2$	Volume of the second cavity
V_c	Cavity volume
V_{max}	Maximum velocity of velocity profile
X_0	Acoustic reactance
y^*	Non-dimensional y position
Z_0	Acoustic impedance
Z_{all}	Total impedance of a transfer matrix
Z_{cav}	Acoustic impedance of HR cavity
Z_{flow}	Acoustic impedance of the HR model in the presence of flow
Z_n	Acoustic impedance of the *n*-th HR model
Z_R	Radiation impedance of neck impedance
Z_v	Viscous and mass effect on neck impedance
α_i	Curve-fitting coefficient of characteristic frequency
α	Sound absorption coefficient
β	Empirical coefficient
Δx	Distance between positions 1 and 2
δ_v	Viscosity effect parameter
ν	Kinematic viscosity
ϕ_R	Effect of flow on neck length correction
ρ	Density of air

ρ_0	Mean background flow density
σ	Open area ratio
ω_0	Resonance frequency
μ	Dynamic viscosity coefficient
μ_T	Turbulent viscosity of the mean background flow

Chapter1

Introduction

1.1 Duct noise control

The term “noise” is defined as unwanted sound that causes people to feel unpleasant or disturbance. Noise can affect the mental health of humans. Thus, it is important to tackle the noise problems. Indoor noise has always been a significant source of noise pollution. Nowadays, people spend the majority of their time in indoor environments for work and entertainment. Therefore, attenuating indoor noise at all audible frequencies is a major task for engineers. The Heating, Ventilation, and Air-Conditioning (HVAC) ductwork system has become a crucial component of the modern building ensuring optimal indoor air. However, the ventilation fan, as a common component of the HVAC duct, can produce noise. The generated noise can be transmitted through the duct, subsequently propagating throughout the indoor environment. Traditional duct noise silencers can effectively reduce medium to high-frequency noise. Nevertheless, low-frequency HVAC duct noise control still remains a challenge to modern engineers.

Meanwhile, airflow is present in the HAVC duct. In most practical engineering applications, flow conditions are always neglected in the designing stage of the duct noise muffler. Therefore, the development of a good HVAC ductwork system is set back by the noise generated by grazing flow.

In modern buildings, the HVAC duct system brings in fresh air and gives out exhaust to create a comfortable indoor environment for residents. However, noise can propagate via the ductwork system. Besides, flow in the duct can also generate noise. To improve the working and rest conditions, many approaches are adopted to attenuate the noise propagating in the HVAC duct. Generally, these approaches could be categorized into two main types: Active Noise Control (ANC) and passive noise control.

1.1.1 Active noise control

ANC reduces unwanted sound through utilizing wave interference techniques. By detecting noise, generating a corresponding anti-noise wave, and leveraging destructive interference, ANC systems can significantly reduce noise in the ductwork system. In 1936, Lueg first proposed the idea of active noise cancellation, and provided several specific application environments including ductwork systems (Lueg, 1936). For a long time, ANC has been investigated from the conceptual perspective until Digital Signal Processors (DSP) were developed to achieve fast real-time noise cancellation(Carmona and Alvarado, 2000). Olson and May designed an electronic sound absorber consisting of microphones, power amplifiers, and secondary speakers to achieve active noise cancellation (Olson and May, 1953). Results showed that the designed ANC system can decrease noise by 11-24 dB between 40-120 Hz. Burgess investigated the sound cancellation in a one-dimensional ductwork system (Burgess, 1981). Besides, he summarized the existing ANC control algorithm and proposed the Filtered-X Least Mean Square (FXLMS) algorithm. Since then, the FXLMS algorithm has become an effective method to reduce duct noise. This algorithm is both simple and efficient, making it widely used in modern ANC systems. Since then, researchers have dedicated their efforts to enhancing the FXLMS algorithm for improved active noise control performance. Felix *et al.* proposed MC-FXLMS/F to attenuate the fan noise propagation in a duct (Félix, Magalhães and Papini, 2021). Compared to the classical FXLMS algorithm, their algorithm performs better when considering a substantial number of filters.

In practical application, Au Yeung *et al.* examined the validity of the noise cancellation of a commercial ANC device installed on a ductwork system (Au Yeung, Yiu and Chow, 1996). Results indicated that the ANC technique effectively complements conventional mufflers in reducing sound generated by the air-conditioning system. Larsson *et al.* incorporated an outer microphone cavity into an ANC system to mitigate the impact of the background flow inside the ventilation duct (Larsson *et al.*, 2009). Their results indicated that noise reduction of ANC can improve by more than 15 dB under a flow speed higher than 20 m/s. Rohlfing and Gardonio designed an ANC system to reduce the air-borne noise inside the air tube (Rohlfing and Gardonio, 2014). Besides, they integrated an active vibration control module on the ANC system to minimize vibrations and subsequently decrease the structure-borne noise radiated inside the air tube. Experimental results demonstrated that reducing vibration can significantly enhance the efficiency of ANC. Li *et al.* proposed the adaptive parameterized feedforward ANC algorithm applied to the U-shaped duct to minimize signal delay and the sound signal coupling of the different noise sources of the traditional ANC system (Li *et al.*, 2022). Their results revealed that the delay of the signal path of the adaptive parameterized feedforward ANC is reduced, indicating effective noise control of the time-varying noise signal.

1.1.2 Passive noise control

Compared to ANC, passive noise control is easy to manufacture and maintain, and therefore has been widely used in ductwork systems. Passive noise control can further be classified into reactive noise control and dissipative noise control based on whether the sound wave is reflected because of the surface properties of the structure or attenuated into heat. In practical situations, engineers always combine dissipative and reactive noise control to design high-performance mufflers.

A. Dissipative noise control

Dissipative noise control uses fibrous or porous material to attenuate sound energy into heat. The noise-absorbing performance highly depends on the acoustic property of the acoustic material (Morse and Ingard, 1986). The low-frequency noise can easily pass through fibrous or porous materials because of the long-wavelength characteristics. Therefore, dissipative noise control is always used to attenuate mid-to-high frequency noise.

Duct lining has been extensively used as an effective dissipative noise control method. Morse investigated the acoustic wave propagation in a rectangular pipe with lining on duct walls theoretically (Morse, 1939). Utley and Mulholland proved that using double and triple panels of lining can improve the sound insulation properties (Utley and

Mulholland, 1968). Cummings and Chang demonstrated that the fluid inside the duct can influence the sound wave propagation within the porous material. Besides, they discussed the impact of sound absorption in terms of transmission loss in the muffler (Cummings and Chang, 1988). Olny and Boutin investigated acoustic wave propagation in porous materials and discussed how to improve noise attenuation within the specific frequency band. (Olny and Boutin, 2003).

Perforated panels have been extensively used in industries and buildings to reduce noise. Bolt analyzed the acoustic behavior of the perforated panel (Bolt, 1947). He also proposed a design chart to provide absorption coefficients of the unfaced material. Maa designed the Micro Perforated Panel (MPP) and provided an empirical formula to calculate its acoustic impedance. (Maa, 1998). Experimental results showed that MPP demonstrates significant potential for broadband absorption across 3 to 4 octaves. In practical applications, an MPP absorber consists of a front panel made of MPP and a back cavity. Numerous researchers have been devoted to enhancing the noise attenuation performance of the MPP absorbers. Yu *et al.* applied the sub-structuring method to examine the influence of the internal partitions on MPP (Yu, Cheng and You, 2015). Results showed that the noise attenuation bandwidth can be enlarged by adding internal partitions with varying parameters. Wang *et al.* used parallel-arranged MPP arrays to design an absorber to achieve the most efficient sound absorption at around 500 Hz (Wang, Huang and Zhang, 2014). Researchers also combined MPP with porous material to design more effective absorbers. However, dissipative mufflers are typically inefficient at low frequencies and can only be effective to use under strict hygienic conditions. If the surrounding environment is humid and is accumulated with ashes, the noise attenuation performance of the dissipative mufflers would decrease.

B. Reactive noise control

Reactive noise control is also named reflective noise control. The reactive muffler consists of elements with different acoustic impedances. At the joint position of the elements, sound waves would be reflected back to sound source due to impedance mismatch. After years of research, researchers have proposed various kinds of reactive mufflers.

The Herschel-Quincke tube comprises two parallel pipes connected at varying lengths and cross-sectional areas. Stewart was the first to examine the noise absorption characteristics of HQ tube mufflers (Stewart, 1945). Over the years, the HQ tube mufflers have demonstrated their effectiveness in absorbing low-frequency noise. An investigation into HQ tube transmission loss was carried out through experimental, theoretical, and computational methods (Selamet *et al.*, 1994). Subsequently, Selamet removed the geometric constraints of the HQ design and modified it into an n-duct configuration (Selamet, 1997). However, the HQ tube has significant drawbacks, as it requires multiple length parameters to determine its placement on the ductwork system and establish its resonant frequency (Lato, 2018). This complexity makes the HQ system less convenient compared to other reactive silencers. Additionally, some studies indicated that the installation of an HQ tube muffler could disrupt flow distribution inside the ductwork system and the side-branch mounted HQ tube (Torregrosa, Broatch, & Payri, 2000).

Researchers designed new mufflers based on HQ to overcome these disadvantages. Lato *et al.* enhanced the traditional HQ muffler by transforming it into the infinity tube, which combines the two connection points of the HQ into a single cross-section on the side of the main duct (Lato *et al.*, 2019).

Miles investigated the sound wave transmission within the pipes with varying cross-sectional areas (Miles, 1944). Following his study, the expansion chamber was proposed as a solution for reducing low-frequency noise in the ductwork system. El-Sharkawy and Nayfeh presented experimental and analytical results of sound propagation in the expansion chamber with different expansion ratios and chamber lengths (El-Sharkawy and Nayfeh, 1978). Afterward, the influence of the mode of the acoustic wave on the sound attenuation ability of the expansion chamber was investigated (Ih and Lee, 1985). Selamet and Radavich determined the sound wave propagation inside the expansion chamber based on numerical simulation and analytical investigation (Selamet and Radavich, 1997). Shi examined the acoustic wave dispersion characteristics inside periodically arranged expansion chambers (Shi, 2016). The results indicated that different configurations could shift the stopbands or improve transmission loss results.

The Quarter-Wavelength Tube (QWT), also named side-branch resonator, is another commonly used reactive noise control muffler. The noise attenuation performance of the QWT is decided by its total length, which means only wavelengths equal to one-quarter of the QWT's length can be completely absorbed. Consequently, the QWT operates efficiently within a relatively narrow frequency range. Neise and Koopman installed a

QWT on a centrifugal fan to reduce the aerodynamic noise. Experiment results showed that noise pressure level is reduced by 29 dB (Neise and Koopmann, 1980). Howard and Craig tested QWT with different orifice geometries. Results showed that bell-mouth geometry can achieve the best noise reduction. Cervenka and Bednarik analyzed noise attenuation of a flush-mounted QWTs array by transfer matrix method (Červenka and Bednařík, 2018, 2020). An optimization algorithm was exploited to refine the geometric parameters of the QWT array to achieve effective broadband noise control. Yu studied the sound wave propagation inside a QWTs array featuring 11 side branches under grazing flow conditions (Ho Man Yu, 2020). Results showed that stronger sound pressures inside QWT can maintain better acoustic performance. Besides, the reversed arrangement of the QWT can minimize the impact of the background flow. Cambonie *et al.* proposed the bending QWT to reduce the space occupancy of the traditional QWT (Cambonie, Mbailassem and Gourdon, 2018). They discussed the noise attenuation performance of a bending QWT with different curvature ratios. Catapane *et al.* designed a coiled QWT to further reduce the space requirement (Catapane *et al.*, 2023). They also manufactured the coiled QET model to develop an experimental study. Experiment results showed that coiled QWT can provide sound absorption even if the dimension is only 1/18th of the targeted wavelength.

1.1.3 Hybrid noise control

In practical applications, engineers always combine reactive noise control with dissipative noise control to design duct mufflers to improve the Transmission Loss (TL) results and to achieve broadband noise control. Additionally, researchers tried to implement the ANC system on the mufflers of the ductwork system to further enhance noise absorption efficiency. Wu *et al.* combined an ANC system and a dissipative noise control muffler to reduce noise propagation in a ventilation duct (Wu *et al.*, 2022). The dissipative noise control muffler consists of a shell constructed by a perforation panel with foam filler. Two sets of microphone systems of the ANC system are mounted in the melamine foam. Experimental results showed that dissipative noise control mufflers can achieve 20 dB of noise attenuation, while the active noise control (ANC) system can provide an additional 10 dB of attenuation. Wang *et al.* proposed a broadband noise control muffler composed of an MPP plate and coiled QWT. They emphasized the noise attenuation mechanism through coupling effects and impedance matching (Wang *et al.*, 2023). Ryoo *et al.* combined MPP with Helmholtz resonators to control low-frequency noise with a low-level Q-factor (Ryoo, Yong Lee and Jeon, 2024). The parameters of the designed muffler were optimized through a machine learning algorithm based on an artificial neural network. Experimental results demonstrated that the muffler could achieve 90% noise absorption across a two-third octave band.

1.2 Helmholtz resonator

The Helmholtz Resonator (HR) is a widely used reactive noise muffler that is effective in reducing low-frequency noise owing to its ease of manufacture and maintenance. It consists of a thin neck and a large cavity. The HR is side-branch mounted on the ductwork system to reduce duct-borne noise. The air inside the neck and cavity forms a spring-mass system to attenuate the noise through the resonance effect. As a duct noise control muffler, HR has been employed in all kinds of ductwork systems, such as HVAC ducts in urban buildings, exhaust ducts in automobiles, and aircraft duct systems (Nayfeh, Kaiser and Telionis, 1975; Dastourani and Bahman-Jahromi, 2021; Yang and Sheng, 2023). Besides, HR has various application scenarios. Sugimoto proposed using HR connected to a tunnel to suppress the sound wave generated by a traveling train (Sugimoto, 1992). Liu *et al.* presented an electromechanical Helmholtz resonator (EMHR) to achieve noise control and acoustic energy harvesting simultaneously (Liu *et al.*, 2008). Their results indicated around 30 mW of output power under 160 dB sound pressure level. Wang *et al.* designed a noise barrier consisting of HR to absorb noise in the residential areas near the high-speed railway (Wang *et al.*, 2018). They also integrated an electricity-generating module on the HR to convert noise into electric energy. Experiment results showed that an output voltage of 74 mW can be generated by converting the absorbed noise from the surrounding environment.

Rayleigh provided a generalized description of energy variation in the HR with a spherical cavity (Rayleigh, 1916). Since then, researchers have focused on improving theoretical models to predict the noise attenuation of HR. Ingard examined the resonance frequency of HRs featuring various combinations of neck and cavity shapes (Ingard, 1953). He also proposed the end-correction formula to describe the actual influence of air motion near regions of the HR model. The influence of various shapes and positional combinations of the neck and cavity was also incorporated into a semi-empirical formula for calculating the resonance frequency of the HR. Alster proposed a theoretical expression to determine the sound transmission loss of HR (Alster, 1972). His expression has involved the cavity shape of common geometries. Selamet and Lee used an extended neck to extend the total neck length of HR to change the resonance frequency (Selamet and Lee, 2003). Wang and Mak used the Bloch wave theory to predict the noise attenuation in a ductwork system with the side-branch mounted HRs array (Wang and Mak, 2012). The theoretical predictions were validated by experiment results and numerical simulations. Cai and Mak proposed an equation to calculate the noise attenuation capacity (C_{TL}) of mufflers (Cai and Mak, 2018c). They calculated the C_{TL} of HRs with different geometrical parameters and discussed the relationship between C_{TL} and sound transmission loss.

In practical applications, researchers have focused on utilizing Helmholtz resonators to achieve broadband low-frequency noise control while enhancing noise attenuation efficiency by minimizing space occupancy. Xu *et al.* proposed the dual Helmholtz resonator and developed the expression to calculate its transmission loss (Xu, Selamet and Kim, 2010). The peak frequency and the noise attenuation band can be changed by adjusting the neck length and the volume of the dual HR. Shi and Mak modified the Helmholtz resonator by incorporating a spiral neck, allowing it to be installed in constrained places. (Shi and Mak, 2015). Cai and Mak compared the sound attenuation of different HR configurations theoretically (Cai and Mak, 2018a). Huang *et al.* proposed an acoustic metamaterial consisted of HR with an embedded neck (Huang *et al.*, 2019). Their designed structure has a tunable resonance frequency range between 137-300 Hz and can achieve perfect absorption. Besides, their structure has been proven to achieve the same noise absorption performance as the HR with a normal aperture. Seo *et al.* achieved broadband low-frequency noise control of HRs array under high sound pressure (Seo, Kim and Kim, 2016). Guo *et al.* designed and manufactured a structure with HRs array for low-frequency noise absorption (Guo, Zhang, *et al.*, 2021). They used an optimization algorithm to combine HRs with different parameters to design an array. Their structure can absorb 90% of the noise in a broadband frequency of more than 400 Hz.

1.3 Helmholtz resonator with grazing flow

The side branch-mounted HR in a ductwork system can be regarded as a rectangular T-junction structure (Du *et al.*, 2016). The aero-acoustical activities of the rectangular T-junction structures under various Mach numbers have been extensively investigated. Gikadi *et al.*(Gikadi, Föller and Sattelmayer, 2014) predicted the shear layer instabilities of a T-joint structure under different flow speeds by numerical simulation. Tonon *et al.*(Tonon *et al.*, 2011) analyzed the aeroacoustics behavior of pipe networks with side branch tubes with different geometric parameters. Dai *et al.*(Dai, Jing and Sun, 2012) investigated the flow field near the orifice of an HR influenced by vortex convection. These studies have shown that the sound attenuation and the acoustic impedance of Helmholtz resonators are consistently affected by the combination of the orifice and neck geometry, vortex convection, flow rate, and sound pressure level. These effects bring difficulties in predicting the sound transmission loss under flow conditions.

Researchers have built empirical formulas to calculate the acoustic response of the small orifice under grazing flow conditions. Mak *et al.* proposed an empirical formula to predict the flow noise of a ventilation duct. Lee and Ih (Lee and Ih, 2003) derived an empirical formula to determine the impedance of circular orifices with varying diameters, thicknesses, and perforation ratios. Seo *et al*.(Seo, Kim and Kim, 2018) employed curve-fitting analysis to establish an empirical flow term for calculating the acoustic impedance of small orifices under low flow Mach numbers. They incorporated this flow term into an empirical impedance model for circular orifices to predict transmission loss performance. Li and Choy (Li and Choy, 2024) indicated that the depth of the backing cavity can change the value of the acoustic resistance and the velocity field near the small orifices. They proposed a semi-empirical formula for incorporating the cavity shape factor of the perforated panel. This empirical formula can also be utilized to calculate the resistance of the orifice with backing cavities in the frequency range under different flow Mach numbers. Based on these empirical formulas of orifice, the relations between transmission loss of HR and the background grazing flow could also be established.

1.4 Objectives and Scope of Research

The main challenge of the HVAC ductwork systems is to achieve broadband low-frequency noise control under grazing flow conditions. Among all the duct noise control methods, the Helmholtz resonator offers a simple and cost-effective solution. The noise attenuation frequency band can be extended by using a periodically arranged HRs array. By modifying the geometry parameters of every HR in the array, the resonance frequency could be adjusted to achieve effective low-frequency noise control. Without grazing flow, HR can effectively control low-frequency noise. However, grazing flow cannot be neglected in the HVAC ductwork systems. In practical applications, the impact of grazing flow on the low-frequency noise absorption of the Helmholtz resonator muffler is often overlooked during the design stage.

Consequently, the objective of this study is to design an HRs array muffler for effective broadband low-frequency noise control under grazing flow conditions. To achieve this main objective, this study has been organized into four parts. In the first part of this study, a flow duct system is designed and manufactured to experimentally measure the sound wave propagation of the side-branch mounted HR model. The second part focuses on understanding the relationship between sound attenuation performance, the geometrical parameters of the HR model, and the grazing flow speeds. A CFD-acoustic coupled numerical simulation has been applied to finish this study. The third part examines the noise attenuation of HR under different flow conditions experimentally. A Helmholtz resonator model has been manufactured and installed on the flow duct system to record the sound signals under different grazing flow speeds. An empirical formula is established to estimate the transmission loss results of the single HR and the periodic HRs array under different grazing flow speeds. Finally, the fourth part proposed a lightweight and compact duct noise control muffler composed of the HRs array. Each single HR of this array is optimized to improve the noise absorption bandwidth. A semi-empirical formula is developed to predict the transmission loss results of the designed muffler under various grazing flow velocities.

1.5 Outline

The thesis is organized into six chapters. This chapter provides the background information for this study, encompassing the research background, a review of the relevant study, and the objectives of this research.

Chapter 2 introduces the research methodology of this study. It includes a numerical simulation method, experimental setup, and theoretical investigation. To measure the sound attenuation performance of the side-branch mounted HR muffler, a flow duct system has been developed and constructed. This section outlines the design process and the function of each component within the flow duct system. The Transfer Matrix Method (TMM) is utilized as a theoretical method for computing the acoustic wave propagation inside the duct and the mufflers. Besides, a Curved HR is proposed to replace traditional HR. The transmission loss performance of the Curved HR will be analyzed by TMM.

Chapter 3 analyzes the noise reduction performance of a side-branch mounted dual HRs model numerically. Two HRs are arranged in serial on the same side of a main duct to form a side-branch mounted dual HRs muffler to increase the sound transmission loss results. A three-dimensional numerical simulation is implemented through a CFD-acoustic coupled approach. The sound pressure field and flow field results are presented to illustrate the fluid dynamic and acoustic behavior of the side-branch mounted dual HRs system under grazing flow. The impact of grazing flow speed, neck length, and cavity volume on the sound transmission loss results are discussed in this chapter.

Chapter 4 presents experimental investigations into the noise attenuation characteristics of the side-branch mounted Helmholtz resonator under different grazing flow speeds. A three-dimensional model of HR has been manufactured and side-branch mounted on the test section of the flow duct system to test the sound transmission results under different grazing flow speeds. The relation between the flow speed and transmission loss result of the HR model would be achieved through curve fitting techniques. A semi-empirical formula is proposed to forecast the noise attenuation ability of the HR under different grazing flow speeds. This empirical model is integrated into the TMM to predict sound transmission loss results of the period Helmholtz resonator model under different grazing flow speeds.

Chapter 5 proposes a lightweight and compact duct noise control muffler composed of the Helmholtz Resonator with Embedded Neck (HREN) array. The constructed muffler consists of eight individual HREN models and is optimized to provide effective noise reduction of the low-frequency band. The normal absorption results of the single HREN models are experimentally obtained using an impedance tube. A semi-empirical formula has been proposed to calculate the noise absorption results of the designed muffler under various grazing flow velocities. The designed muffler is installed on the flow duct system to test its sound transmission loss results under grazing flow conditions.

Finally, Chapter 6 provides a summary of the whole studies and findings discussed in this thesis and suggests potential directions for the next research based on current work.

Chapter 2

Methodology

2.1 Introduction

The methodologies used to assess the noise attenuation ability of the Helmholtz Resonator (HR) models are presented in this chapter. The whole research is carried out via theoretical analysis, numerical simulations, and experimental studies. By specifying the geometric parameters and physical field of the Helmholtz resonator model, the acoustic and fluid dynamic responses could be determined by numerical simulation. Additionally, the numerical results can elucidate the relationship between geometry parameters, flow speed, and sound wave propagation. The numerical simulation strategy will be introduced in this chapter.

In this study, the experiment procedure involves two phases. In the first phase, an HR prototype model has been manufactured to measure the noise absorption results. The experiment results will be compared with numerical simulation and analytical prediction. The second phase of the experiment will investigate the noise attenuation performance of a side-branch mounted muffler consisting of a periodic HRs array. To finish the acoustic experiment, a flow duct system has been designed and manufactured. The design details and performance of the experiment setup have been reported in this section.

The sound propagation inside the ductwork system would be solved by the Transfer Matrix Method (TMM). If the muffler is treated as a lumped-parameter model, its acoustic impedance could be determined. Consequently, the sound propagation within the duct and the noise attenuation ability could be calculated using TMM. This section will introduce the TMM by calculating the wave propagation of a Curved HR side-branch mounted on a ductwork system. Compared to straight HR, Curved HR can save space, making them suitable for installation in restricted areas. This feature is particularly important in practical applications.

2.2 Numerical simulations

This study employs COMSOL Multiphysics to conduct a numerical investigation of the noise attenuation ability and fluid dynamics of HR. The numerical method consists of three steps: first, a Computational Fluid Dynamics (CFD) simulation is applied to solve the background flow under a very fine mesh; then, the flow field results are mapped to a course mesh. Finally, the acoustic results would be solved using a coarse mesh. A detailed numerical strategy is presented in this section.

2.2.1 CFD module

The Reynolds Averaged Navier–Stokes (RANS) model has been widely applied to simulate the background flow of the HR. Researchers have used the RANS model to simulate the flow inside ductwork systems and HRs. The numerical results indicate that the RANS model can effectively capture the time-averaged flow and vortex in the ductwork system (Ghanadi *et al.*, 2015). Researchers have also used the Large Eddy Simulation (LES) turbulence model to capture the vortex-acoustic coupling behavior of HR (Shahzad, Hickel and Modesti, 2023). In this research, the RANS model is sufficient for simulating the background flow, and it could save computing resources. For a compressible, steady-state airflow, the governing equations are as follows:

$$\nabla \cdot (\rho \mathbf{u}) = 0 \tag{2.1}$$

$$\rho(\mathbf{u} \cdot \nabla)\mathbf{u} = \nabla \cdot [\mu(\nabla \mathbf{u} + (\nabla \mathbf{u})^T) - p\mathbf{I} - \tfrac{2}{3}\mu(\nabla \cdot \mathbf{u})\mathbf{I}] + \mathbf{F} \tag{2.2}$$

where ρ denotes the density of air, $\mathbf{u}$ is the velocity of flow, **I** represents the identity matrix, μ denotes the dynamic viscosity coefficient, and **F** represents the source term.

The *k*-*ε* turbulence model has been widely used to simulate the turbulence inside a ductwork system. Therefore, this model has been selected to module the turbulent flow. This model utilizes the following equations to solve the dissipation rate of the turbulence kinetic energy (*ε*) and the value of the turbulence kinetic energy (*k*):

$$\rho(\mathbf{u} \cdot \nabla)k = \nabla \cdot ((\mu + \tfrac{\mu_\tau}{\sigma_k})\nabla k) + P_k - \rho\varepsilon \tag{2.3}$$

$$\rho(\mathbf{u} \cdot \nabla)\varepsilon = \nabla \cdot ((\mu + \tfrac{\mu_\tau}{\sigma_\varepsilon})\nabla \varepsilon) + C_{\varepsilon 1}\tfrac{\varepsilon}{k}P_\lambda - C_{\varepsilon 2}\tfrac{\varepsilon^2}{k}\rho \tag{2.4}$$

where $\sigma_k = 1.0$, $\sigma_\varepsilon = 1.3$, $C_{\varepsilon 1} = 1.44$ and $C_{\varepsilon 2} = 1.92$ are constants, $\mu_\tau$is the turbulent viscosity, P_k is the production term.

2.2.2 Mapping Between CFD and Acoustics Mesh

In this study, two different meshes have been built to separately calculate the CFD results and acoustic responses. Therefore, a mapping study must be used to map and smooth the grazing flow of CFD results into the acoustic mesh by solving an additional set of equations. The mapping strategy is achieved by solving:

$$P_{0,aco} - P_0 = \delta h^2 \nabla \cdot (\nabla P_{0,aco}) \tag{2.5}$$

$$\boldsymbol{u}_{0,aco} - \boldsymbol{u}_0 = \delta h^2 \nabla \cdot (\nabla \boldsymbol{u}_{0,aco}) \tag{2.6}$$

$$\rho_{0,aco} - \rho_0 = \delta h^2 \nabla \cdot (\nabla \rho_{0,aco}) \tag{2.7}$$

$$T_{0,aco} - T_0 = \delta h^2 \nabla \cdot (T_{0,aco}) \tag{2.8}$$

$$\mu_{T,aco} - \mu_T = \delta h^2 \nabla \cdot (\mu_{T,aco}) \tag{2.9}$$

where P_0, $\boldsymbol{u}_0$, ρ_0, T_0 and μ_T are the pressure, velocity, density, temperature and turbulent viscosity of the mean background flow, respectively; $P_{0,aco}$, $\boldsymbol{u}_{0,aco}$, $\rho_{0,aco}$, $T_{0,aco}$ and $\mu_{T,aco}$ are these parameters mapped onto the acoustic mesh. δ =0.01 is constant and h is the mesh size.

2.2.3 Acoustic Module

The Linearized Navier-Stokes solver of Frequency (LNSF) interface of the COMSOL Multiphysics has been utilized to simulate the acoustic field of HR model. The governing equations are given as follows:

$$\rho_0(i\omega\mathbf{u}_t + (\mathbf{u}_t \cdot \nabla)\mathbf{u}_0 + (\mathbf{u}_0 \cdot \nabla)\mathbf{u}_t) + \rho_t(\mathbf{u}_0 \cdot \nabla)\mathbf{u}_0 = \nabla \cdot \sigma + F - \mathbf{u}_0 M \quad (2.10)$$

$$i\omega\rho_t + \nabla \cdot (\rho_0\mathbf{u}_t + \rho_t\mathbf{u}_0) = M \quad (2.11)$$

$$\rho_0 C_p(i\omega T_t + \mathbf{u}_t \cdot \nabla T_0 + \mathbf{u}_0 \cdot \nabla T_t) + \rho_t C_p(\mathbf{u}_0 \cdot \nabla T_t) - \alpha_p T_0(i\omega p_t + \mathbf{u}_t \cdot \nabla p_0 + \mathbf{u}_0 \cdot \nabla p_t) - \alpha_p T_t(\mathbf{u}_0 \cdot \nabla p_t) = \nabla \cdot (k\nabla T_t) + \Phi + Q \quad (2.12)$$

where $\mathbf{u}_t$, p_t, T_t and $\rho_t$are the acoustic perturbations of velocity, pressure, temperature and density, respectively. The right-hand terms, M, $\boldsymbol{F}$ and Q are the source terms. C_p is the heat capacity. σ is the stress tensor and Φ is the viscous dissipation function.

2.3 Experimental measurements

A flow duct system is designed and manufactured to investigate the sound transmission loss performance of the side-branch mounted HR model under grazing flow conditions. Figure 2.1 depicts the setup of the flow duct system. The flow duct system comprises a centrifugal fan, a diffusion section, an anechoic termination, a sound source, a flow development section, and a test section. The whole system is supported by an aluminum frame to lift about 50cm above the ground. The anti-vibration mats are stuck at the connections between the bracket and the instrumentation system to isolate the low-frequency vibrations from the surrounding environment. Additionally, a flexible duct is used to connect the fan and diffusion section to minimize the effects of fan vibration. All these section connections are fixed with silicone sealant to prevent air leakage and sound leakage.

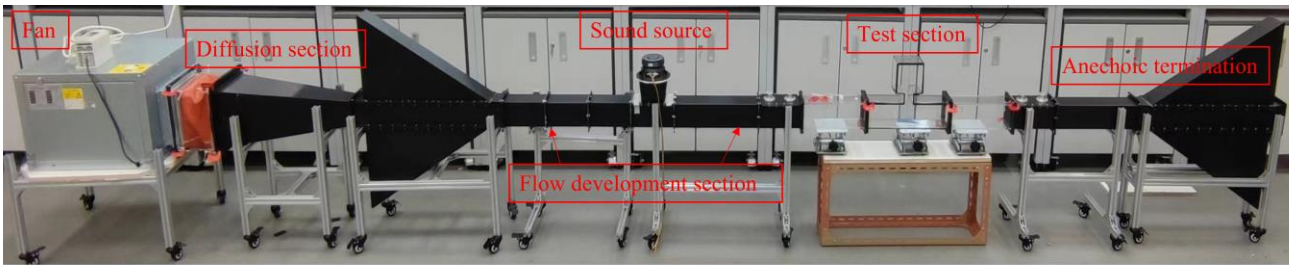

Figure 2.1 Photograph of the flow duct system.

A variable-frequency drive regulates the rotational frequency of the centrifugal fan to adjust the flow rate inside the duct system. The maximum airflow velocity is around 20 m/s, which is typical in building ventilation systems. The airflow generated by the fan enters the flow duct through a diffusion section. The diffusion section gradually reduces the cross-sectional area to 10 cm × 10 cm, while maintaining a constant cross-sectional area in other sections of the flow duct. A loudspeaker is located at the downstream side of the diffusion section as the noise source to generate acoustic waves with a Sound Pressure Level (SPL) of about 120 dB. The reflected acoustic wave is absorbed by the anechoic termination. Four microphones are flush-mounted at both sides of the test section to capture the sound signal at both sides of the side-branch mounted HR model under different grazing flow conditions.

2.3.1 Anechoic termination

Two anechoic terminations are located at the downstream side of the test section and the upstream side of the diffusion section. As illustrated in Figure 2.2, the anechoic termination features a cross-section with continuous expansion, which resembles a catenoidal horn. The design and manufacture of the anechoic termination follow the guidelines of EN ISO 5136:2009 (‘EN ISO 5136:2009 - Acoustics - Determination of sound power radiated into a duct by fans and other air-moving devices’, 2009). The height of each anechoic termination is about 50 cm, and has a total length of 75cm. A perforated plate of an open-area ratio at around 55% is located between the duct and the expansion region. The expansion region of the horn is filled with fiberglass of a density of approximately 48 kg/m^3, which can attenuate the sound power from both the centrifugal fan and the loudspeaker. Therefore, the noise from the background flow can be attenuated, and the reflected acoustic wave can be suppressed, which could improve the accuracy of the acoustic measurements.

(a) (b)

Figure 2.2 Anechoic termination.

2.3.2 The sound source and the flow development section

The sound source and the flow development section are shown in Figure 2.3. A loudspeaker functions as a noise source to generate the acoustic wave at the upstream side of the flow duct system. To overcome background noise, the loudspeaker is amplified by the B&K power amplifier Type 2706 to produce white noise with SPL above 115 dB. The white noise is generated via the B&K signal generator Type 1405. The loudspeaker is mounted in the middle of the flow development section. A honeycomb flow straightener is placed within the flow development section to improve flow uniformity. The length of the flow development section is 2m, which is long enough to guarantee flow uniformity near the test section.

(a) (b)

Figure 2.3 The sound source and the flow development section.

2.3.3 Test section

As illustrated in Figure 2.4, the test section is manufactured by an acrylic plate for observing the flow field inside the test sample. An HR model is side-branch mounted on the test section as the test sample. The transmission loss performance of the test sample would be assessed by using the four-microphone method. Consequently, four mounting holes are positioned 50-60 cm from the test sample to install the acoustic microphone.

The acoustic pressure signals are captured by four B&K type 4189 ½ inch microphones that are installed on the side walls of the duct through these holes. The collected signals are recorded through a B&K Type 3506 PULSE system. The flow field results near the test section are also measured. A Pitot tube is positioned at the upstream side of the test sample to measure the velocity profile and the pressure fluctuation in a separate experiment.


(a) (b)

Figure 2.4 The Helmholtz resonator model and the microphone mounting holes.

2.3.4 Performance of the flow duct system

The velocity profile near the test sample is assessed by a Pitot static tube. The probe is moved vertically from bottom to top in 10 mm increments, allowing for the measurement of nine velocity points. As shown in Figure 2.5, symbols and lines are velocity profiles measured by Pitot tube and calculated by an analytical equation from Spillere *et al* (Spillere, Cordioli and Boden, 2017). When the average velocity V equals 10 m/s and 15 m/s, the velocity distribution demonstrates good flow uniformity. However, at the top side of the duct, velocity has a slight decrease. The installation gap between the duct sections may cause the non-uniform velocity distribution.

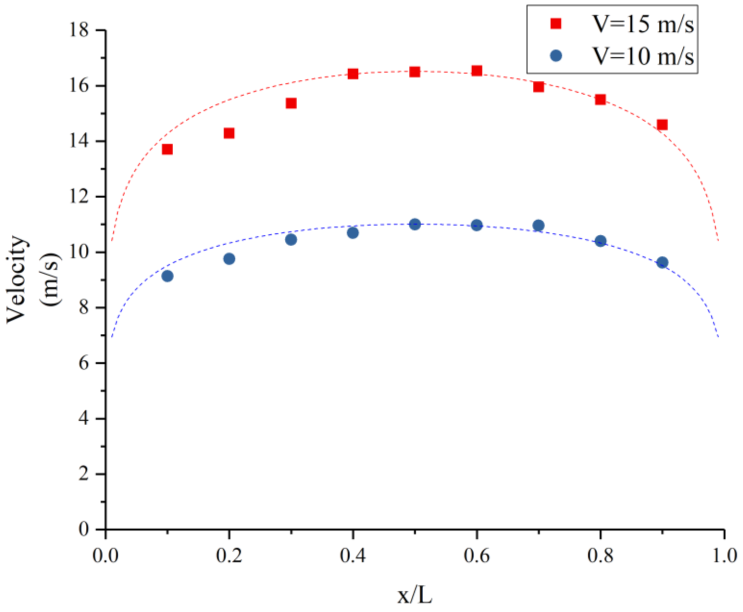

Figure 2.5 Velocity profile when average velocity equals 15 m/s and 10 m/s.

The Pitot static tube also measures the dynamic pressure at these nine locations. As shown in Table 2.1, the high consistency between the dynamic pressure results and the velocity distribution results indicates the uniformity of the velocity distribution. After the field flow measurement, the Pitot static tube is removed, and the hole used for installing the probes is sealed to avoid any interference with the acoustic measurement results.

Table 2.1 Dynamic pressure at nine measure points

Points	Dynamic Pressure (Pa)			
	V=10 m/s	Relative error	V=15 m/s	Relative error
1	51.20	[43.3~54.7]	115.00	[106.8~123.0]
2	58.30	[51.0~64.6]	124.90	[116.3~135.6]

3	66.90	[61.9~70.2]	144.50	[131.9~152.4]
4	70.00	[64.5~75.7]	165.10	[154.0~178.2]
5	74.10	[70.3~77.4]	166.70	[155.8~177.6]
6	73.70	[69.8~76.1]	167.60	[158.2~179.9]
7	73.60	[69.9~75.6]	156.00	[149.0~167.3]
8	66.20	[62.2~69.4]	147.10	[140.6~155.6]
9	56.70	[49.0~61.1]	130.40	[122.0~136.9]

Figure 2.6 (a) illustrates the absorption coefficient result of the anechoic termination. Measurement and data processing adhere to the guidelines outlined in ISO 10534-2 (‘ISO 10534-2:2023 - Acoustics — Determination of acoustic properties in impedance tubes — Part 2: Two-microphone technique for normal sound absorption coefficient and normal surface impedance’, 2023). It is evident that the anechoic termination can absorb over 80% of acoustic energy within the target frequency band (200 Hz - 1600 Hz), thereby ensuring excellent acoustic measurement performance. Figure 2.6 (b) shows the background noise near the test section when the flow speed generated by the centrifugal fan equals 20 m/s. The background noise is much lower than the acoustic signal generated by the loudspeaker, which indicates that the background noise from the centrifugal fan would influence the experiment results.

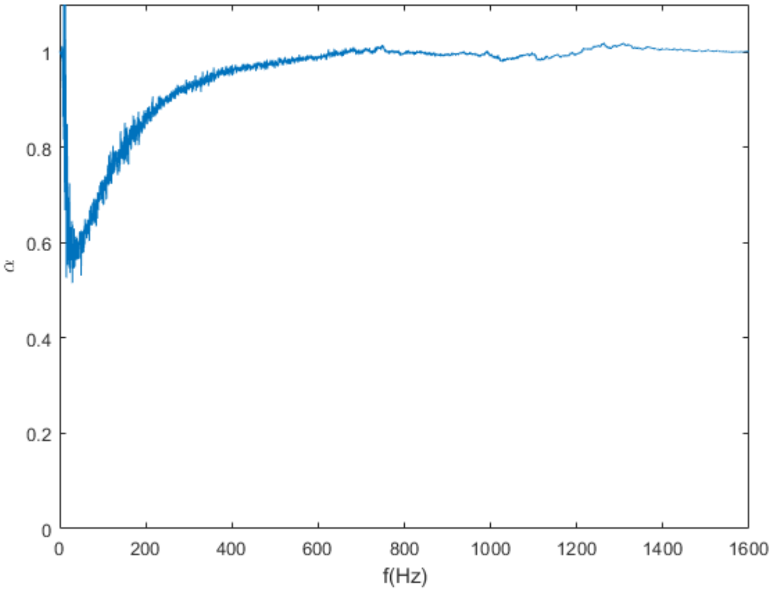

(a)

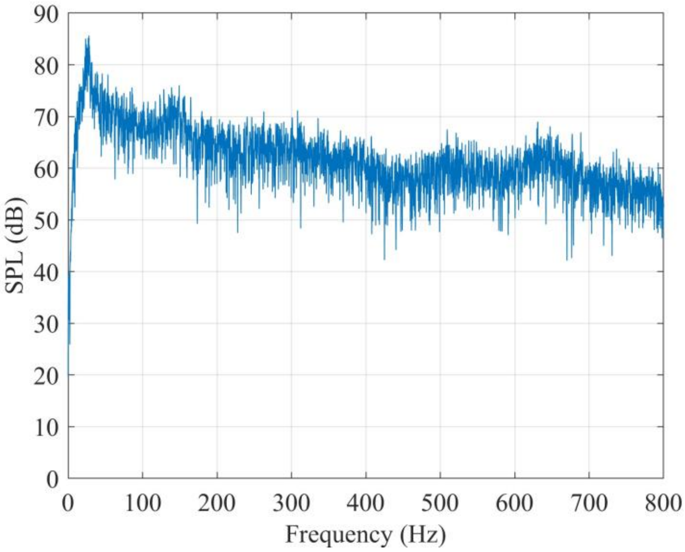

(b)

Figure 2.6 (a) Absorption coefficient of the anechoic termination (b) Background noise of the centrifugal fan.

2.4 Analytical model

In this research, TMM would be utilized to analytically calculate the acoustic wave propagation inside the ductwork system with side-branch mounted mufflers. TMM has been utilized for many years to determine the sound transmission loss performance of mufflers. This method is particularly suitable for one-dimensional muffler systems.

By introducing TMM, a Curved HR is proposed in this section. As shown in Figure 2.7, a curved HR is side-branch mounted on a main duct and features two curved necks with a curved cavity. Compared to traditional HR, Curved HR can reduce space occupation while maintaining the same neck and cavity volumes. This feature is crucial for the practical application of HR-based mufflers that are side-branch mounted on ductwork systems that are often installed in confined spaces. In this section, the sound propagation inside a side-branch mounted Curved HR is analyzed by TMM. The actual noise attenuation performance of the Curved HR will be discussed in detail.

2.4.1 Sound wave propagation and the transfer matrix method

Assuming that only planar sound waves are present within the ductwork system, the characteristics of sound waves along the longitudinal orientation of the duct is described as follows:

$$\frac{\partial^2 p}{\partial x^2} = \frac{1}{c^2}\frac{\partial^2 p}{\partial t^2} \tag{2.13}$$

where *c*=343 m/s denotes the sound speed of air, *p* represents the acoustic pressure, and *t* represents the time. Supposing wave is time-harmonic, the sound pressures and particle velocities along the longitudinal direction of the ductwork system can be solved by Equation (2.14) and (2.15):

$$p(x,t) = p_I e^{j(\omega t - kx)} + p_R e^{j(\omega t + kx)} \tag{2.14}$$

$$u(x,t) = \frac{p_I}{\rho_0 c} e^{j(\omega t - kx)} - \frac{p_R}{\rho_0 c} e^{j(\omega t + kx)} \tag{2.15}$$

where ρ_0=1.2 kg/m^3 is the air density, $j = \sqrt{-1}$ denotes the imaginary unit, and p_I and p_R are acoustic pressure magnitudes representing acoustic waves traveling in opposite directions. Additionally, ω refers to angular frequency, $k = \omega/c$ is the wave number.

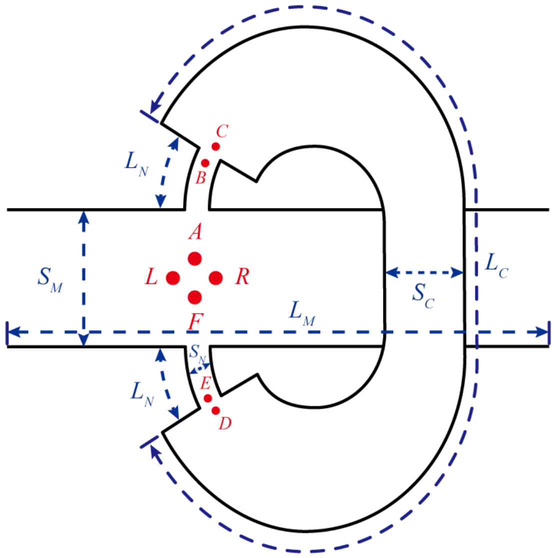

Figure 2.7 Schematic of a Curved HR

The Transfer Matrix Method (TMM) has been generally employed to assess the noise reduction performance of mufflers (Morse and Ingard, 1986). The acoustic transfer matrix for a ductwork system with a uniform cross-section and length, such as between the duct of points *C* and *D* in Figure 2.7, is represented as follows:

$$\begin{bmatrix} p(0,t) \\ \rho_0 cu(0,t) \end{bmatrix} = \begin{bmatrix} T_{11} & T_{12} \\ T_{21} & T_{22} \end{bmatrix} \begin{bmatrix} p(L_C,t) \\ \rho_0 cu(L_C,t) \end{bmatrix} = \mathbf{T_{CD}} \begin{bmatrix} p(L_C,t) \\ \rho_0 cu(L_C,t) \end{bmatrix} \tag{2.16}$$

where L_{EC} denotes the length between points *C* and *D*. The volume velocities $u(0,t)$, $u(L_C,t)$, and sound pressures $p(0,t)$, $p(L_C,t)$ can be solved from Equation (2.17) and

Equation (2.18):

$$p(0,t) = [p_I + p_R]e^{j\omega t} \tag{2.17a}$$

$$\begin{aligned} p(L_{EC},t) &= [p_I e^{-jkL_C} + p_R e^{jkL_C}]e^{j\omega t} \\ &= [(p_I + p_R)\cos\, kL_C - j(p_I - p_R)\sin\, kL_C]e^{j\omega t} \end{aligned} \tag{2.17b}$$

$$u(0,t) = \frac{1}{\rho_0 c}[p_I - p_R]e^{j\omega t} \tag{2.18a}$$

$$\begin{aligned} u(L_{EC},t) &= \frac{1}{\rho_0 c}[p_I e^{-jkL_C} - p_R e^{jkL_C}]e^{j\omega t} \\ &= \frac{1}{\rho_0 c}[(p_I - p_R)\cos\, kL_C - j(p_I + p_R)\sin\, kL_C]e^{j\omega t} \end{aligned} \tag{2.18b}$$

Assuming the time-harmonic terms are ignored, Equation (2.17) and Equation (2.18) could be rearranged into the matrix form:

$$\begin{bmatrix} p(L_C) \\ \rho_0 cu(L_C) \end{bmatrix} = \begin{bmatrix} \cos\, kL_C & -j\sin\, kL_C \\ -j\sin\, kL_C & \cos\, kL_C \end{bmatrix} \begin{bmatrix} p(0) \\ \rho_0 cu(0) \end{bmatrix} \tag{2.19}$$

TMM can also be applied to determine the transfer function at the junction points. Based on the principles of equality of pressure and continuity of air flow, the transfer function between points *B* and *C* in Figure 2.7 can be expressed as follows:

$$\begin{bmatrix} p(B) \\ \rho_0 cu(B) \end{bmatrix} = \begin{bmatrix} 1 & 0 \\ 0 & \frac{S_C}{S_N} \end{bmatrix} \begin{bmatrix} p(C) \\ \rho_0 cu(C) \end{bmatrix} = \mathbf{T_{BC}} \begin{bmatrix} p(C) \\ \rho_0 cu(C) \end{bmatrix} \tag{2.20}$$

By determining the product of the transfer functions of each part of the Curved HR, the particle velocity and sound pressure between point *A* to point *F* in Figure 2.7, are expressed as follows:

$$\begin{bmatrix} p(A) \\ \rho_0 cu(A) \end{bmatrix} = \mathbf{T_T} \begin{bmatrix} p(F) \\ \rho_0 cu(F) \end{bmatrix} = \begin{bmatrix} T_{T11} & T_{T12} \\ T_{T21} & T_{T22} \end{bmatrix} \begin{bmatrix} p(F) \\ \rho_0 cu(F) \end{bmatrix} = \mathbf{T}_{\mathrm{AB}} \mathbf{T}_{\mathrm{BC}} \mathbf{T}_{CD} \mathbf{T}_{\mathrm{DE}} \mathbf{T}_{\mathrm{EF}} \begin{bmatrix} p(F) \\ \rho_0 cu(F) \end{bmatrix} \tag{2.21}$$

where $\mathbf{T_T}$ denotes the total transfer matrix of the Curved HR, $\mathbf{T_{AB}}$ to $\mathbf{T_{EF}}$ denotes the transfer matrix of each section of the Curved HR. The transfer matrix from $\mathbf{T_{AB}}$ to $\mathbf{T_{EF}}$ can be readily calculated using Equation (2.20) and Equation (2.21).

2.4.2 Transmission loss of the Curved HR

Once the relationship of the acoustic property has been established using the TMM, the next step is to examine the sound attenuation ability of the side-branch mounted mufflers. In this study, once the transfer matrix between point *A* and point *F* is acquired through Equation (2.21), the subsequent step involves calculating the transfer matrix from point *L* to point *R*. The equality of pressure and the continuity of volumetric flow at the connection position can lead to the following equations:

$$\begin{cases} P(L) = P(R) = P(A) = P(F) \\ S_M U(L) + S_N U(F) = S_M U(R) + S_N U(A) \end{cases} \tag{2.22}$$

By rearranging Equation (2.22), we can obtain:

$$U(L) = \frac{S_N}{S_M}(U(A) - U(F)) + U(R) \tag{2.23}$$

By integrating Equation (2.23) with Equation (2.20) and Equation (2.21), we can determine the results of particle velocity u and sound pressure P from point *A* to point *F*:

$$\begin{cases} P(A) = T_{T11}P(F) + T_{T12}\rho_0 cu(F) \\ \rho_0 cu(A) = T_{T21}P(F) + T_{T22}\rho_0 cu(F) \end{cases} \tag{2.24}$$

Then, by rearranging these equations, the transfer function of the side-branch mounted Curved HR (from point L to point R) can be determined:

$$\begin{aligned} \begin{bmatrix} p(L) \\ \rho_0 cu(L) \end{bmatrix} = \mathbf{T_M} \begin{bmatrix} p(R) \\ \rho_0 cu(R) \end{bmatrix} = \begin{bmatrix} T_{M11} & T_{M12} \\ T_{M21} & T_{M22} \end{bmatrix} \begin{bmatrix} p(R) \\ \rho_0 cu(R) \end{bmatrix} \\ = \begin{bmatrix} 1 & 0 \\ \frac{S_N}{S_M} \frac{T_{T12}T_{T21} + (T_{T22}-1)(1-T_{T11})}{T_{T12}} & 1 \end{bmatrix} \begin{bmatrix} p(R) \\ \rho_0 cu(R) \end{bmatrix} \end{aligned} \tag{2.25}$$

Lastly, the sound Transmission Loss (TL) result of the Curved HR model could be solved by:

$$TL = 20\log_{10} \left|\frac{1}{2}(T_{M11} + T_{M12} + T_{M21} + T_{M22})\right| \tag{2.26}$$

2.4.3 Results and discussion

The FEM numerical simulations are conducted by using COMSOL Multiphysics to verify the correctness of the TL results obtained by TMM. The geometrical parameters for the Curved HR of this case are detailed in Table 2.2. In this study, the frequency range of interest is lower than 1000 Hz, which is the common frequency range of the reactive noise control muffler. As illustrated in Figure 2.8, the Curved HR model exhibits three resonance frequency peaks within the chosen frequency range. The results from the TMM calculation and from the FEM simulation are very close, especially near the first resonance peak. The frequencies associated with the resonance peaks are provided in Table 2.3. It can be observed that the resonance peak results show a minimum 4Hz error near the first peak and a maximum 10Hz error near the second peak. Overall, the TMM predictions exhibit a high level of accuracy about the resonance frequency. However, there are some errors when predicting the resonance peak.

Table 2.2 Geometrical parameters of the Curved HR in verification case.

	Length (mm)	Area (mm^2)
Main duct	L_M=1000	S_M=5674.5
Neck	L_N=95.91	S_N=1418.6
Cavity	L_C=958.19	S_C=5674.5

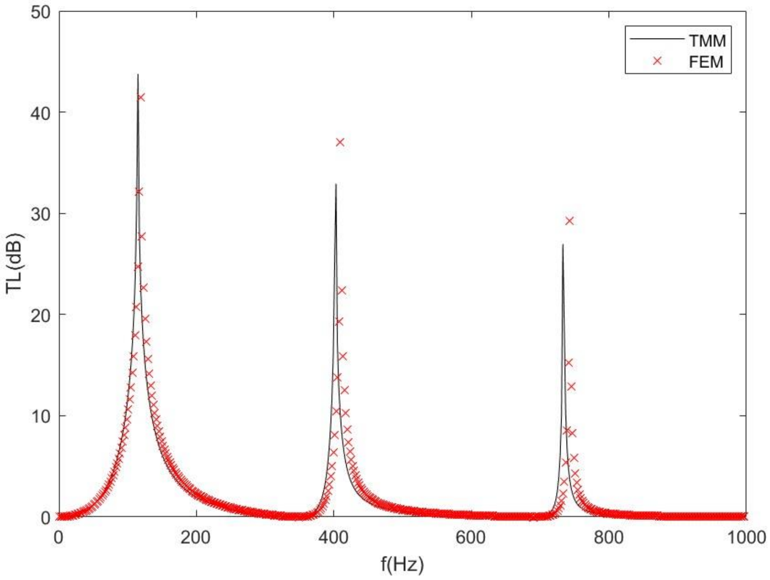

Figure 2.8 A comparison of the theoretical and numerical transmission loss results for the Curved HR (solid lines indicate TMM predictions, and crossed dots indicate FEM simulation).

Table 2.3 The resonance frequency results from TMM calculation and FEM simulation.

	TMM calculation	FEM simulation
Peak1	115Hz	119Hz
Peak2	403Hz	409Hz
Peak3	733Hz	743Hz

The transmission loss results for the Curved HR and the Parallel HR are compared to examine their effectiveness in noise attenuation. The sound transmission loss performance of the Parallel HR model has been examined by Cai and Mak (Cai and Mak, 2018a). As shown in Figure 2.9, the Parallel HR can be regarded as two single HRs mounted within the same section of a ductwork system. Equation (2.27) has been used to calculate the TL results of the traditional HR:

$$TL = 20\log_{10}\left(\frac{1}{2}\left|2 + \frac{\rho_0 c}{S_N}\frac{1}{2Z_r}\right|\right) \tag{2.27}$$

where Z_r represents the impedance of each HR. In this study, the geometrical parameters for the Parallel HR match those of the Curved HR outlined in Table 2.2. The dimensions of the neck for the Parallel HR are L_n=95.91mm and S_N=1418.6mm^2. The cavity parameters for the Parallel HR include L_C=958.19 mm and S_C=5674.5mm^2. The volume of the cavity of the Parallel HR model is equal to half that of the Curved HR.

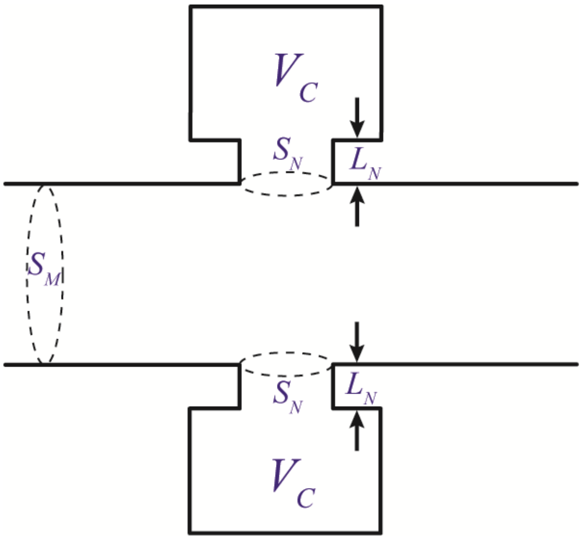

Figure 2.9 Configuration of a parallel HRs system.

As presented in Figure 2.10, the TL characteristics of the Curved HR differ from those of the Parallel HR model. The Curved HR only has three resonance peaks within the frequency range lower than 800 Hz, whereas the Parallel HR exhibits two. Besides, in the lower-frequency range (1-350Hz), the Parallel HR has a resonance frequency of 133 Hz, representing a 14 Hz increase compared to the Curved HR. In the medium frequency range (350-650Hz), the resonance frequency of the Parallel HR is 473Hz, indicating a 64 Hz increase compared with the Curved HR. These resonance frequency characteristics indicate a significant distinction between the Curved HR and Parallel HR systems, even though they share the same geometric parameters. The Curved HR has a lower resonance frequency, making it more effective for attenuating low-frequency noise. Besides, the Curved HR provides an additional resonance peak which is not found in the Parallel HR system. Consequently, the low-frequency noise attenuation performance of the Curved HR surpasses that of the Parallel HR.

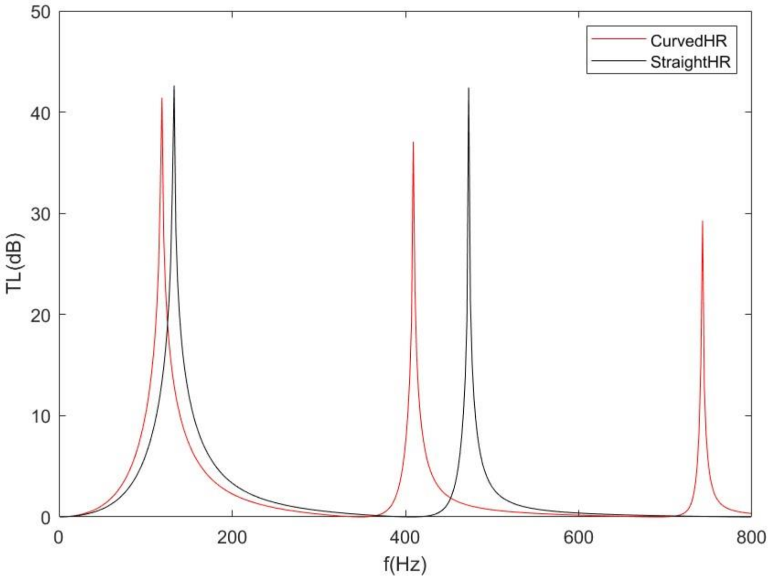

Figure 2.10 Comparison of the transmission loss results between a Curved HR model and a Parallel HR system (the red lines correspond to the results for the Curved HR, while the black lines correspond to the results for the Parallel HR system).

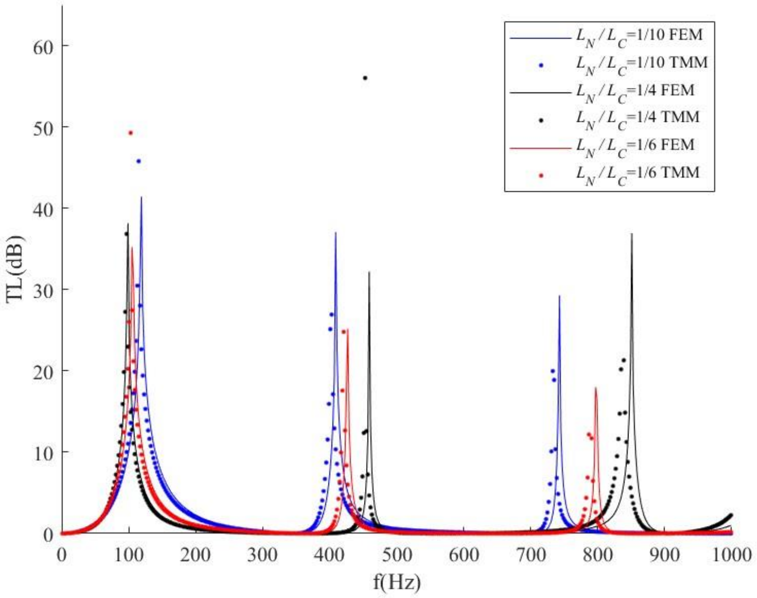

Figure 2.11 Comparison of the TL results for the Curved HR at various cavity length ratios.

The Curved HR with varying geometrical parameters is examined to evaluate the impact of geometry parameters on transmission loss performance. Figure 2.11 displays the transmission loss result of the Curved HR with various length ratios. The neck and cavity lengths vary with different ratios from 1/10 to 1/4, while the overall length of the Curved HR is fixed at 1150mm. These length values are detailed in Table 2.4. The FEM simulation and TMM calculations are performed to ensure the accuracy of the transmission loss. The Curved HR typically exhibits three resonance peaks, which emerge near the frequency ranges between 0-350 Hz, 350-650 Hz, and 650-1000 Hz. Consequently, these frequency ranges are separated into three sub-domains to differentiate between lower, medium, and higher-resonance peaks. In the lower-frequency range, the resonance frequencies of the Curved HR with different length ratios are close, whereas more differences emerge in the medium and higher-frequency ranges. The following principles can be summarized for the Curved HR with various length ratios:

In the lower-frequency range, the length ratio has a minimal impact on the bandwidth and resonance frequency of TL results. Curved HR with a higher length ratio exhibits minimally lower TL peaks and narrower TL bandwidth. However, in the medium frequency range, length ratios can significantly affect the transmission loss result. The Curved HR model with greater length ratios shows higher resonance frequencies with narrower TL bandwidths. Compared to the lower-frequency range, the Curved HR demonstrates a much narrower TL bandwidth in the medium-frequency range, suggesting that increasing the length ratio is less effective for noise absorption in the medium-frequency. In the higher-frequency range, length ratios greatly influence transmission loss results. As the length ratio increases from 1/10 to 1/4, the resonance frequency rises by nearly 100 Hz. Additionally, the Curved HR featuring a length ratio of 1/4 exhibits a much broader TL bandwidth than other Curved HR models, indicating that increasing the neck length enhances higher-frequency noise attenuation performance.

Table 2.4 Parameters of L_N and L_C of Curved HR in Figure 2.11

L_N/L_C	L_N	L_C
1/10	95.91mm	958.19mm
1/6	143.75mm	862.5mm
1/4	191.65mm	766.67mm

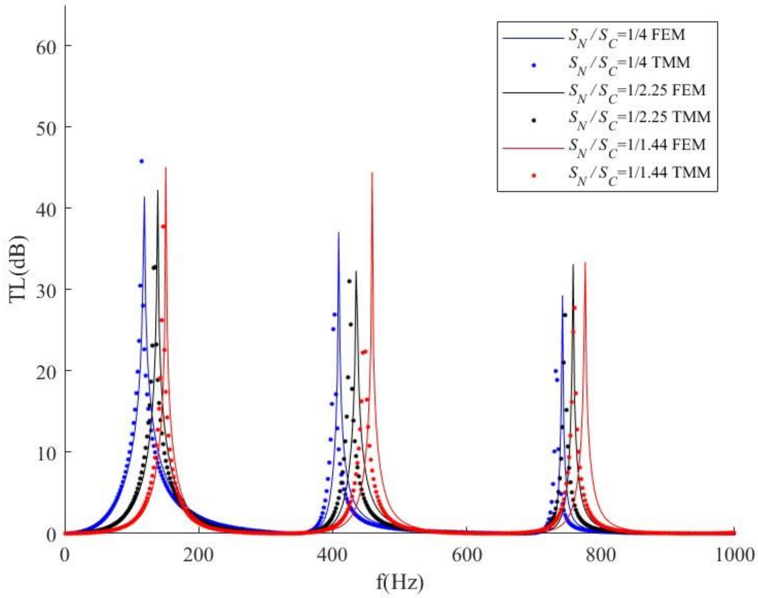

Figure 2.12 Comparison of transmission loss based on varying cross-section area ratios of the cavity (dots represent TMM prediction results, while lines represent FEM simulation results).

The effects of the cross-sectional area are also examined here. As detailed in Table 2.5, three A_N/A_C ratios are associated with three distinct expansion chamber radii, while the neck radius remains constant. The TL results are presented in Figure 2.12. From this figure, it can be observed that a greater cross-sectional area ratio is more effective in attenuating noise in the lower-frequency band. The Curved HR with an A_N/A_C ratio of 1/4 exhibits the lowest resonance frequency and the broadest noise attenuation band in the lower-frequency range. Conversely, a lower cross-sectional area ratio proves more advantageous for higher-frequency noise attenuation. The Curved HR with an A_N/A_C ratio of 1/1.44 displays a broader noise attenuation range and a higher resonance frequency in the higher-frequency range.

Table 2.5 Parameters of A_N and A_C of the Curved HR in Figure 2.12

A_N/A_C	R_N	R_C
1/1.44	21.25mm	25.5mm
1/2.25	21.25mm	31.875mm
1/4	21.25mm	42.5mm

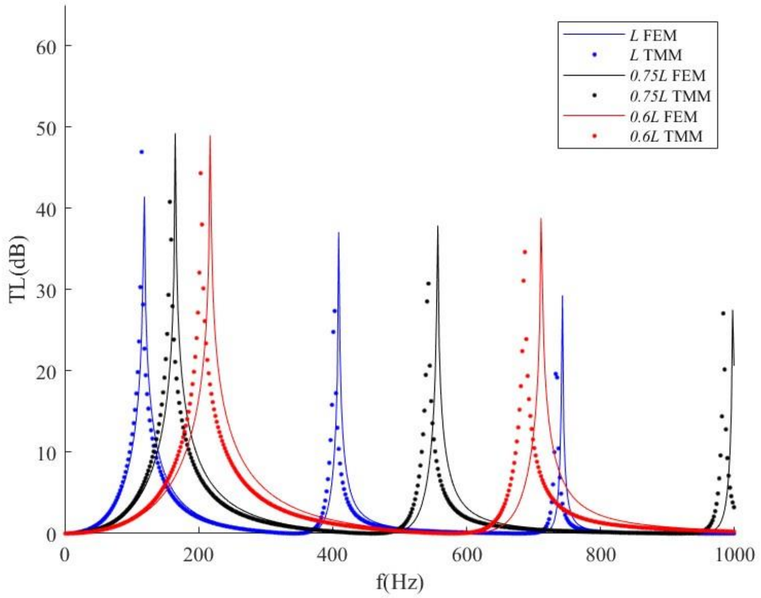

Figure 2.13 Comparison of transmission loss based on varying lengths of the Curved HR (dots represent TMM prediction results, while lines represent FEM simulation results).

Figure 2.13 illustrates the TL results for the Curved HR of different total length values. The total length has adjusted to 0.75 and 0.6 times of the initial length ($L=L_C+2L_N=1.15$m), while L_C and L_N are scaled down accordingly, keeping the radius of the neck and cavity constant. As depicted in Figure 2.13, a shorter total length can lead to a broader TL bandwidth, with the TL peak shifting into a higher frequency range that can even exceed 1000Hz, the upper bound of this study. Additionally, the Curved HR model with 0.6L shows a greater discrepancy compared to the FEM results, probably because of the length of the neck being too short. According to the research of Ingard (Ingard, 1953), an end correction is non-negligible to enhance the correctness of calculating the TL results of the short-neck HR. Therefore, the TMM calculation result of a short L_N case (0.6L) is not accurate enough. The results from TMM and FEM suggest that Curved HRs with a shorter length provide a wider sound attenuation bandwidth, but the resonance frequency would move to high frequencies.

2.5 Summary

In this chapter, the numerical, experimental and theoretical methods employed in the current study have been presented. A CFD-Acoustic coupled numerical simulation has been applied to finish this study. The detailed simulation results will be presented in the following chapter.

A flow duct system is designed and manufactured to assess the sound absorption performance of the HR-based muffler. The velocity profile of the flow duct system and the sound absorption characteristics of the anechoic termination are tested. The performance of the flow duct demonstrates that it can produce a steady grazing flow with an average speed ranging from 0 to 20 m/s, with up to 80% of reflected acoustic waves being absorbed within the frequency of 200 to 1000 Hz. The characteristics of the flow duct system demonstrate that it is suitable for testing the sound absorption performance of the side-branch mounted mufflers under grazing flow conditions.

TMM has been adopted to determine the sound transmission loss of the ductwork system with side-branch mounted mufflers. By introducing TMM, a Curved HR is proposed in this section. The design of the Curved HR allows for reduced space occupancy while preserving the same neck and cavity volumes as traditional HR. The TL performance of the Curved HR is analyzed by using TMM, with results indicating that the designed

Curved HR muffler is effective for reducing low-frequency noise. Besides, a parametric study is performed to examine how geometrical parameters influence the TL results of the Curved HR. Transmission loss results for the Curved HR are obtained through TMM and FEM, focusing on variations in length ratios, cross-sectional area, and total lengths. These findings offer valuable insights for selecting geometric parameters to optimize duct noise reduction with the Curved HR.

Chapter 3

Numerical investigation of a dual Helmholtz resonator under grazing flow conditions

3.1 Introduction

In this chapter, a numerical analysis has been performed to discuss the noise attenuation ability of a dual HRs system under different flow Mach numbers. The dual HRs system was first introduced by Xu *et al*. (Xu, Selamet and Kim, 2010). This kind of HRs system includes a pair of necks and cavities connected in series that are side-branch mounted on a main duct. Cai *et al.* compared the acoustic characteristics of different HRs array configurations theoretically and numerically (Cai and Mak, 2018a). The results showed that dual HR could increase the broadband noise reduction ability. In practical applications, the dual HR can utilize the constrained space and provide two resonance frequencies, which means it can be an effective muffler in ductwork systems. However, it is still not clear about the relationship between the transmission loss performance of the dual HRs system and the geometry parameters under grazing flow conditions, particularly regarding the acoustic behavior of the additional second neck and cavity. It can be seen that these results could provide help in designing high-performance duct mufflers.

3.2 Simulation model

As illustrated in Figure 3.1, the geometry for the numerical simulation features a dual HR model mounted on one side of the rectangular main duct. The dual HRs include two necks and two cavities, and these parts are connected in series. The volumes of the two cavities are *V1* and *V2*. The lengths of the two necks are *Ln1* and *Ln2*. This study will examine the influence of neck length and cavity volumes. The lengths of the neck are changed from 0cm to 7.62cm (0in to 3in), and the cavity volumes are changed from 926.3 cm^3 to 1852.6 cm^3. The flow Mach number, *Ma*, ranges from 0 to 0.12. Table 3.1 summarizes the geometric dimensions and flow conditions for the dual HR system.

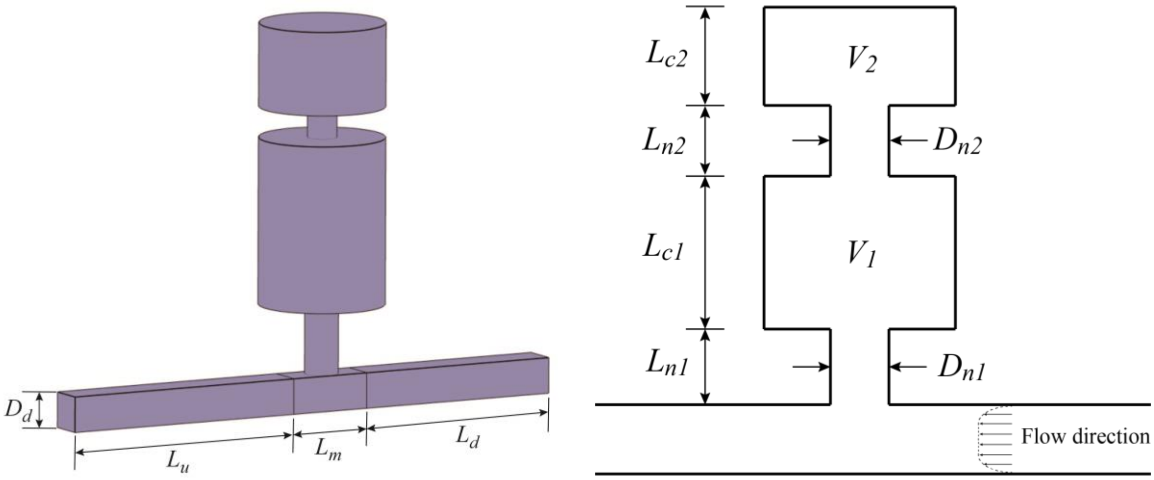

(a) (b)

Figure 3.1 Schemes of a dual HRs system: (a) 3D model, (b) cross-section view.

Table 3.1 Geometric parameters and flow conditions of the dual HRs system.

Parameters	Values	Parameters	Values
D_d	4.3cm	*Dn2*	3.5cm
Lu	25 cm	*V1,V2*	926.3-1852.6cm^3
Lm	10 cm	*f*	1-1000Hz
L*d*	30 cm	*P0*	101.325kPa
Ln1	8.5 cm	*c*	343m/s
Lc1,Lc2	10.16-20.32 cm	*Ma*	0-0.12
Ln2	0-7.62 cm	*ρ0*	1.2kg/m3
Dn1	4 cm	*T0*	293.15K

By considering the symmetry of the geometry model, numerical simulations are performed for half of the dual HRs model. For CFD simulations, the inlet is configured as a fully developed flow condition, while the outlet is designated as a pressure outlet. The boundaries of the main duct and the dual HRs are set as no-slip walls. For the acoustic simulations, the upstream and downstream are implemented as perfectly matched layers (PML) to minimize the reflected acoustic wave. A background acoustic wave is generated in a small area behind the upstream PML. The boundaries of the acoustic simulations are set as slip wall and adiabatic conditions. Figure 3.2 shows the detailed boundary conditions.

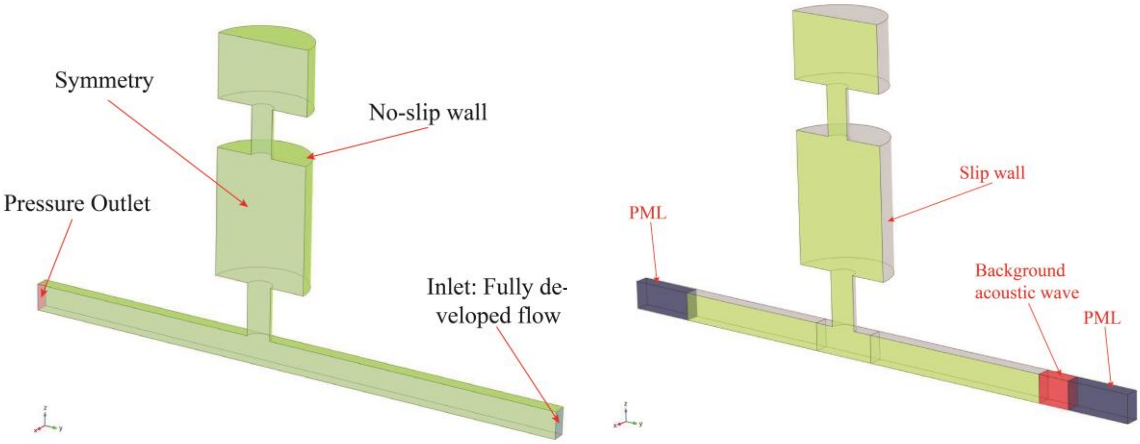

(a) (b)

Figure 3.2 Boundary condition of the simulation models. (a) CFD module; (b) acoustic model.

As shown in Figure 3.3, two different meshes are used to simulate the flow and acoustic field. To capture the turbulence accurately, it is necessary to refine some specific areas of the numerical mesh. Figure 3.3(a) illustrates the mesh refinement near the boundary layer, resonator neck, and junction area between the resonator and main duct. A swept mesh is used to reduce the computational resources near the main duct. Figure 3.3(b) illustrates the computational mesh for the acoustic simulation. Swept meshes are also used in the PML region. The other parts used an unstructured tetrahedral mesh.

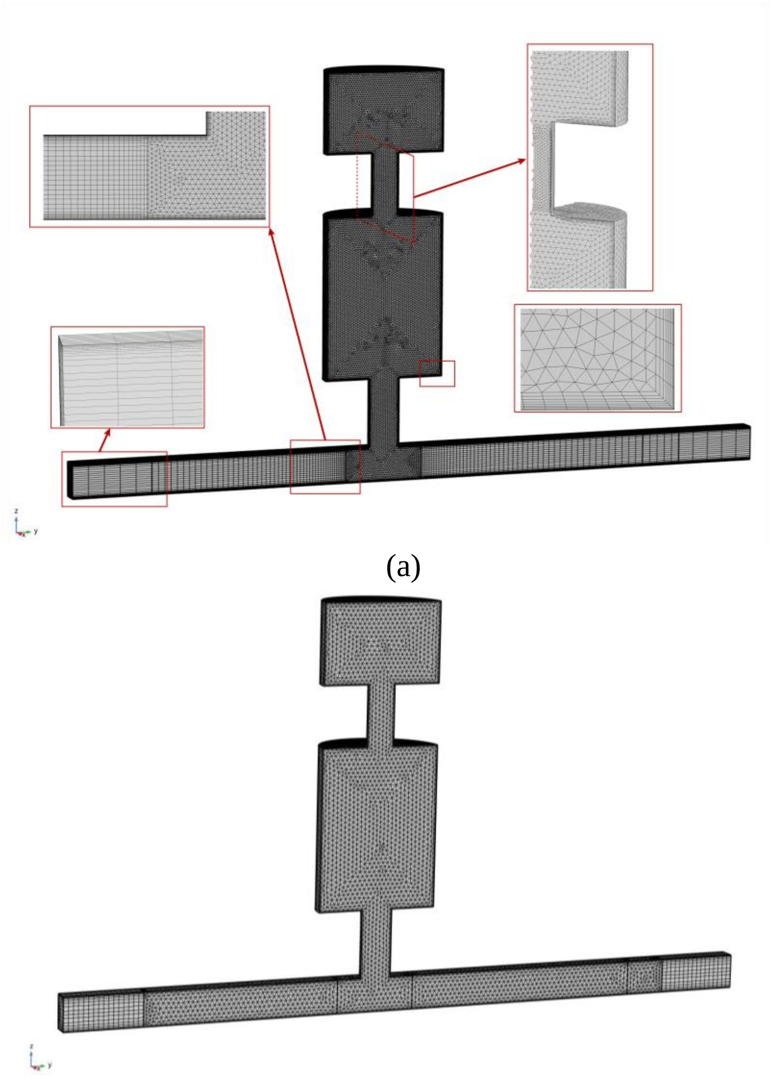

(a)

(b)

Figure 3.3 Schematics of meshes distribution. (a) mesh for CFD simulation with details of the inlet, boundary layer, resonator neck, and junction area; (b) Mesh for acoustic simulation.

This section presents a grid convergence study conducted to determine an appropriate mesh for completing the CFD simulation. As shown in Figure 3.4, four sets of meshes are used to calculate the velocity distribution near the neck inlet along the x-axis. The numbers of grids are 662229 (mesh1), 753,394 (Mesh2), 874,094 (mesh3), and 1,271,660 (mesh4). Finally, Mesh3 has been chosen for CFD simulation. The CFD grid comprises a total of 874,094 cells, while the acoustic grid consists of 284,937 cells.

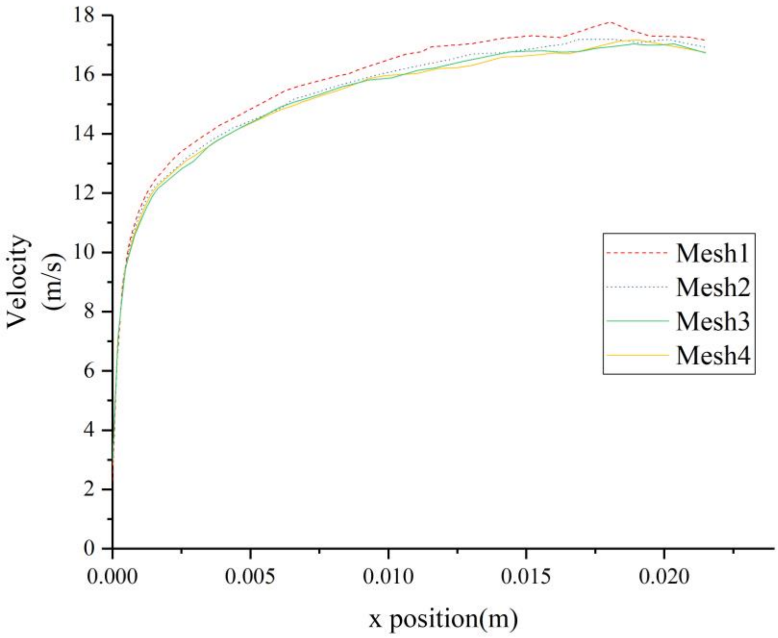

Figure 3.4 Grid convergence verification.

3.3 Numerical validation

The results of the numerical simulation are compared with the experiments performed by Kim and Selamet (Kim and Selamet, 2020) to examine the accuracy of the acoustic simulation method. All geometric dimensions in this simulation match those used in the experiments, and the flow Mach numbers also correspond to the experimental conditions (*Ma* =0, 0.05, and 0.1). The frequency range selected for this analysis is 1-300 Hz. Figure 3.5 presents the transmission loss results for the dual HR system at various flow Mach numbers, with experimental data from Kim and Selamet. The transmission loss is defined by Equation (3.1):

$$TL = 20\log_{10}\left(\left|\frac{P_{in}}{P_{out}}\right|\right) \tag{3.1}$$

where P_{in} is the incident acoustic pressure of the inlet side, and P_{out} denotes the transmitted acoustic pressure at the outlet side. It can be seen that the numerical simulations are consistent with experiment results under different *Ma* numbers, indicating that our simulation model can accurately capture the acoustic field inside the ductwork system.

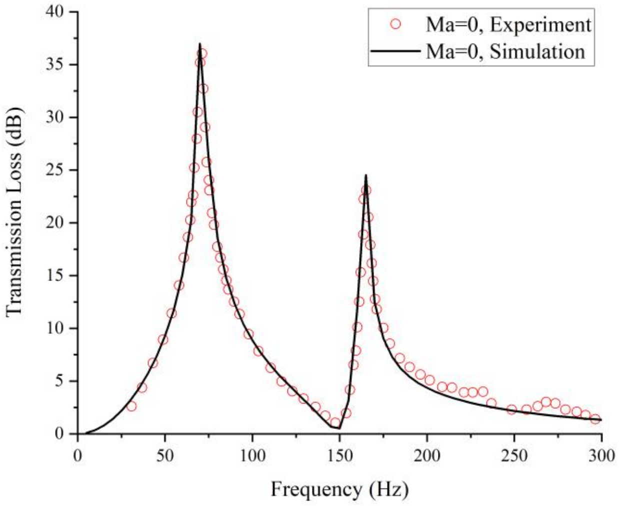

(a)

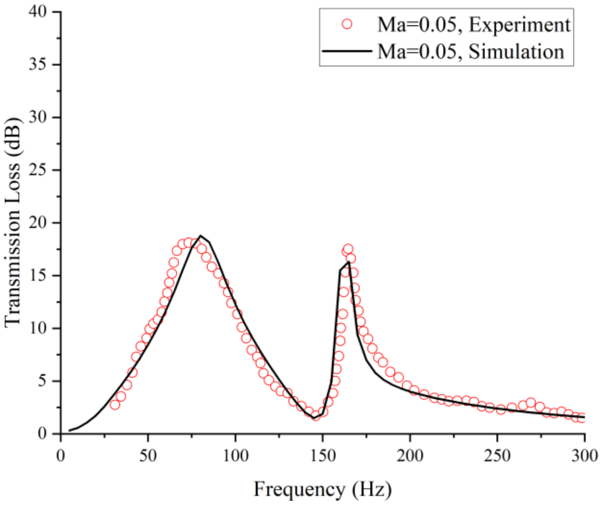

(b)

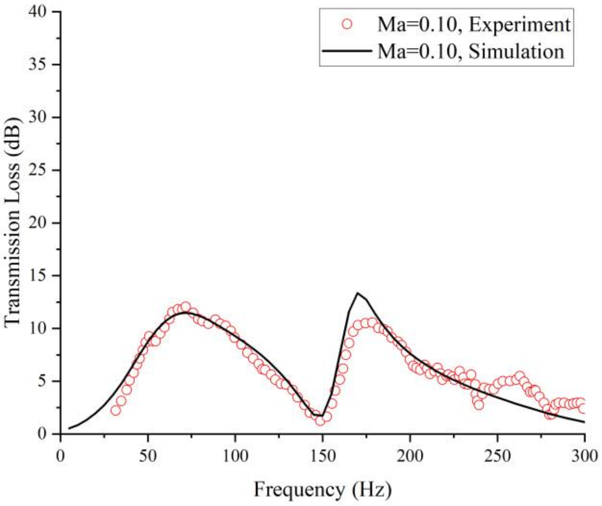

(c)

Figure 3.5 Comparison of the TL results between existing experiments(Kim and Selamet, 2020) and present simulations (a) *Ma*=0; (b)*Ma* =0.05; (c) *Ma* =0.1. Black lines and red dots represent the experimental and numerical results respectively.

To confirm the correctness of the CFD simulation, the velocity profile of the main duct is compared with analytical results. According to the power law, the velocity profile is determined by (Spillere, Cordioli and Boden, 2017):

$$U(y^*) = U_{max}[-4y^*(y^* - 1)]^{2/7} \tag{3.2}$$

where y^* is the non-dimensional y position, U_{max} is the maximum velocity. The main duct velocity profile at 5cm before the dual HRs model is calculated by using Equation (3.2). As shown in Figure 3.6, when *Ma*=0.05, the time-averaged velocity profile of the CFD simulation is consistent with analytical results, which means the flow field of the simulation is correct.

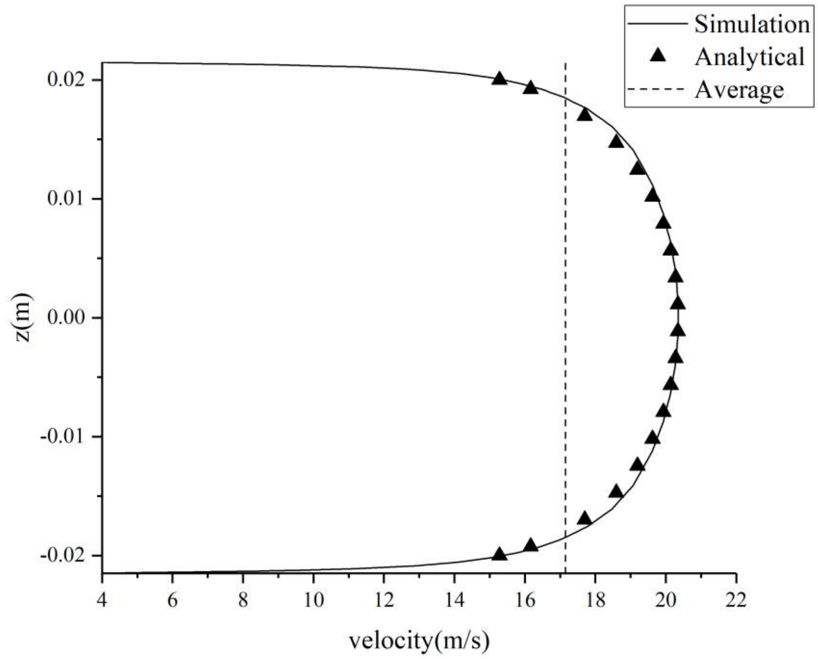

Figure 3.6 The velocity profile of simulation (solid line), analytical (symbols) and averaged result (dashed line), *Ma*=0.05.

3.4 Results and discussion

3.4.1 Effect of the neck length between two cavities

This section examines the impact of the neck length between the two cavities of the dual HR system. An HR could be regarded as a mass-spring system.(Cai, Mak and Wang, 2017), and the mass is fully determined by the neck geometry. Therefore, for a dual HRs system, the neck length between the two cavities can influence the sound absorption ability. The transmission loss results for various second neck lengths are evaluated and summarized in Figure 3.7. The flow Mach numbers are selected as 0.05 and 0.1, which are typical flow speeds in the duct system of the building acoustic research area. Neck lengths are selected as 0in, 0.5in, 1.5in, and 3in. The geometrical parameters of the main duct and cavity volume are the same as the dual HRs model in Section 3.2.

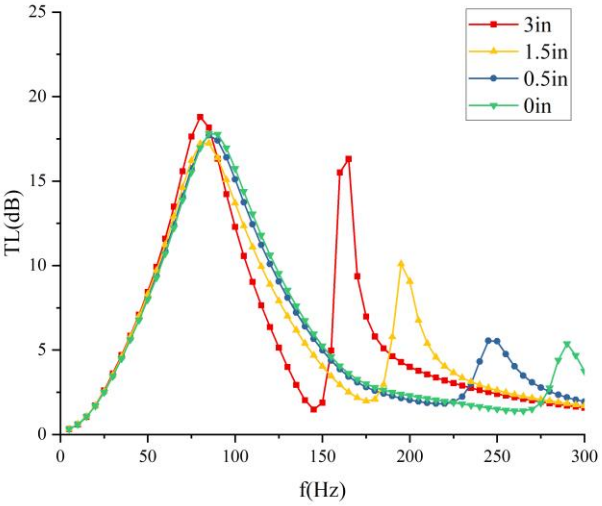

(a)

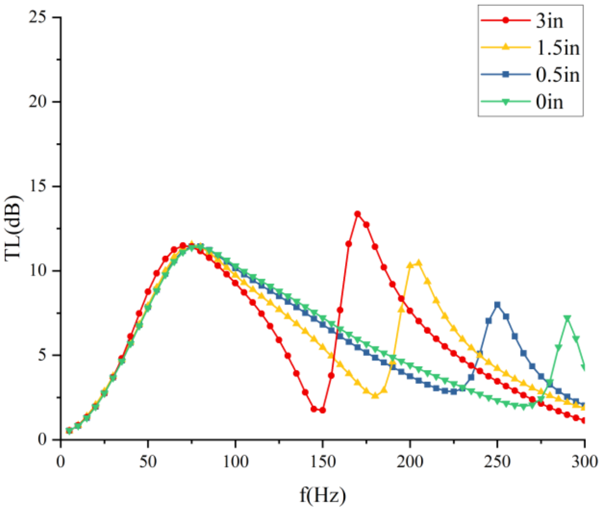

(b)

Figure 3.7 Transmission loss results of various neck length values (a) *Ma*=0.05; (b) *Ma*=0.1. The first neck length is 3.35in, and the second neck lengths are selected as 0in, 0.5in, 1.5in, and 3in.

For the dual HRs system, two resonant peaks of the transmission loss are present within the frequency band between 1-300 Hz. It is evident that as the length of the second neck increases, the first resonant frequency stays constant, while the second resonant frequency decreases. Additionally, the maximum transmission loss, TL_{max}, has been increased with the increase of the length of the neck. In particular, with a long neck length (3in), the second TL_{max} is higher than the first peak when Ma=0.1. Table 3.2 summarizes the resonance frequencies and TL_{max} for various Mach numbers and neck lengths. For the first TL peak, TL_{max} has decreased about 7dB when Ma is increased from 0.05 to 0.1. However, with a shorter neck length (0in and 0.5in), the second TL peak is increased around 3 dB. These results indicate that the neck length significantly affects the noise attenuation ability of dual HR systems. Specifically, increasing the second neck length can increase the TL performance, and a short neck length can increase the TL performance under a higher flow rate.

The resonance frequency of an HR can be calculated using Equation (3.3):

$$\omega_0 = c_0\sqrt{\frac{S_n}{l_n V_c}} \tag{3.3}$$

where ω_0 represents the resonance frequency, l_n denotes neck length, S_n denotes the sectional area of the HR neck, and V_c denotes the cavity volume. In this study, the dual HRs have two resonance frequencies. Each resonance frequency is decided by the geometrical parameters of each cavity and neck region. According to Equation (3.3), the second resonance frequency is decreased when the second neck length increases. Besides, the length and radius of the first neck are kept constant. Hence, the first resonance frequency stays the same in Figure 3.7.

Table 3.2 The resonance frequency and maximum transmission loss for different Mach numbers and neck lengths.

		Peak1		Peak2	
		Frequency (Hz)	TL(dB)	Frequency (Hz)	TL(dB)
Ma=0.05	0in	85	17.81	290	5.37
	0.5in	85	17.7	245	5.55
	1.5in	85	17.23	195	10.09
	3in	80	18.8	165	16.3
Ma=0.10	0in	80	11.41	290	7.22
	0.5in	75	11.45	250	7.99
	1.5in	75	11.45	205	10.44
	3in	70	11.48	170	13.36

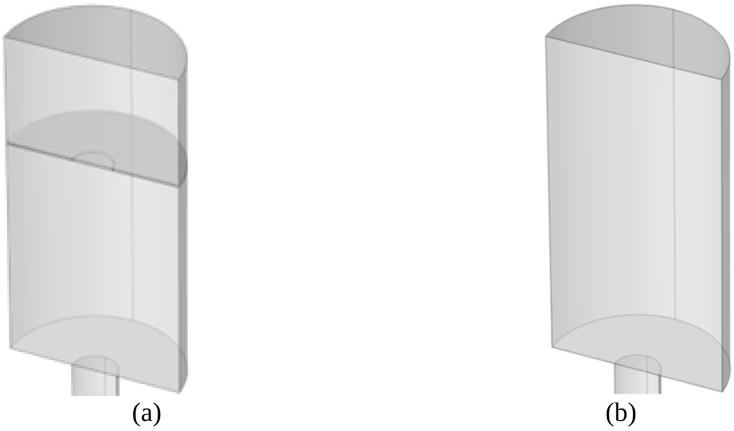
(a) (b)

Figure 3.8 Diagram of the main duct with a side-branch mounted HR model. (a) dual HRs system with neck length *Ln*=0; (b) single HR system.

As depicted in Figure 3.8(a), when the second neck length *Ln2* equals zero, two cavities of the dual HRs system are connected and separated by a perforated wall. If this perforated wall is removed, the dual HRs system can be regarded as a single HR with the same cavity volume (Figure 3.8(b)). The sound transmission loss of these two structures is compared and shown in Figure 3.9. The thickness of the perforated wall of the dual HRs model used in this study is 2mm, and other geometric parameters are the same as the model in Section 3.1. The cavity volume of the single HR model is 2778.9 cm^3, which is the same as the total volume of the dual HRs model. It can be observed that dual HRs can provide another TL peak than single HR. For the first TL peak, when Ma=0.05, the TL_{max} of the single HR is higher than that of the dual HRs. When Ma=0.1, the first TL_{max} is nearly the same. Therefore, the noise attenuation ability of dual HRs is better than that of a single HR under higher flow rate conditions.

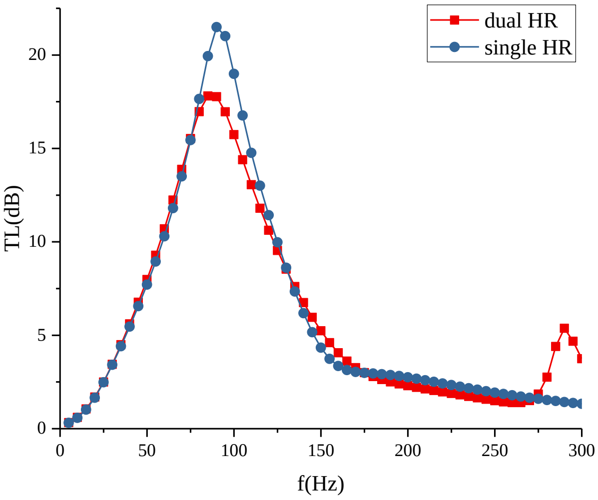

(a)

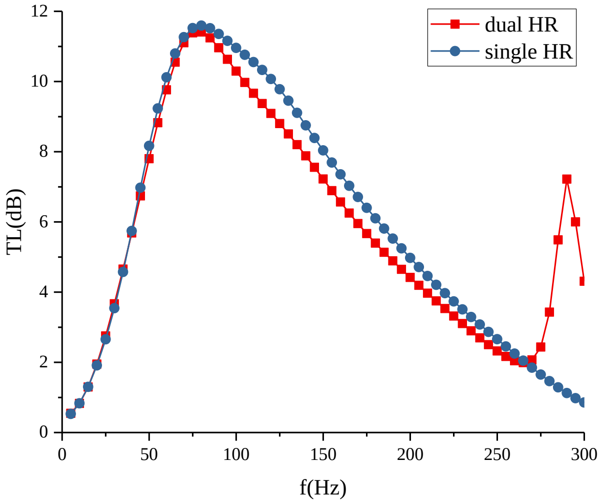

(b)

Figure 3.9 Comparison of the transmission loss versus frequency for a dual HRs system and a single HR. (a) *Ma*=0.05; (b) *Ma* =0.1

3.4.2 Effect of the cavity volume

The impact of cavity volume is examined and illustrated in Figure 3.10. In this study, the total cavity volume of all the dual HRs models is *V1*+*V2*=22778.9 cm^3, while the neck length and main duct geometrics are the same as the parameters in Section 3.2. Table 3.3 presents the detailed cavity volumes of each dual HRs system. The influence of cavity volume has been studied under two different flow velocity conditions: *Ma*=0.05 and *Ma*=0.10. It can be observed that changing the cavity volume influences the resonant peaks and the resonant frequency. When *V2* is increased, the second resonant frequency tends to decrease, but the first resonant frequency tends to increase. When *Ma*=0.05, increasing *V2* leads to a higher second resonant peak. When *Ma*=0.1, resonant peaks are much smaller owing to the high flow rate, and the effect of changing the cavity volume is not obvious. Therefore, adjusting the cavity volume is an effective way to improve the noise attenuation with the lower grazing flow rate conditions; however, it is not suitable for a higher flow rate.

In this study, Equation (3.3) can explain the variation of the resonance frequency by changing the cavity volume. From Design1 to Design 3, the first cavity volume *V1* keeps decreasing. According to Equation (3.3), the resonance frequency increases as cavity volume decreases. Therefore, the first resonance frequency is increased from 60Hz to 80Hz when *Ma*=0.05. Besides, it is evident that the variation of the second resonance frequency is also consistent with Equation (3.3).

Table 3.3 Characteristics of the dual HRs system with different cavity volume

Dual HRs design	*V1*(cm^3)	*V2*(cm^3)	*V1/V2*
1	1852.6	926.3	2
2	1389.5	1389.5	1
3	926.3	1852.6	0.5

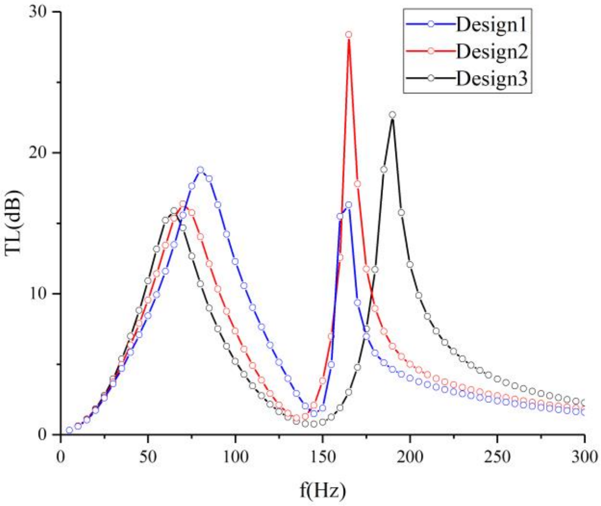

(a)

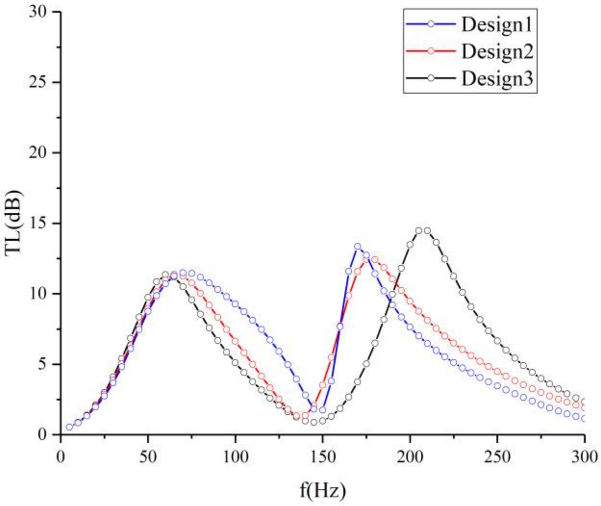

(b)

Figure 3.10 Transmission loss results versus frequency for different cavity volume values (a) *Ma*=0.05; (b) *Ma*=0.1

Figure 3.11. shows the flow field results of the dual HRs system with different cavity volumes. The velocity magnitude inside the cavity has been converted to a non-dimensional Mach number ($Ma=v/c_0$) to clearly show the velocity distribution. As can be seen in the figure, air entered the first cavity through the downstream side of the neck. As the air enters the cavity, the flow rate decreases gradually. Figure 3.12 illustrates the

acoustic pressure fields of the dual HRs system under the resonant frequency. The acoustic pressure inside the main duct is extremely low due to the resonance occurring. Near the downstream side of the dual HRs system, a secondary acoustic wave source has emerged as a result of the combined effect of acoustic wave and grazing flow. This phenomenon is also mentioned by Dastourani and Bahman-Jahromi (Dastourani and Bahman-Jahromi, 2021). The secondary acoustic wave source can generate noise. Consequently, the noise attenuation ability of the dual HRs system is reduced owing to the grazing flow effect.

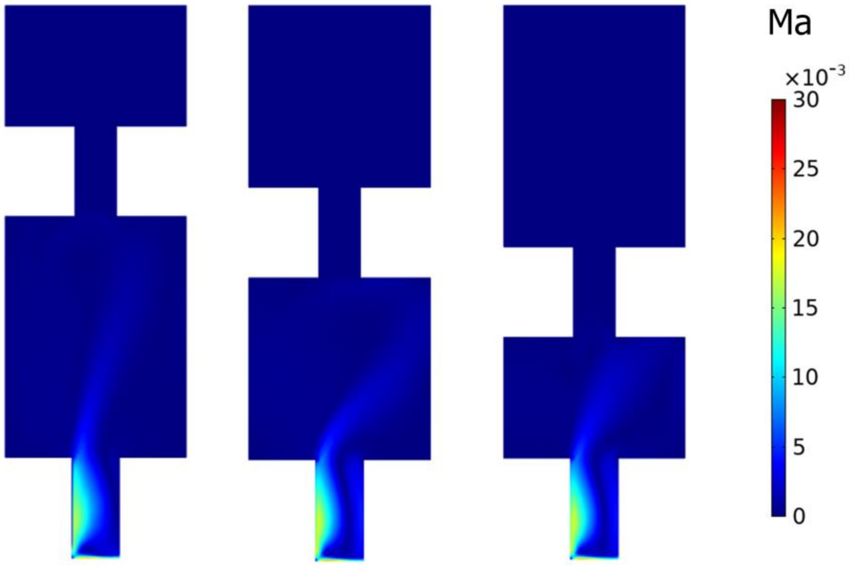

(a)

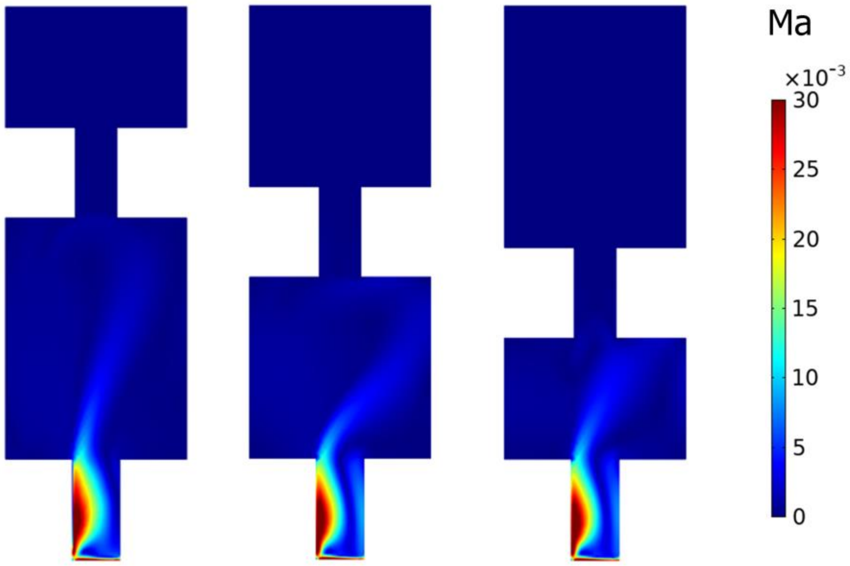

(b)

Figure 3.11 Velocity fields of dual Helmholtz resonators with different cavity volumes under different grazing flow speeds (a) *Ma*=0.05; (b) *Ma*=0.1

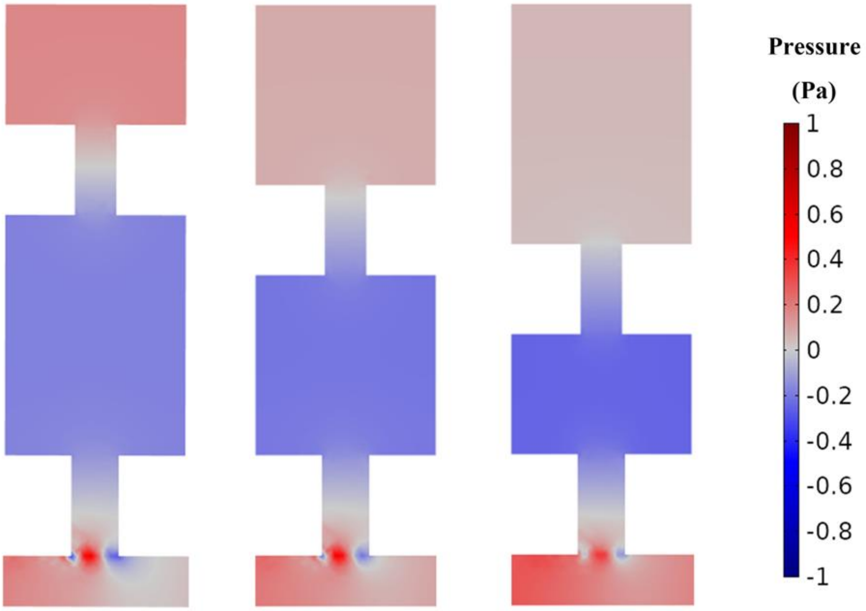

(a)

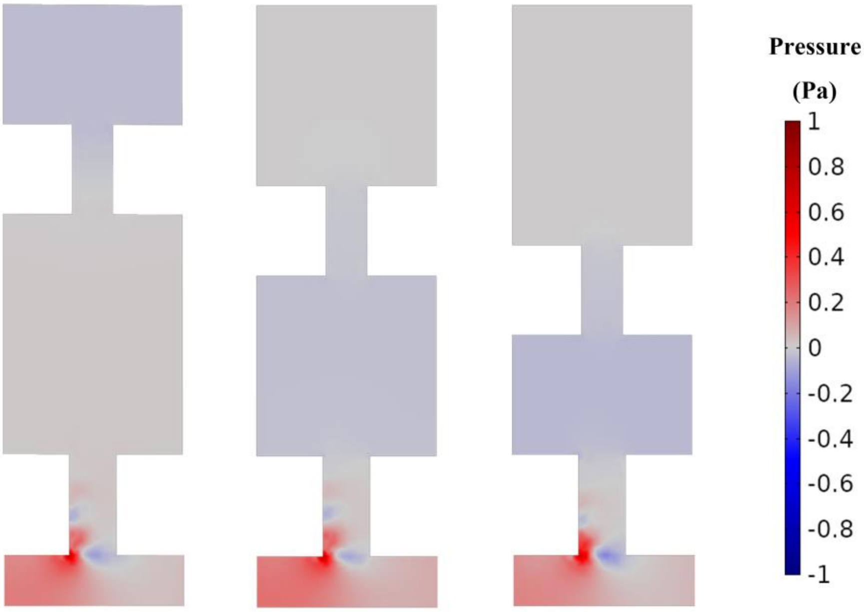

(b)

Figure 3.12 Acoustic pressure fields of dual Helmholtz resonators with different cavity volumes under different grazing flow speeds (a) *Ma*=0.05; (b) *Ma*=0.1

3.4.3 Effect of the grazing flow Mach number

In this section, the flow Mach numbers are set as 0, 0.03, 0.05, 0.07, 0.10 and 0.12 to investigate the influence of grazing flow speed on the transmission loss performance. Table 3.4 summarizes the resonance frequencies and TL_{max} values for various flow Mach numbers. Figure 3.13 illustrates the impact of the grazing flow Mach number on transmission loss performance. It can be seen that as *Ma* increases, the first TL_{max} and the second TL_{max} both decreases. The first TL_{max} dropped from 37.0dB to 10.7 dB. The second TL_{max} dropped from 24.5dB to 11.0 dB. The results indicate that flow Mach number has a greater influence on the first transmission loss peak compared to the second. As *Ma* increases, the first resonance frequency is increased from 70Hz to 85Hz in the first place, and subsequently drops back to 70Hz. The second resonance frequency is increased from

165Hz to 170Hz. The resonance frequency of HR is influenced by acoustic impedance. As the Mach number increases, the acoustic impedance also rises, resulting in a higher resonance frequency. Conversely, a higher Mach number also produces higher background noise, which may reduce transmission loss performance in the higher frequency range. The resonance frequency is influenced by these two factors. Therefore, as *Ma* increases, the first resonance frequency increases first and then decreases in this study.

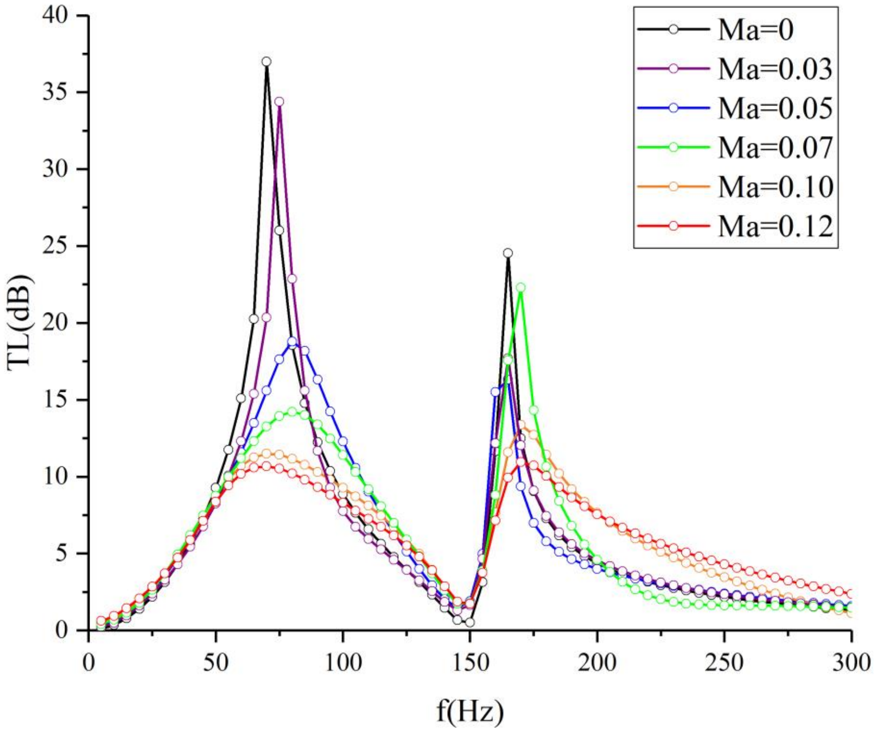

Figure 3.13 Transmission loss results for different flow Mach numbers.

Table 3.4 Summary of the resonance frequency and TL_{max} for different Mach numbers

Ma	Peak1		Peak2	
	Frequency (Hz)	TL (dB)	Frequency (Hz)	TL (dB)
0	70	37.0	165	24.5
0.03	75	34.4	165	17.7
0.05	80	18.8	165	16.3
0.07	80	14.2	170	22.3
0.10	70	11.5	170	13.4
0.12	70	10.7	170	11.0

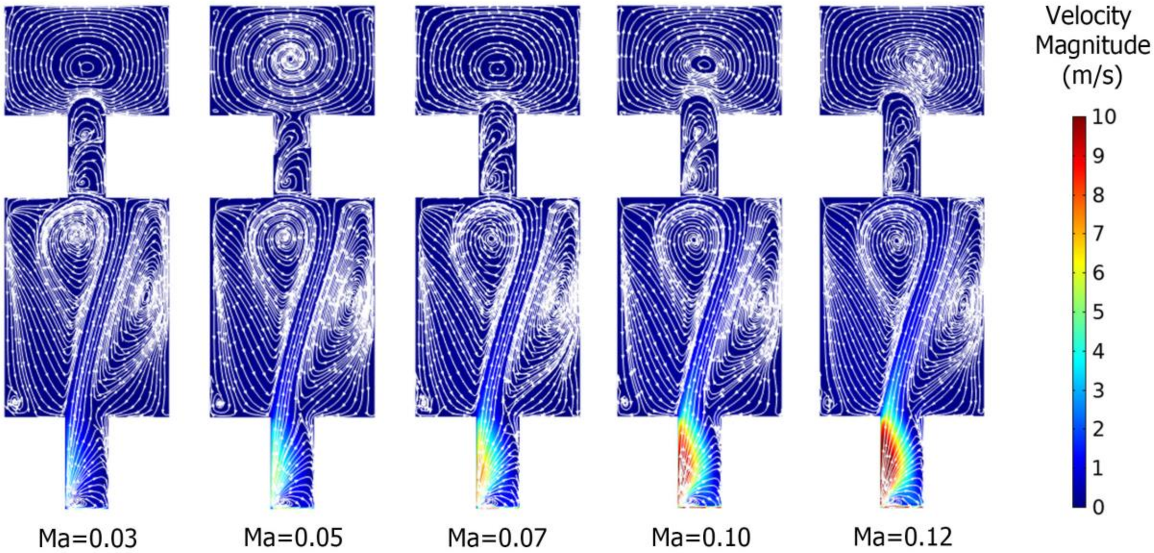

Figure 3.14 Velocity fields and streamlines of the dual HRs system under different flow Mach numbers

Figure 3.14 shows the velocity magnitude and streamlines of the dual HRs system under different flow Mach numbers. As indicated by the streamlines, the main flow enters the first cavity through the left edge of the first neck. Afterward, the streamlines inside the first cavity indicate two vortex centroids emerged. One of the vortices is positioned just below the second neck and rotates counterclockwise, while the other vortex is situated near the center of the cavity boundary. The airflow near the second neck also generates two vortices rotating in opposite directions. Finally, airflow exits the first cavity from the right side of the cavity. When the flow rate Mach numbers increase from 0.03 to 0.12, the locations of the vortex centroids remain unchanged. The velocity magnitude indicates that as Ma increases, the average velocity in the first cavity increases. However, the velocity magnitude inside the second neck and cavity tends to be zero. The velocity magnitude shows that the first neck is located between a high flow rate area (main duct) and a low flow rate area (first cavity). The velocity difference causes the velocity magnitude inside the first neck to reach nearly 10m/s. Conversely, the velocity magnitude within the first and second cavities is lower than the velocity magnitude inside the main duct, leading to a tendency for the velocity magnitude in the second cavity to approach zero.

3.5 Summary

This chapter presents a numerical analysis aimed at investigating the effect of the geometric parameters and Mach numbers on the sound attenuation ability of the dual HRs model under grazing flow conditions. The effect of neck length is first investigated. The results indicate that the second resonant frequency and TL_{max} increase as the length of the second neck is increased. Compared with the single HR system, the dual HRs model can provide another TL peak and is more suitable for mufflers under higher flow rate conditions. Altering the cavity volume significantly affects the resonance frequency and the TL_{max} under lower flow rate conditions; however, it is not suitable for higher flow rate conditions. The acoustic pressure field results demonstrate that a secondary acoustic wave source emerges downstream of the neck. Increasing the Mach number of grazing flow leads to a reduction in the TL_{max} of both peaks, while the second resonance frequency increases. In contrast, the first resonance frequency initially rises and then falls. The transmission loss results suggest that the flow Mach number has a greater impact on the first transmission loss peak compared to the second. The velocity field results reveal that as Ma increases, more air enters the first cavity, and the average velocity in the first cavity is also increased. However, the velocity magnitude inside the second neck and cavity tends to be zero. Understanding the relationship between the noise absorption ability of the dual HR system and the geometric parameters as well as the flow Mach number can be beneficial for designing noise mufflers.

Chapter 4

Experimental investigation of the Helmholtz resonator under grazing flow conditions

4.1 Introduction

When grazing flow occurs in the ductwork system, the sound absorption of the side-branch mounted HR could be affected. Additionally, the interaction between the shear layer and the background grazing flow can introduce a new noise source (P. Wang *et al.*, 2018). These two effects pose challenges in investigating the noise attenuation ability of the HR model under different grazing flow conditions. Current research has focused on the flow mechanics near the orifice, with little attention given to the flow field within the neck regions of HR. In this chapter, an acoustic experiment is performed to assess the transmission loss results of an HR model under different grazing flow speeds. A PIV measurement experiment is performed to measure the fluid characteristics near the HR neck. An empirical formula is developed to estimate the transmission loss performance of the HR model under grazing flow conditions.

4.2 Transmission loss of a Helmholtz resonator

Figure 4.1 illustrates the experimental configuration used to test the transmission loss result of an HR model. The test rig is consisted of a silent centrifugal fan, a diffusion section, a flow straightener, a loudspeaker, and two anechoic terminations. The main duct of the experimental setup features a square cross-section with dimensions of 10cm×10cm, resulting in a cutoff frequency of approximately 1700 Hz. For this research, the upper-frequency limit is set at 800 Hz to ensure that only plane waves are present inside the main duct. An 80W loudspeaker (OPEL AP 6510C8) is amplified using a B&K 2706 amplifier as the sound source to minimize the influence of background noise in the room. This sound source can generate acoustic waves of a sound pressure level (SPL) of more than 110 dB. The centrifugal fan is installed inside a soundproof box to reduce the noise of the grazing flow. Two anechoic terminations are installed upstream of the loudspeaker and downstream of the microphones to reduce the acoustic wave reflection. A signal generator (NTI MR-PRO) is connected to the amplifier to generate white noise, and four free-field microphones (B&K 4189) are flush-mounted near the test section to collect the acoustic signals of the HR model. The microphones are connected to the B&K 3052 PULSE system to log the data. The rotation frequency of the centrifugal fan can be controlled by manipulating the variable frequency drive, allowing for adjustment of the airflow velocity in the duct within the range of 0-20 m/s. This range of airflow velocities falls within the common ventilation systems of buildings. The longitudinal distance between the centrifugal fan and the test model exceeds three meters to ensure a fully developed velocity profile.

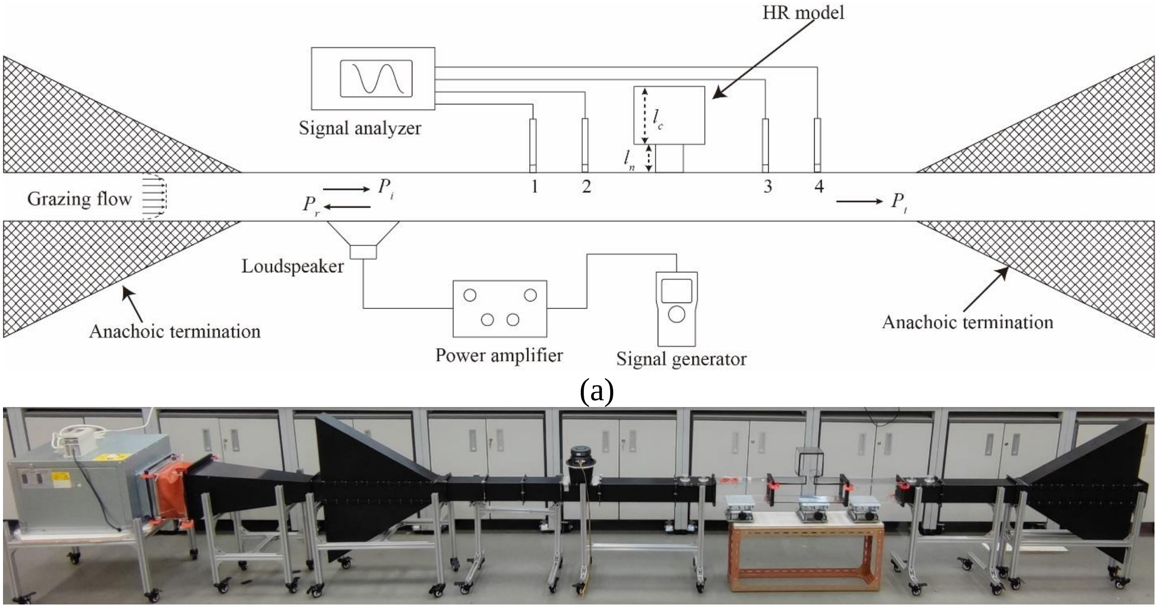

(a)

(b)

Figure 4.1 Schematic and photograph of the flow duct system and instruments for measuring the TL result under grazing flow conditions

In this experiment, the four-microphone method has been employed to measure and calculate the transmission loss result of the test sample. As depicted in Figure 4.1, the acoustic pressure at positions 1 and 2 on the upstream side of the resonator can be expressed as follows:

$$P_1 = P_i e^{-jk^+ x_1} + P_r e^{jk^- x_1} \tag{4.1}$$

$$P_2 = P_i e^{-jk^+ x_2} + P_r e^{jk^- x_2} \tag{4.2}$$

where $k^+ = k_0/(1 + Ma)$ and $k^- = k_0/(1 - Ma)$, $Ma = U/c$ denotes the flow Mach number, P_i and P_r denote the acoustic pressures of the incident and reflected acoustic wave, k_0 represents the acoustic wave number, and c denotes the sound speed of air. Δx represents the distance between positions 1 and 2 of this flow duct system, which is equivalent to the distance between positions 3 and 4. Then, the incident wave can be solved by:

$$P_i = \frac{P_1 e^{j\frac{k_0}{1-Ma}x_2} - P_2 e^{j\frac{k_0}{1-Ma}x_1}}{2j\sin\frac{k_0\Delta x}{1-Ma^2} e^{j\frac{k_0 Ma(2x_1+\Delta x)}{1-Ma^2}}} \tag{4.3}$$

The transmitted wave pressure amplitudes P_t also can be solved according to Equation (4.3) by using the acoustic pressure at positions 3 and 4. Therefore, the transmission loss can be calculated by(Wu and Wan, 1996):

$$\mathrm{TL} = 20\log_{10}\left(\frac{P_i}{P_t}\right) = \frac{H_{21}e^{jk^- x_2} - e^{jk^- x_1}}{H_{23}e^{jk^- x_4} - H_{24}e^{jk^- x_3}} e^{j\frac{2k_0 Ma}{1-Ma^2}(x_3 - x_1)} \tag{4.4}$$

where H_{ab} means the complex transfer function between positions a and b. In this study, Equation (4.4) would be utilized to compute the sound transmission loss (TL) result of the side-branched mounted HR model. In chapter 2, the reflected acoustic pressure is less than 10% between 100Hz and 1000Hz, which means that the anechoic terminations could eliminate most of the reflected wave to prove the accuracy of the test.

Figure 4.2 shows the TL results of the HR model at various flow speeds. The HR model used in this experiment features a rectangular neck and cubic cavity and is manufactured from Plexiglas. The neck had a length (l_n) of 5mm and a side length of 4mm, while the cavity had a side length (l_c) of 120mm. Additionally, the HR model has a width (*W*) of 100mm, which matches the geometry of the duct model. Results indicate a TL peak at around 303Hz when background flow velocity U=0m/s. As the background flow speed increases from 0m/s to 20m/s, the TL peak gradually decreases from 28.4dB to 14.1dB, and the resonance frequency increases from 303Hz to 319.5Hz. Furthermore, the transmission loss performance can be significantly affected at higher flow rates. As demonstrated in Figure 4.2(b) and Figure 4.2 (c), as the background flow rates have increased from 0 m/s to 10 m/s, the TL peak is only reduced by about 4 dB. Besides, the resonance frequency is only increased by 1 Hz. However, in Figures 4.2(d), (e), and (f), if the increment of the flow rate is higher than 10 m/s, TL peaks and resonance frequency have changed significantly. As indicated by Du *et al.* and Gikadi *et al.* (Gikadi, Föller and Sattelmayer, 2014; Du *et al.*, 2016), the variation of the TL results at a higher flow rate is due to the additional attenuation caused by interactions between the shear layer and acoustic wave.

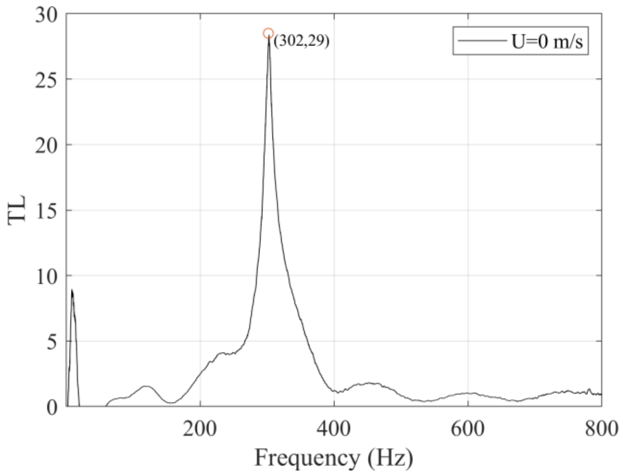

(a)

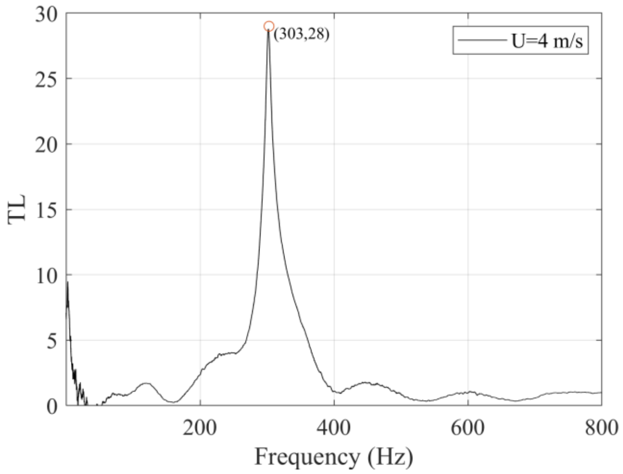
TL
Frequency (Hz)
U=4 m/s
(303,28)
0
5
10
15
20
25
30
200
400
600
800

(b)

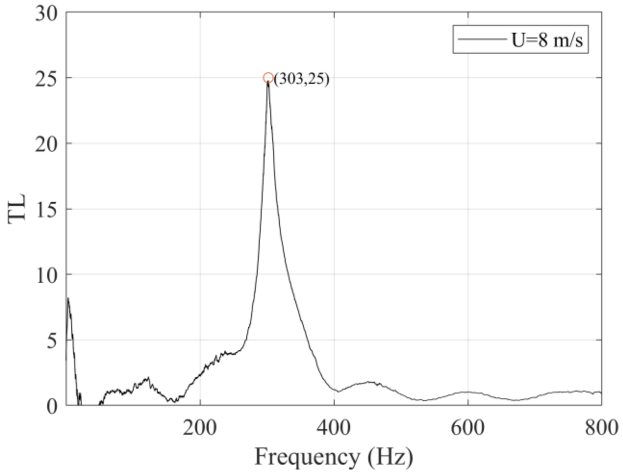
TL
Frequency (Hz)
U=8 m/s
(303,25)
0
5
10
15
20
25
30
200
400
600
800

(c)

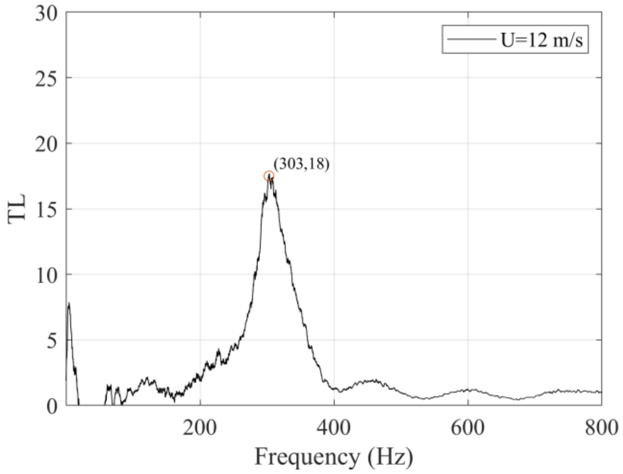
TL
Frequency (Hz)
U=12 m/s
(303,18)
0
5
10
15
20
25
30
200
400
600
800

(d)

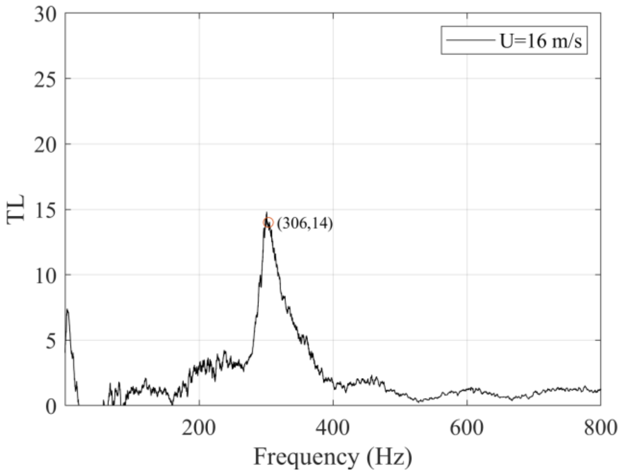

(e)

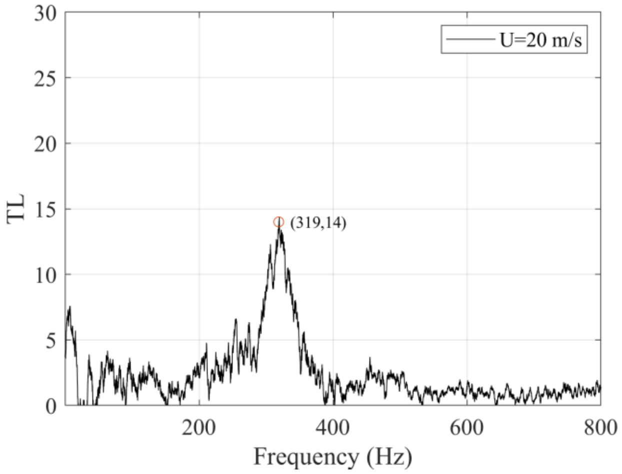

(f)

Figure 4.2 Transmission loss results of the HR model at different flow speeds. (a) U=0 m/s, (b) U=4 m/s, (c) U=8 m/s, (d) U=12 m/s, (e) U=16 m/s, (f) U=20 m/s.

4.3 Empirical transmission loss model

A commonly used prediction model can be utilized to calculate the TL results of the HR model without the background flow. This model treats HR as a mass-spring system, allowing for accurate predictions. The TL results of an HR without flow can be solved by the analytical equation(Kinsler *et al.*, 1999):

$$\mathrm{TL}_{HR} = 20\log_{10}\left|1 + \frac{\rho c}{2S_n}\frac{1}{Z_0}\right| \tag{4.5}$$

where ρ represents the air density, S_n denotes the area of the HR neck section, and Z_0 is the acoustic impedance of the HR model.

The acoustic impedance of HR model could be theoretically determined by:

$$Z_0 = R_0 + jX_0 = R_0 + j(\frac{\rho l_n'}{S_n}\omega - \frac{\rho c^2}{V}) \tag{4.6}$$

where R_0 represents the acoustic resistance, X_0 represents the acoustic reactance. V denotes the cavity volume, l_n' is the neck length modified by the end correction factor. Therefore, l_n' can be referred to Ingard and given as(Ingard, 1953):

$$l_n' = 0.85(\frac{l_n}{2})(1 - 1.25\frac{l_n}{l_c}) + 0.85(\frac{l_n}{2}) \tag{4.7}$$

Figure 4.3 compares the sound transmission loss results from theoretical predictions and experimental measurements. We could find that the TL peak and the resonance frequency fit well between experimental measurement and analytical prediction. Besides, the results denote that the HR model can be regarded as a lumped parameter model without considering the background flow. However, using Equation (4.5) to predict the transmission loss of HR is only suitable for non-flow conditions. Therefore, in the next study, the flow effect would be considered as a correction term to be added to Equation (4.5) to compute the TL performance of the HR model under grazing flow conditions.

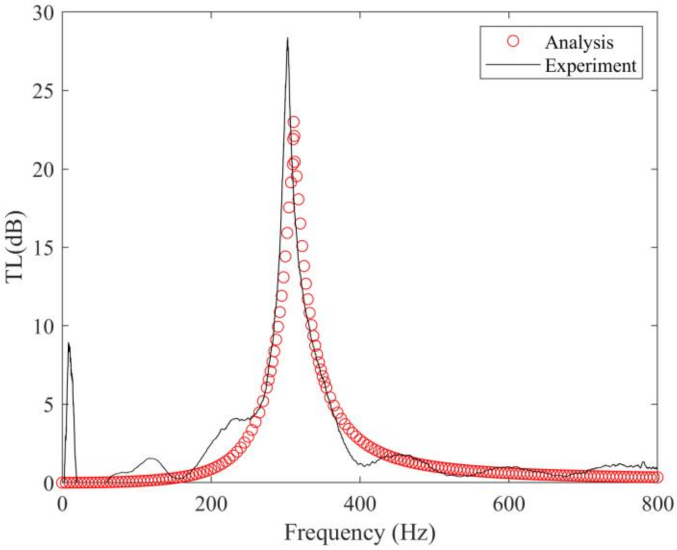

Figure 4.3 Transmission loss results for the HR model (with red dots indicating theoretical calculations and black lines representing experimental results).

An empirical transmission loss formula for calculating the TL results of the HR model is derived from experiment data using the curve fit technique. The Curve Fitting Toolbox of MATLAB is employed to analyze the experiment data. In Figure 4.3, it can be found that the resonance frequency could be considered as the symmetrical axis of the TL results. Therefore, a curve-fitting process is undertaken to find the relationship between resonance frequency and flow speed in advance. As shown in Figure 4.4, the resonance frequency begins to increase when the background flow rate becomes higher than 10 m/s. For the HR model used in this experiment, the resonance frequency in the absence of background flow f_0 is 303 Hz. Then, the resonance frequency f_r can be represented by:

$$f_r = \begin{cases} f_0 & (u < 10\text{m/s}) \\ f_0 + 0.01785u^3 - 0.5744u^2 + 6.343u - 22.9 & (u \geq 10\text{m/s}) \end{cases} \tag{4.8}$$

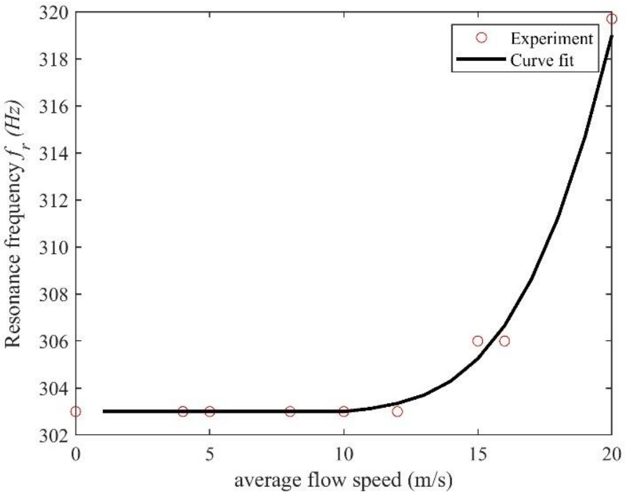

Figure 4.4 Comparison of resonance frequency between prediction and experiment result.

Once the relationship between f_0 and f_r is established, it becomes possible to derive an empirical formula for the transmission loss under varying background flow speeds. The formula can be expressed as:

$$\mathrm{TL}(f + f_r - f_0) = \mathrm{TL}_{HR}(f) - (l_n U)\mathrm{TL}_f(f) \tag{4.9}$$

where TL_{HR} is the transmission loss of HR without grazing flow in Equation (4.5), and TL_f is the transmission loss correction term. Owing to the significant symmetrical features observed in the distribution curve of TL_f, a piecewise function is employed to accurately fit the TL correction term. TL_f is nondimensionalized by geometry parameter and the grazing flow, which can be represented by:

$$\frac{\mathrm{TL}_f}{l_n U} = \sum_{i=1}^{n+1} \alpha_i f^{*n+1-i} \tag{4.10}$$

where l_n and U are neck length and flow speed, α_i represents the coefficient of curve-fitting, and f^* denotes the non-dimensional frequency, which can be represented as $f^* =$

$|(f - f_0)/f_0|$. n+1 represents the polynomial order, while n denotes the degree of the fitting. In our research, n=4 is utilized to fit the data. Figure 4.5 shows the curve fitting of $\frac{\mathrm{TL}_f}{l_n U}$ and the polynomial fitting is used to fit the experiment data. The non-dimensional TL correction term can be written as:

$$\frac{TL_f}{l_n U} = \begin{cases} a_1 f^{*4} + b_1 f^{*3} + c_1 f^{*2} + d_1 f^{*} + e_1 \, (f \leq f_0) \\ a_2 f^{*4} + b_2 f^{*3} + c_2 f^{*2} + d_2 f^{*} + e_2 (f > f_0) \end{cases} \tag{4.11}$$

where regression coefficients are:

$$a_1 = 390.27, a_2 = 36.30 \tag{4.12a}$$

$$b_1 = -764.40, b_2 = -134.74 \tag{4.12b}$$

$$c_1 = 526.87, c_2 = 171.16 \tag{4.12c}$$

$$d_1 = -149.72, d_2 = -85.35 \tag{4.12d}$$

$$e_1 = 14.13, e_2 = 13.22 \tag{4.12e}$$

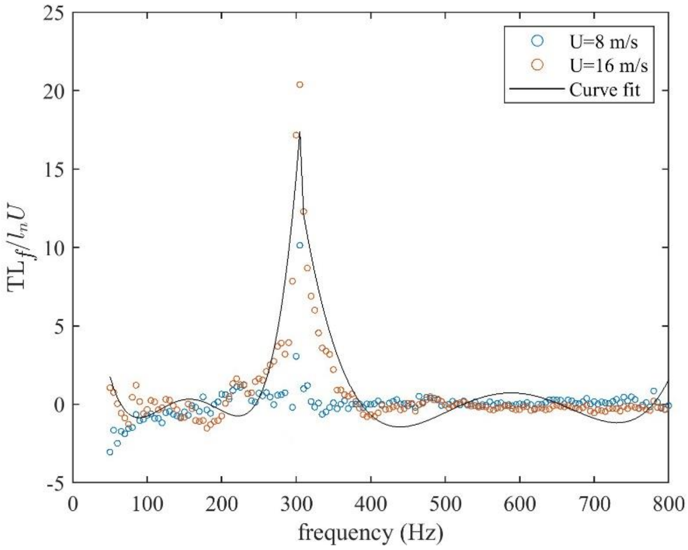

Figure 4.5. Curve fit of the non-dimensional TL correction term.

Figure 4.6 (a)-(e) shows the contrast of the TL results of a single HR model between the experiment data and the empirical formula prediction in Equation (4.10) under different grazing flow rates. As the flow rate increases, the results show that the resonance frequency of the HR model rises to a higher value, while the TL peak decreases. The empirical formula prediction fits well with the experiment data, especially under higher flow speed conditions. The results indicate that Equation (4.10) can be employed to predict the TL results of the HR model under grazing flow conditions.

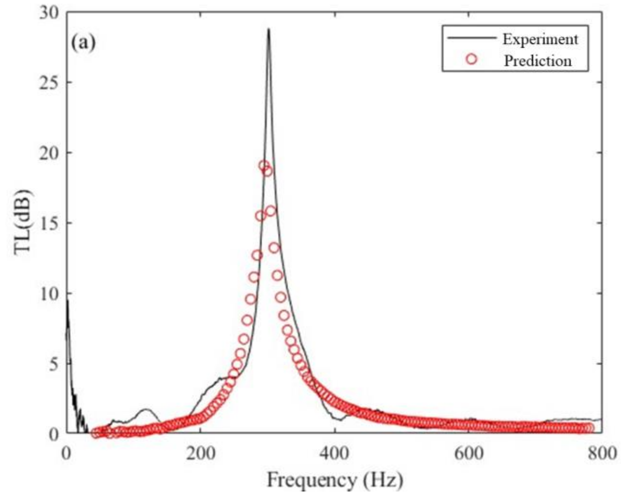
(a)
Experiment
Prediction
TL(dB)
0
5
10
15
20
25
30
Frequency (Hz)
0
200
400
600
800

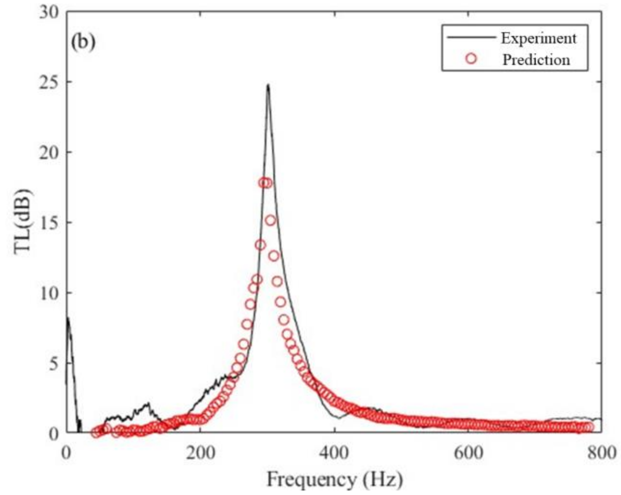
(b)
Experiment
Prediction
TL(dB)
0
5
10
15
20
25
30
Frequency (Hz)
0
200
400
600
800

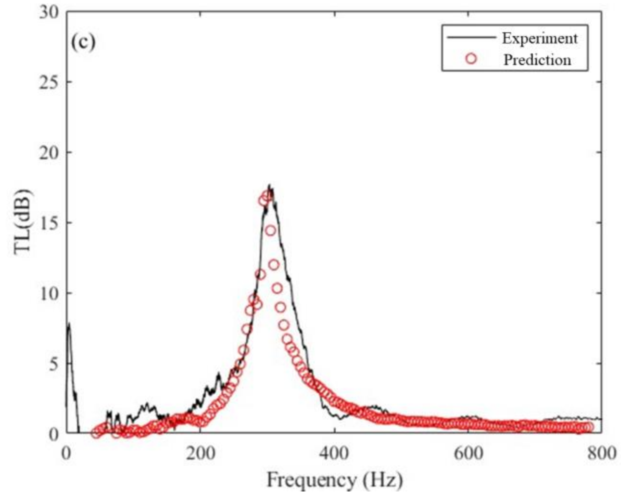
(c)
Experiment
Prediction
TL(dB)
0
5
10
15
20
25
30
Frequency (Hz)
0
200
400
600
800

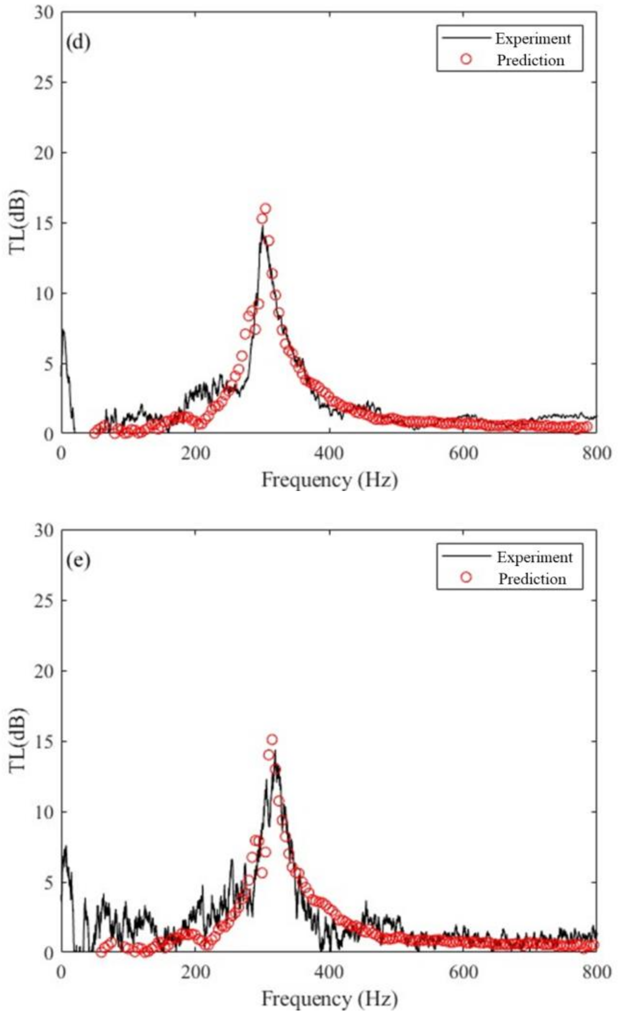

Figure 4.6 Transmission loss results of theoretical prediction and experimental measurement of a single HR.(a) U=4 m/s, (b) U=8 m/s, (c) U=12 m/s, (d) U=16 m/s, (e) U=20 m/s.

4.4 Analysis of the grazing flow effect on the Helmholtz resonator model

4.4.1 Prediction of the transmission loss of a periodic HRs array

Multiple HRs are commonly employed to improve broadband noise absorption performance. If the HRs are side-branch mounted periodically within a ductwork system, the periodic mufflers can introduce unique noise attenuation in the overall TL spectrum. In this part, the empirical model proposed in section 4.3 is utilized to predict the TL results of a muffler array consisting of periodic HRs. For the HRs array, the Transfer Matrix Method (TMM) could be utilized to determine the acoustic wave propagation. As illustrated in Figure 4.7, the acoustic wave transmission through a main duct and a side-branch mounted periodic HRs array system can be described as:

$$\begin{pmatrix} P_0 \\ \mathrm{u}_0 \end{pmatrix} = \begin{bmatrix} T_{11} & T_{12} \\ T_{21} & T_{22} \end{bmatrix} \begin{pmatrix} P_n \\ \mathrm{u}_n \end{pmatrix} = \mathbf{T}_{\text{all}} \begin{pmatrix} P_n \\ \mathrm{u}_n \end{pmatrix} \tag{4.13}$$

where u, P denotes the particle velocity and the acoustic pressure. Besides, the transfer function $\mathbf{T}_{\text{all}}$ of all sections of the ductwork system be solved by:

$$\mathbf{T}_{\text{all}} = \begin{bmatrix} 1 & 0 \\ \frac{1}{Z_1} & 1 \end{bmatrix} \mathbf{T}_{\text{duct}} \begin{bmatrix} 1 & 0 \\ \frac{1}{Z_2} & 1 \end{bmatrix} \mathbf{T}_{\text{duct}} \cdots \mathbf{T}_{\text{duct}} \begin{bmatrix} 1 & 0 \\ \frac{1}{Z_n} & 1 \end{bmatrix} \tag{4.14}$$

where Z_n represents the acoustic impedance of the *n*-th HR model. $\mathbf{T}_{\text{duct}}$ denotes the transfer function of the main duct section between each HR model, which can be represented by:

$$\mathbf{T}_{\text{duct}} = \begin{bmatrix} e^{-j\frac{kMa}{1-Ma^2}L} \cos \frac{kL}{1-Ma^2} & j e^{-j\frac{kMa}{1-Ma^2}L} \frac{\rho c}{S_d} \sin \frac{kL}{1-Ma^2} \\ j \frac{e^{-j\frac{kMa}{1-Ma^2}L}}{\rho c/S_d} \sin \frac{kL}{1-Ma^2} & e^{-j\frac{kMa}{1-Ma^2}L} \cos \frac{kL}{1-Ma^2} \end{bmatrix} \tag{4.15}$$

where L represents the length of the duct between each HR model.

The TL results of a periodic HRs array without grazing flow can be obtained by:

$$\mathrm{TL}_{Array} = 20\log_{10}\left|\frac{1}{2}\left(T_{11} + T_{12}S_n/\rho c + T_{21}\rho c/S_n + T_{22}\right)\right| \tag{4.16}$$

Therefore, the TL of a periodic HR array under grazing flow conditions could be solved by:

$$\mathrm{TL}(f + \Delta f - f_0) = \mathrm{TL}_{Array}(f) - n \cdot (l_n U)\mathrm{TL}_f(f) \tag{4.17}$$

In this study, a periodic HRs array model has been installed in the flow duct system to test the TL results under different flow speeds. The periodic HR model consists of 3 single resonators, all of which share the same geometric parameters as the model described in Chapter 4.2. L denotes the distance between each HR model. In this study, L is set as 100 mm.

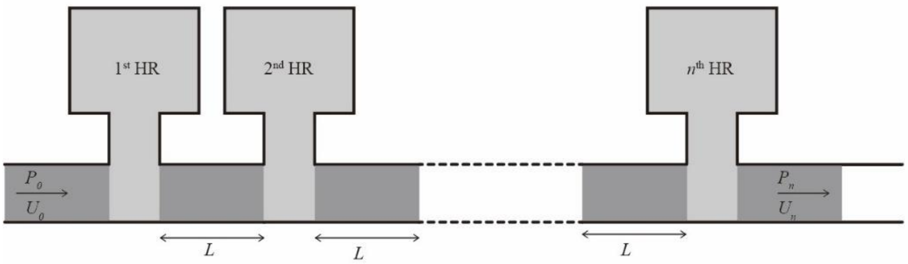

Figure 4.7 A ductwork system with periodic HRs array systems.

Figures 4.8 (a)-(e) present the results of transmission loss from theoretical predictions and experimental data for a periodic HRs array at various grazing flow rates ranging from 4 m/s to 20 m/s. Comparing Figure 4.8 and Figure 4.6, using the periodic HR array can increase the TL performance by improving the TL peak and expanding the bandwidth of the noise attenuation results. Besides, it could be observed that the experiment results fit well with formula prediction, which means Equation (4.17) could be utilized to predict the TL performance under different flow speeds. However, discrepancies exist at the resonance peak in Figure 4.8 (d) and (e). The experiment TL peaks are always lower than the formula prediction. These phenomena are mainly due to the limitation of measurement. As indicated by Oh and Jeon(Oh and Jeon, 2022), if the TL results are too high, the acoustic signals at the downstream side of the main duct would be buried in the background noise. Therefore, the experimental results have plateaus at the frequency range between 295-340Hz due to the background noise of the high-speed grazing flow.

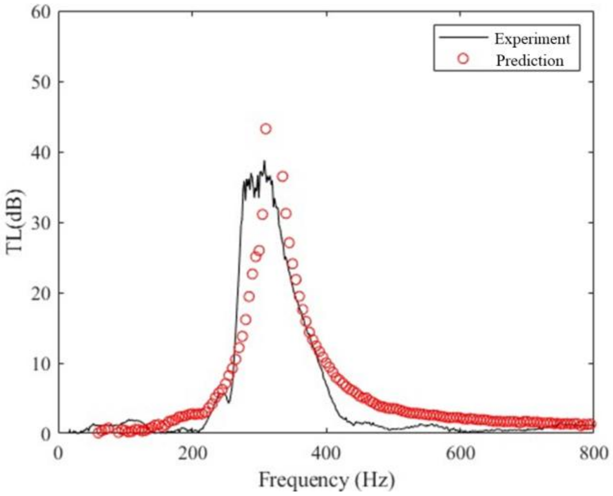

(a)

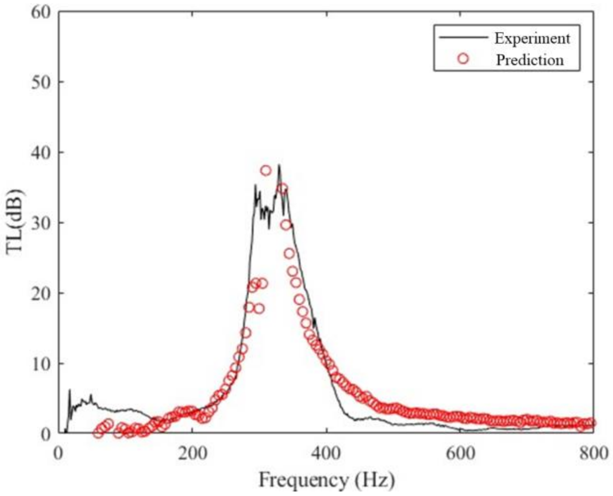

(b)

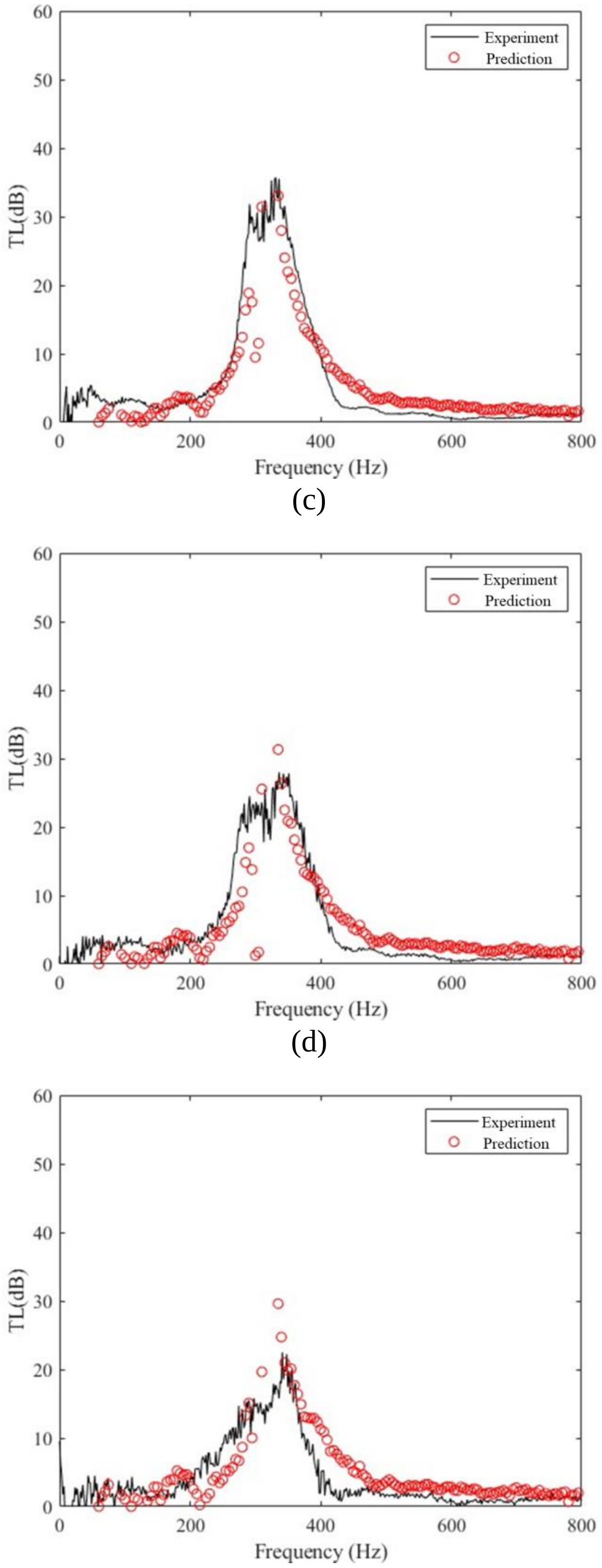

(c)

(d)

(e)

Figure 4.8 Transmission loss results between theoretical prediction and experiment result of a periodic HR array.

4.4.2 Effects of the grazing flow

To deepen our understanding of the fluid dynamics of the flow over the HR model, a PIV experiment is performed to capture the fluid characteristics near the neck region under varying grazing flow rates. Figure 4.9 illustrates the arrangement of the experiment setup employed for the flow field measurements of the HR model. The test rig used in part II is placed in a darkroom to finish the measurement procedure of the PIV experiment.(Li, Mak, Wai Ma, *et al.*, 2021) The Di-Ethyl-Hexyl-Sebacate (DEHS) oil droplets are utilized as tracers for this study. These droplets are generated using a particle seeding generator (10F03). The middle plane of the HR model is illuminated using a YAG laser system, which has a total energy of 50 mJ and a wavelength of about 500 nm. The internal cylindrical lenses of the laser system are adjusted to generate a light sheet that has a total thickness of 2 mm. A high-image-density CCD camera (Dantec Speedsence M140) with a resolution of 2560×1600 pixels is positioned 800 mm in front of the test region to capture the seeded airflow patterns. The camera records a series of 900 consecutive images of the seeded flow at a rate of 30 Hz. To determine the time-averaged velocity fields, a standard PIV cross-correlation algorithm is employed, which includes distortion correction, window offset, and sub-pixel recognition in the Dynamic Studio software. The detailed experimental procedure can be referenced in Li *et al.*'s study (Li, Mak, Ma, *et al.*, 2021). The size of the interrogation window is configured to 16×16 pixels with an overlap value of 50%, resulting in a test grid of velocity vectors spaced at intervals of 1.6×1.6 mm. The errors in the PIV test can be categorized into systematic errors and statistical errors, which collectively contribute to an overall velocity field error of less than 3.5%.

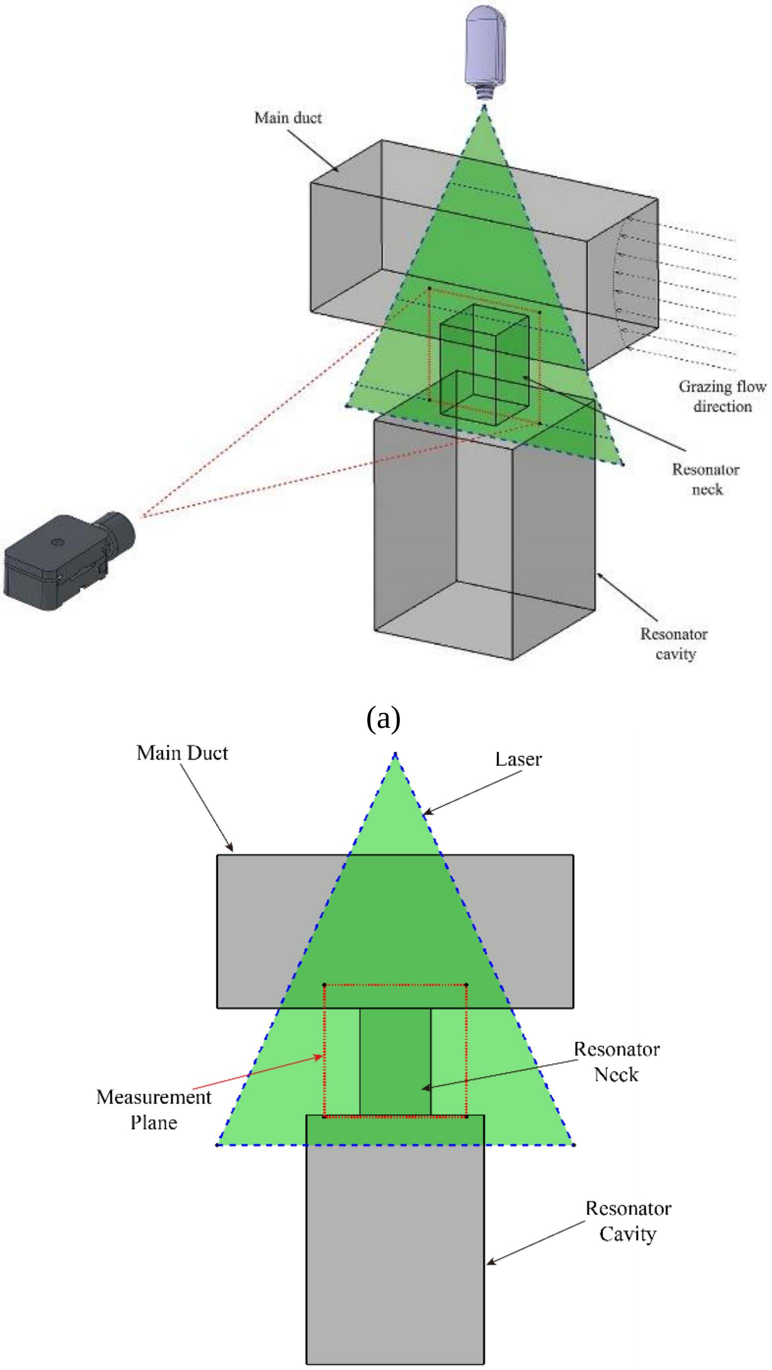

(a)

(b)

Figure 4.9 Illustration of the PIV measurement for the flow field of the HR model.

Figure 4.10 (a) to (c) shows the measurement result of the time-averaged velocity field near the neck region of the HR model when the average grazing flow speeds in the main duct are 4 m/s, 8 m/s and 12 m/s, respectively. The velocity direction is shown by the black arrows. It can be seen that the flow patterns are similar under different flow speeds. A uniform, high-speed grazing flow can be shown in the main duct, while the low-speed region is shown in the resonator neck. As the grazing flow speed rises, the average flow speed inside the neck region is also increased. A shear layer emerges at the connecting place of the main duct and the neck region of the HR, and the shear layer area also increases as the grazing flow speed increases.

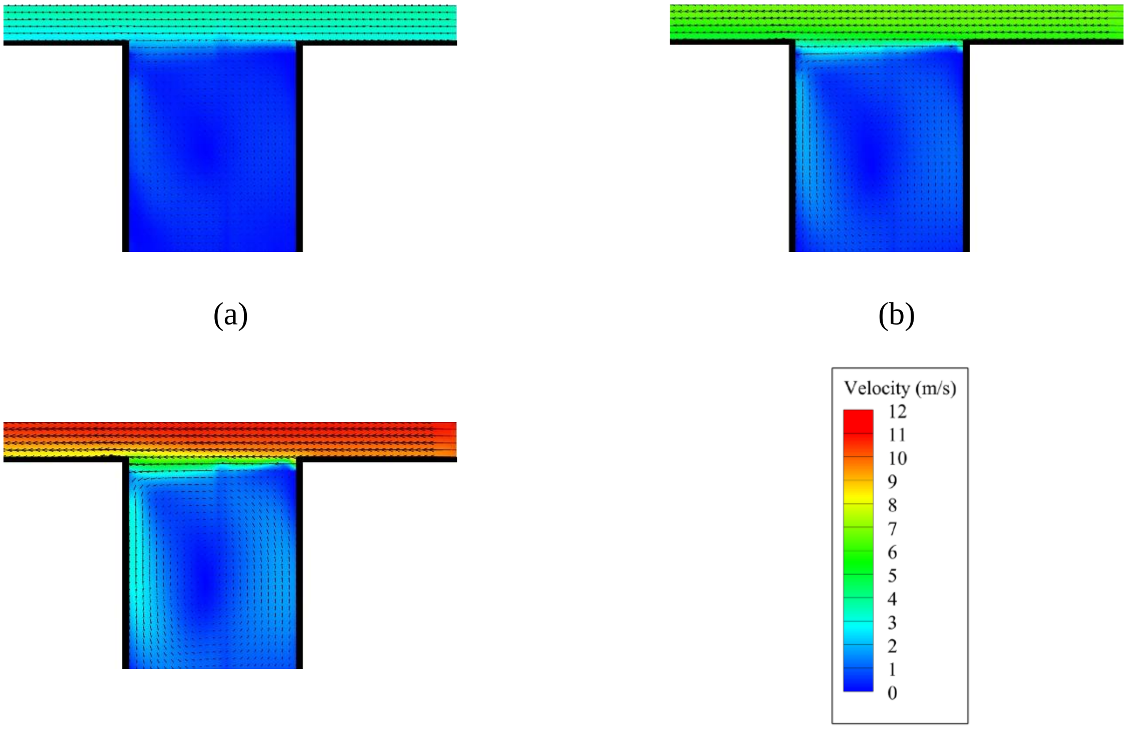

(a)

(b)

(c)

Figure 4.10 Flow field near the neck region of the HR model under different grazing flow speeds (a) U=4m/s, (b) U=8m/s, (c) U=12m/s.

Figure 4.11 (a) to (c) illustrates the vorticity magnitude distributions near the neck region of the HR model when the grazing flow rates inside the main duct are from 4 m/s to 12 m/s, respectively. A high vorticity region appears at the upstream and downstream side of the connection area between the neck and main duct. The emergence of vorticity is closely related to the interaction of the sound waves and the shear layer at the neck region (Li and Choy, 2024). As the grazing flow speed increases, the interaction becomes stronger, which leads to a vorticity increase inside the neck region. According to Li and Choy (Li and Choy, 2024), the shear layer can increase the dissipation rate of the acoustic energy. Besides, the shear layer can decrease the resistance of the mufflers. Therefore, as the grazing flow rate increases, the noise attenuation ability of the HR model decreases due to the increase in the total area of the shear layer.

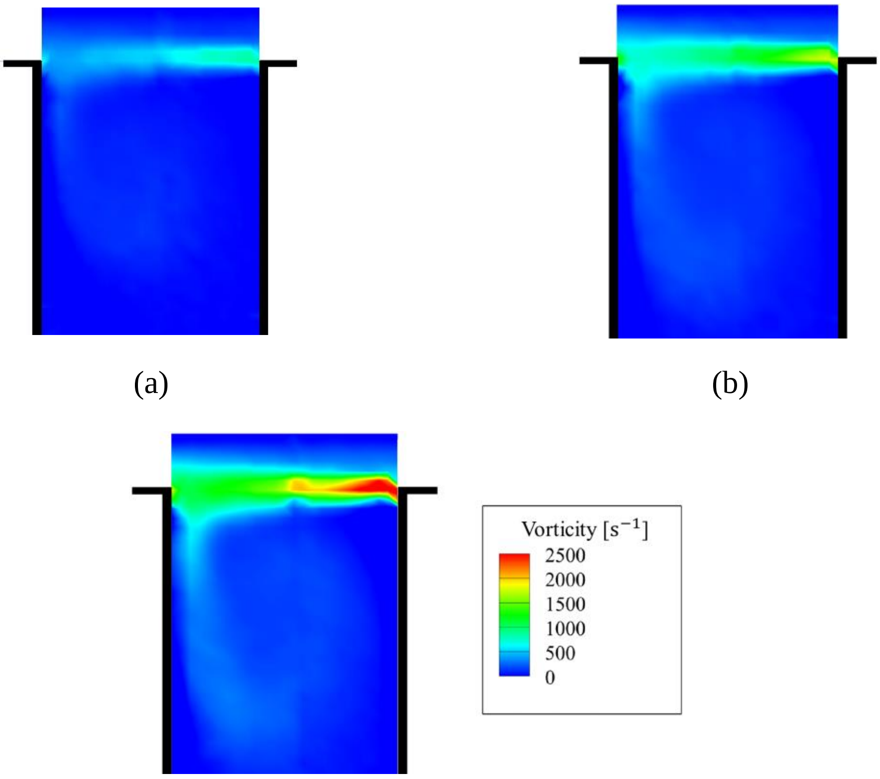

(c)

Figure 4.11 Vorticity distribution near the neck region of the HR model under different grazing flow speeds (a) U=4m/s, (b) U=8m/s, (c) U=12m/s.

4.5 Summary

Understanding the acoustic response and flow field characteristics of the HR model is crucial for designing the muffler under grazing flow conditions. This chapter presents an experimental study of the transmission loss results of a single HR model under grazing flow conditions. Besides, a PIV measurement experiment has been performed to analyze the fluid dynamics of the neck region of the HR model.

An empirical formula is proposed to estimate the sound transmission loss performance of the HR model under different grazing flow speeds. The non-dimensional TL correction term has been fitted from measurement data to predict the TL correction term. The proposed empirical formula has been utilized to predict the TL results of the HR model across a grazing flow speed range of 0 to 20 m/s.

The fluid dynamics of the neck region of the HR model under different flow speeds are investigated experimentally. With the increment of the grazing flow rate, the transmission loss performance of the HR model decreases due to the increase in the shear layer area.

The empirical formula is utilized to predict the TL results of the periodic HRs array model under grazing flow conditions. The formula used in this study could improve the accuracy of predictions for the noise absorption results of the mufflers derived from the HR model.

Chapter 5

Broadband low-frequency noise attenuation of a Helmholtz resonator array

5.1 Introduction

Over the last few years, the Acoustic Metamaterial (AM) has emerged as a fascinating way to control sound waves under low-frequency ranges. The term ‘acoustic metamaterial’ typically refers to artificial materials composed of small structures that could manipulate sound waves. The development of AM inspires researchers to develop various functional devices across multiple research fields, such as urban noise control (Kim and Lee, 2014), acoustic levitation (Memoli *et al.*, 2017), acoustic focusing, and acoustic stealth (Yu *et al.*, 2021). Among these applications, many Sound-Absorbing MetaMaterial (SAMM) have been fabricated to reduce low-frequency noise. In contrast to traditional SAMs, SAMMs are characterized by their lightweight and compact nature, providing the advantage of space-saving. Besides, HVAC duct systems often encounter challenges related to constrained spaces, and traditional SAMs are bulky in the low-frequency range. As a result, SAMMs have emerged as a useful way to control low-frequency noise in the HVAC duct systems of modern buildings.

As summarized by Gao *et al.* (Gao *et al.*, 2022), SAMMs can be classified into four types: pre-stressed membranes (Allam, Elsabbagh and Akl, 2017), thin plates (Fang *et al.*, 2022), labyrinth structures (Li and Assouar, 2016; Pavan and Singh, 2024), and Helmholtz Resonator (HR) based absorbers (Gao *et al.*, 2022). Among these structures, HR has simple geometric structures and is easy to manufacture and maintain (Cai, Mak and Wang, 2017; Cai and Mak, 2018b), and therefore becomes an effective strategy for low-frequency noise attenuation. HR is comprised of a cavity that is connected to the main duct with the neck, enabling attenuation of sound waves through the resonance effect. Huang *et al.* proposed constructing a SAMM built by an HR with the embedded neck as an acoustic tunable absorber capable of achieving perfect absorption (Huang *et al.*, 2019). Ryoo and Jeon developed a SAMM consisting of a two-dimensional array constructed by four HRs and investigated the absorption spectra through an equivalent fluid model (Ryoo and Jeon, 2018). Guo *et al.* (Guo *et al.*, 2020) reported a SAMM constructed by HR with spiral extended necks to reduce low-frequency noise. However, HR-based SAMMs exhibit local resonance, leading to significant dispersion that greatly restricts the effective bandwidth.(Cai and Mak, 2016; Zhou *et al.*, 2022).

To enhance the broadband noise attenuation capabilities of HR-based SAMMs, the common approach is to cascade-couple the HR in both lateral and vertical directions to construct an array. Guo et al developed an HR-based AM with multi-layer mufflers and optimized the noise attenuation performance in the low-frequency range. (Guo, Zhang, *et al.*, 2021). Besides, they investigated the influence of the open-area ratio of HR and the multi-layer effect. They also designed an inhomogeneous HR with an Embedded Neck (HREN) array with multiple perforations to achieve broadband sound absorption (Guo, Fang, Qu, *et al.*, 2021). Ryoo *et al.* (Ryoo, Yong Lee and Jeon, 2024) used an artificial neural network to design an AM consisting of HR installed on the MPP to reduce noise between 380-790 Hz. Duan *et al.* (Duan *et al.*, 2021) applied multi-layer HR to design an absorber with multiple absorption peaks. Mei *et al.* (Mei *et al.*, 2024) proposed a parallel-coupled absorber constructed by two layers: one of HREN and another of segmented neck HR. This design enables to choose noise attenuation range due to the different resonance peaks. These implementations of cascade-coupled HR-based SAMMs present a promising solution for sound attenuation in ductwork systems.

Recently, the development of HRs-based SAMMs has drawn researchers' attention to designing acoustic liners for their potential to control low-frequency noise in ductwork systems (Hasan, 2023; Li *et al.*, 2024; Liu *et al.*, 2024; Zhang *et al.*, 2024). Oh and Jeon proposed a metaliner consisting of two different HRs to insulate the duct noise under different grazing flow speeds (Oh and Jeon, 2022). Guo *et al.* (Guo, Fang, Jiang, *et al.*, 2021) studied the noise attenuation properties of an acoustic muffler consisting of HRENs in a frequency range between 700-1000 Hz under grazing flow conditions. The results showed that the designed metaliner had effective noise attenuation ability in flow conditions. Huang *et al.* (Huang *et al.*, 2021) presented a metaliner build up by a perforated plate with an HREN array to enhance the broadband sound absorption in the ductwork systems. This kind of metaliner is able to attenuate the acoustic wave in a broadband frequency between 700-3000 Hz with and without grazing flow. However, there is still limited discussion on the noise attenuation performance of metaliners under grazing flow conditions. Inspired by these studies of SAMMs, this chapter will design an HR-based SAMM for broadband low-frequency noise control of the HVAC duct systems.

5.2 Acoustic absorption coefficient of the HREN

This section outlines the design of both single-layer and double-layer Helmholtz resonators with embedded necks (HREN) and provides a theoretical formula to predict its sound absorption analytically. In Figure 5.1(a), the proposed double-layer HREN is cascade-coupled by two single-layer HRENs with the same cavity radius r_c. The embedded neck can decrease the weight of the whole structure (Huang *et al.*, 2019). Compared to a single-layer HREN, the extra layer can provide an extra resonance frequency. Therefore, this kind of design features a high-efficiency sound absorption ability.

5.2.1 Theoretical prediction model

The equivalent fluid model developed by Stinson has been widely adopted to investigate the acoustic wave propagation inside the sub-wavelength scale structures (Stinson, 1991). The efficacy of this model in predicting the sound absorption coefficient of the AM has been validated in previous studies. (Ryoo and Jeon, 2018; Guo *et al.*, 2020; Ryoo, Yong Lee and Jeon, 2024). In addition to the equivalent fluid model, some semi-empirical models have been proposed to describe the acoustic performance of the orifice under flow conditions (Elnady and Boden, 2003). In this study, Guess's semi-empirical model will be utilized to determine the acoustic impedance of the HREN (Guess, 1975). This model calculates the resistance and reactance of each section of a resonator by taking into account the influences of viscous and thermal effects. It was validated for acoustic structures whose dimensions are smaller than the wavelength ($ka \ll 1$), and grazing flow speed is less than 70 m/s (Seo, Kim and Kim, 2016, 2018).

The normalized specific impedance Z of each layer of the HREN can be divided into two parts, neck impedance Z_N and cavity impedance Z_{cav}:

$$Z = \frac{1}{\sigma}(Z_n + Z_{cav}) = \frac{1}{\sigma}(Z_v + Z_R + Z_{cav}) \tag{5.1}$$

where $\sigma = S_n/S_c$. S_n and S_c are neck area and cavity area. The neck impedance Z_n can be further divided into viscous and mass effect Z_v and radiation impedance Z_R, which can be calculated by:

$$Z_v = k\delta_v(2 + \frac{l_n}{r_n}) + j[k\delta_v(2 + \frac{l_n}{r_n})] \tag{5.2}$$

$$Z_R = kr_n^2 + j[k(l_n + (\frac{16r_n}{3\pi})\phi_I\phi_G)] \tag{5.3}$$

where $\delta_v = \sqrt{2v/kc}$ is the viscosity effect, c and ρ denote the sound speed and the density of air, v is the kinematic viscosity, l_n and r_n represent the length and the radius of the neck of the HREN, k is the wave number, ϕ_I and ϕ_G are end correction factor of the neck proposed by Ingard (Ingard, 1953) and Groeneweg (Groeneweg, 1969), which can be calculated by:

$$\phi_I = 1 - 1.41\sqrt{\sigma} \tag{5.4}$$

$$\phi_G = \frac{1+5\times10^3 M_0^2}{1+10^4 M_0^2} \tag{5.5}$$

where $M_0 = u_0/c$ is the dimensionless particle velocity at the neck region. u_0 can be determined by (Ingard and Ising, 1967):

$$u_0 = \frac{c\sigma}{1-\sigma^2}\left[\sqrt{\frac{1}{4} + 2(\frac{P_i(1-\sigma^2)}{\rho c^2 \sigma^2})} - \frac{1}{2}\right] \tag{5.6}$$

where P_i denotes the pressure amplitude of the incident sound wave.

The cavity impedance Z_{cav} can be calculated by:

$$Z_{cav} = -j\frac{S_n}{kV_\mathrm{c}} \tag{5.7}$$

where V_c is the volume of the cavity.

The Transfer Matrix Method (TMM) is utilized to compute the acoustic wave propagation inside the double-layer HREN. The transfer function of the double-layer HREN can be expressed as:

$$\mathbf{T}_{\mathrm{all}} = \begin{bmatrix} \mathrm{T}_{11} & \mathrm{T}_{12} \\ \mathrm{T}_{21} & \mathrm{T}_{22} \end{bmatrix} = \begin{bmatrix} 1 & 0 \\ (Z^1 + Z^2)/Z^1 Z^2 & 1 \end{bmatrix} \tag{5.8}$$

where Z^1 and Z^2 are the acoustic impedances of the *i*-th layer. Therefore, the total impedance can be determined by:

$$Z_{all} = \frac{\mathrm{T}_{11}}{\mathrm{T}_{21}} \tag{5.9}$$

After the total impedance is acquired, the absorption coefficient of the double-layer HREN model can be determined by using the following formula:

$$\alpha = 1 - \left|\frac{Z_{all}-1}{Z_{all}+1}\right|^2 \tag{5.10}$$

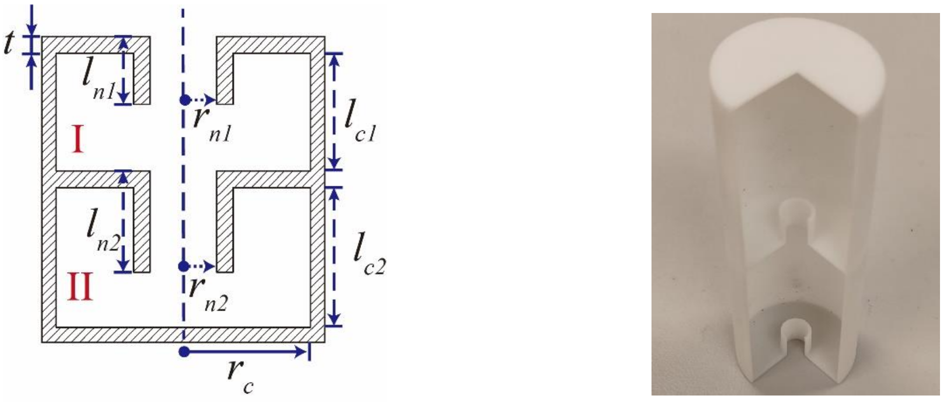

(a) (b)

Figure 5.1 (a) Illustration of the cross-sectional view of the double-layer HREN, (b) A 3D-printed model of the double-layer HREN

5.2.2 Experimental sound absorption

The B&K type 4206 impedance tube kit is utilized to test the absorption coefficient of the designed HREN. A pair of B&K type 4187 ¼ -inch microphones are connected to B&K data acquisition system (DAQ) module type 3052 to record the sound of each channel. The calculation of the absorption coefficient can be described as:

$$\alpha = 1 - \left|\frac{H_{ij}-e^{-jks}}{e^{jks}-H_{ij}}e^{2jk(s+d)}\right|^2 = 1 - |r|^2 \tag{5.11}$$

where r represents the reflection coefficient, k denotes the wave number, s represents the distance between two microphones, and d denotes the distance from the second microphone to the faceplate of the HREN. H_{ij} is the transfer function from the i-th channel to the j-th channel and can be calculated as $H_{ij} = S_{ij}/S_{ii}$, where S_{ij} is the cross-spectrum between the i-th channel and the j-th channel, and S_{ii} is the auto-spectrum of the i-th channel. The details of calculating S_{ij} and S_{ii} and H_{ij} can be found in international standard ISO 10534-2 ('ISO 10534-2:2023 - Acoustics — Determination of acoustic properties in impedance tubes — Part 2: Two-microphone technique for normal sound absorption coefficient and normal surface impedance', 2023). The arrangement of the test equipment can be found in Figure 5.2.

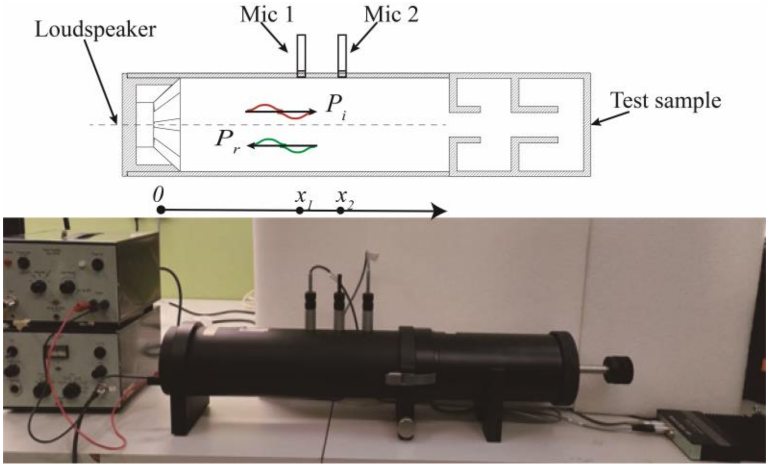

Figure 5.2 Absorption measurement of the double-layer HREN in an impedance tube.

Figure 5.1(b) shows the photographs of the double-layer HREN. The HREN is fabricated using a photopolymer resin that undergoes UV light curing at a wavelength of 405 nm, employing the Masked Stereolithography (mSLA) 3D printing method. The fabrication precision is 0.1 mm. The radii of the cavity r_c is 19mm. The neck length l_{n1} and l_{n2} are 10mm. The neck radius r_{n1} and r_{n2} are 4mm. The cavity lengths l_{c1} and l_{c2} are 55mm. The thickness t of the model is 1mm. In addition, the absorption result of a single-layer HREN is also evaluated. The geometry parameters of the single-layer HREN are the same as the first layer of the double-layer HREN.

Figure 5.3 displays the absorption coefficient result of the single-layer HREN and the double-layer HREN. The results demonstrate that analytical results fit well with the experimental measurements, indicating the high precision of the theoretical predictions. The resonance frequency of the single-layer HREN is approximately 406 Hz, whereas the resonance frequencies of the double-layer HREN are at 250 Hz and 658.5 Hz. By increasing the layer number of the HREN, the first resonance peak can reach a lower frequency. This result indicates that the low-frequency noise reduction of double-layer HREN is better than that of single-layer HREN. The theoretical model suggests that the interaction between each layer alters the acoustic impedance, leading to a decrease in the first resonance frequency. For the noise attenuation frequency band, the absorption bandwidth ($\Delta f_r/f_r$) (Huang *et al.*, 2019) of the single-layer HREN is 10.5%, while the absorption bandwidths of the first and the second resonance frequency of the double-layer HREN are 12.4% and 4.2%, respectively. The noise attenuation frequency band results indicate that increasing the layer number can be more suitable for broadband noise control. Several discrepancies can be noted between the theoretical predictions and experimental results, which are attributed to the gaps between the inner walls of the impedance tube and the 3D-printed model. Additionally, the loudspeaker is unable to produce a consistent white noise signal below 200 Hz, leading to a discrepancy in the absorption results between the tests and the theoretical prediction. However, it should be emphasized that the frequency range of interest in this study is above 200 Hz, allowing any inaccuracies below this threshold to be disregarded.

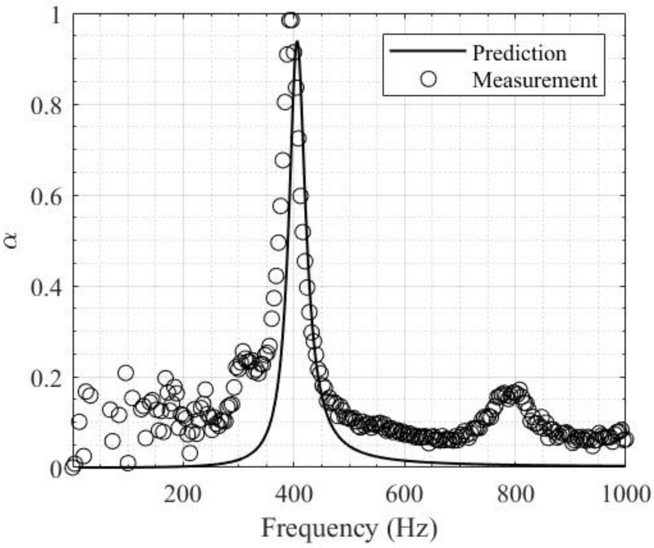

(a)

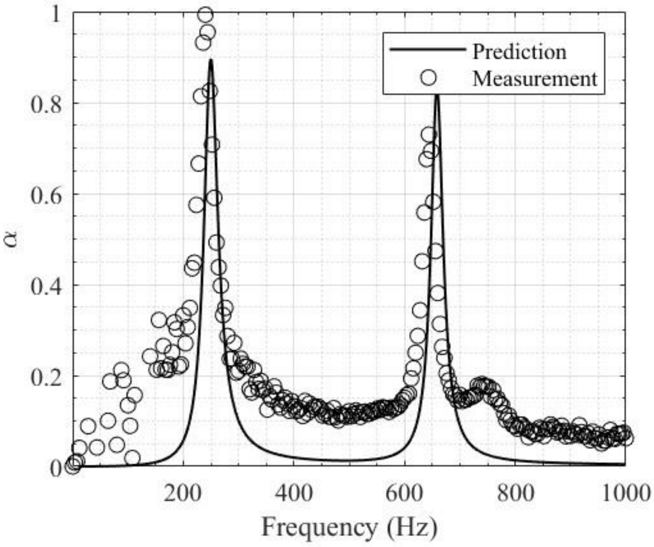

(b)

Figure 5.3 Predicted (solid lines) and measured (circles) results of the sound absorption coefficient of the HREN: (a) single-layer HREN, (b) double-layer HREN.

5.3 Optimization design of the Helmholtz resonator array

5.3.1 Optimization design strategy

The double-layer HREN exhibits a limited bandwidth due to its strong dispersion characteristic. In practical applications, the absorber with broadband noise attenuation ability is very attractive. However, the absorption bandwidth ($\Delta f_r/f_r$) of the proposed double-layer HREN in section 5.2 is not sufficient for practical applications. In this part, an optimization strategy is applied to design a Helmholtz resonator array (HRA) to achieve broadband low-frequency noise attenuation performance by using the single and double-layer HRENs arranged in an array. The geometric parameters are optimized to increase the sound absorption capacity within a specified frequency band. [f_{min}, f_{max}]. The objective function in the optimization process is set as:

$$\text{Max: } C_\alpha = \int \alpha df = \sum_{i=1}^{N_f} \alpha_i(f_i) \qquad (5.12)$$

where C_α is the sound absorption capacity(Cai and Mak, 2018c); N_f represents the number of the discrete frequencies within the specified frequency band; $\alpha_i(f_i)$ represents the sound absorption coefficient in the i-th discrete frequency f_i. The total acoustic impedance Z_{all}^{array} of all the double-layer HRENs in the array can be determined by:

$$\frac{S_{all}}{Z_{all}^{array}} = \sum_{N=1}^{M} \frac{S_N}{Z_{all}^{N}} \qquad (5.13)$$

where Z_{all}^{array} denotes the acoustic impedance of the array, S_{all} is the total area of the array, S_N is the area of each single HREN, Z_{all}^{N} represents the acoustic impedance of the

N-th HREN. Once Z_{all}^{array} has been obtained, the total sound absorption α can be determined by Equation (5.10).

The designed frequency range is chosen as 200 to 800 Hz. For the geometrical parameters, cavity radius r_c is fixed as 19mm, and thickness t is fixed as 1mm. Other geometry parameters are optimized and constrained as follows:

$$r_{n1}, r_{n2} \in [2.0, 6.0] \text{ mm}; \tag{5.14a}$$

$$l_{n1}, l_{n2} \in [5.0, 15.0] \text{ mm}; \tag{5.14b}$$

$$l_{c1}, l_{c2} \in [40.0, 80.0] \text{ mm}. \tag{5.14c}$$

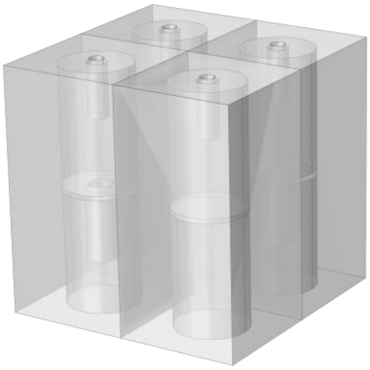

(a)

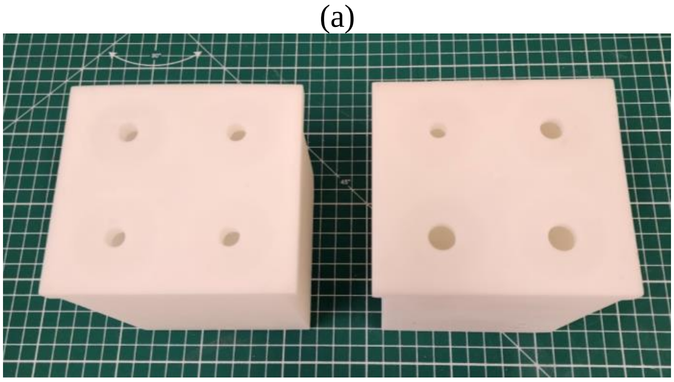

(b)

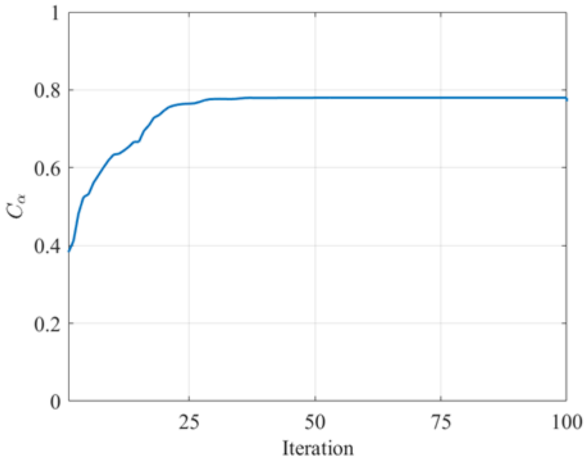

(c)

Figure 5.4 (a) Illustration of the design of the optimized HREN array. (b) Photograph of the optimized HRA model. (c) The iteration history of the optimization process.

Besides, the overall length of the array is set at 124 mm, which means that the final constraint is: $l_{c1} + l_{c2} + 3t \leq 124\,mm$. A MATLAB-based genetic algorithm (GA) package is utilized for the optimization process (Wang and Mak, 2018b, 2018a). To guarantee enough absorption bandwidth in the prescribed frequency range, a total of 8 HRENs are selected to construct the HRA. As shown in Figure 5.4 (b), the array is divided into two groups, and the HRENs are arranged vertically and horizontally within each group. Each HREN is installed in a 50mm × 50mm cell.

5.3.2 Optimization design results

Table 5.1 shows the parameters of each single cell in the HRA model. Besides, the theoretically calculated resonance frequency is also presented in Table 5.1. The optimized HRA is consisted of 6 double-layer HRENs and 2 single-layer HRENs. It is evident that the resonance frequencies of both layers are located in the optimization range of [200, 800] Hz. Figure 5.5(a) illustrates the normal sound absorption coefficient of the optimized array theoretically calculated by the GA program. For comparison purposes, the sound absorption results of the first four cells are selected to illustrate and compare with the array. The resonance frequency of each single cell is uniformly distributed in the prescribed frequency range. The photograph of the optimized array is displayed in Figure 5.4(b). It is clear that the designed array achieves effective sound absorption within the optimization range. Figure 5.4(c) shows the iteration history of the optimization process. It can be seen that after around 100 iteration steps, the total sound absorption capacity C_α of the optimized array is 0.78 in the designed frequency band.

Table 5.1 Parameters and resonance frequencies of each cell in the optimized HRA model.

Cell index N	r_{n1} (mm)	l_{n1} (mm)	r_{n2} (mm)	l_{n2} (mm)	l_{c1} (mm)	l_{c2} (mm)	Resonance Frequency 1 (Hz)	Resonance Frequency 2 (Hz)
1	4.5	9	3.5	11	60	46.9	238	537
2	4.5	9	3.5	11	46	60	213	601
3	4.5	9	-	-	53	-	469	-
4	4.5	9	3.9	9	46	50.4	271	683
5	6	5	3.8	5	77.5	42.4	316	671
6	6	5	4	5	70.6	40	348	722
7	4	7.9	-	-	44.3	-	400	-
8	5.1	5	3.2	5	75.7	44.3	261	578

Figure 5.5(b) illustrates the complex plane analysis of the optimized HRA. The black dashed line denotes the “real frequency” that is related to the actual sound absorption

conditions (Ding *et al.*, 2022), and the black circles represent the perfect absorption(Romero-García, Theocharis, Richoux, Merkel, *et al.*, 2016) of each cell. The contour indicates the variation of the sound reflection coefficient $|R|$ under different complex frequencies. In the lossless cases, $|R|$ displays a zero-pole pair that is symmetrical around the Re(*f*) axis (Romero-García, Theocharis, Richoux and Pagneux, 2016). In the realistic case, each zero-pole pair represents an absorption peak of each cell as presented in Figure 5.5(a). For each cell in the HRA, the zeros are shifted downward because of the energy loss resulting from visco-thermal losses in the neck region. All zeros are situated close to the real frequency line, indicating that high absorption of each cell can be achieved. In addition, the zeros are nearly uniformly distributed, suggesting that broadband absorption is attained.

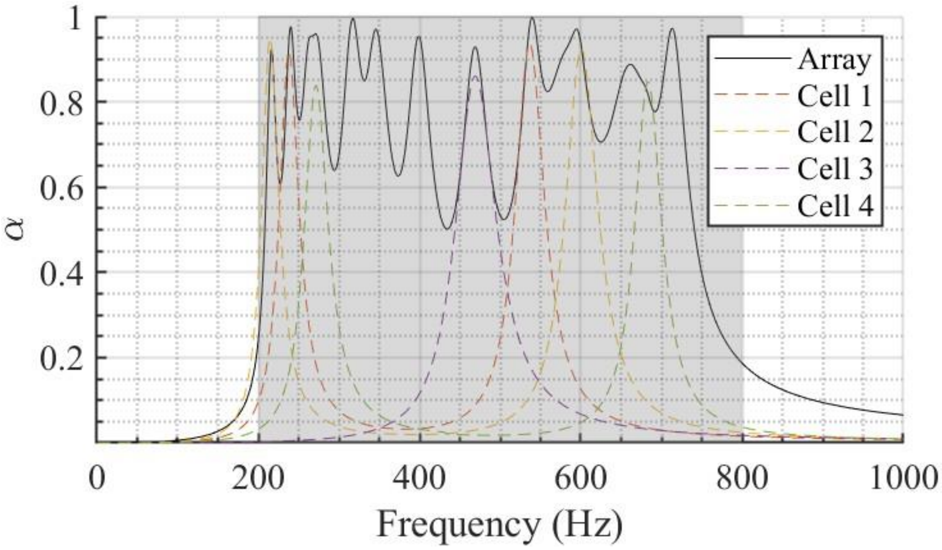

(a)

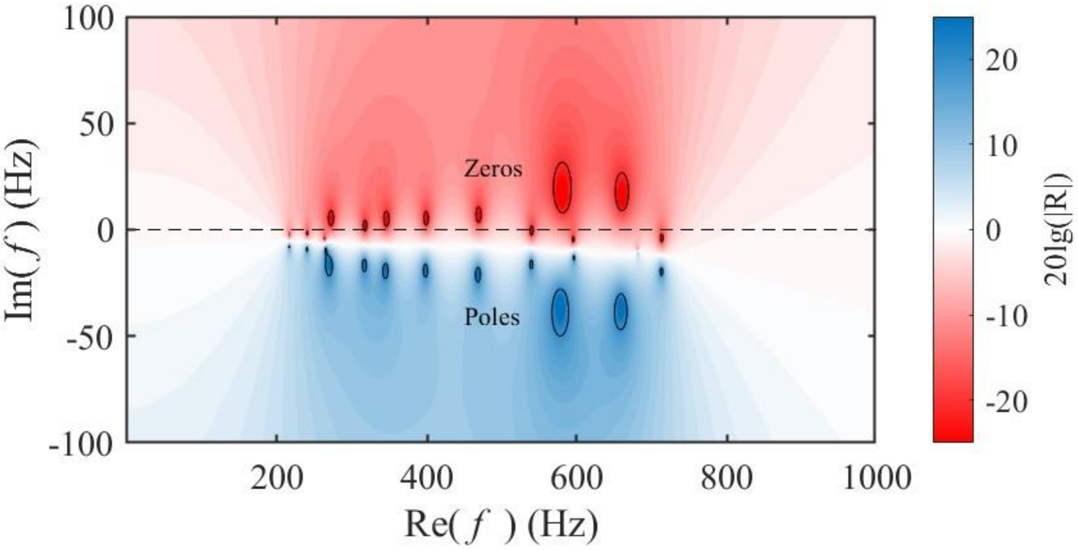

(b)

Figure 5.5 (a) Sound absorption performance of optimized HRA (black line), and the first four HREN cells (dashed lines). (b) Contour of 20lg($|R|$) of the optimized HRA in the complex frequency plane.

5.4 Acoustic performance in a ductwork system in the presence of grazing flow

5.4.1 Flow duct system and noise attenuation performance measurement

As shown in Figure 5.6, the side-branch mounted HRA is installed on the flow duct system for measuring the sound attenuation performance under grazing flow conditions. A centrifugal fan has been used to generate background grazing flow. The stable flow magnitude can be reached up to 20 m/s, which is the common flow rate in building acoustics for the HVAC duct design. White noise is generated by a B&K type 1405 signal generator and is produced by a loudspeaker (OPEL AP 6510C8). The sound power level

(SPL) is set as 115dB through a B&K type 2706 power amplifier. Two anechoic terminations are installed at both end sides of the main duct to reduce the reflected sound wave. The test section consists of three Plexiglas ducts, featuring square cross-sections with total dimensions of 100mm(*H*) ×100mm(*W*) ×1000mm(*L*). The HRA model is side-branch mounted on the middle duct of the test section. Two pairs of B&K type 4189-A-021 microphones are flush-mounted at the different sides of the test section to receive the acoustic pressure signals, and a B&K DAQ module 3160D is used to record the acoustic signal data.

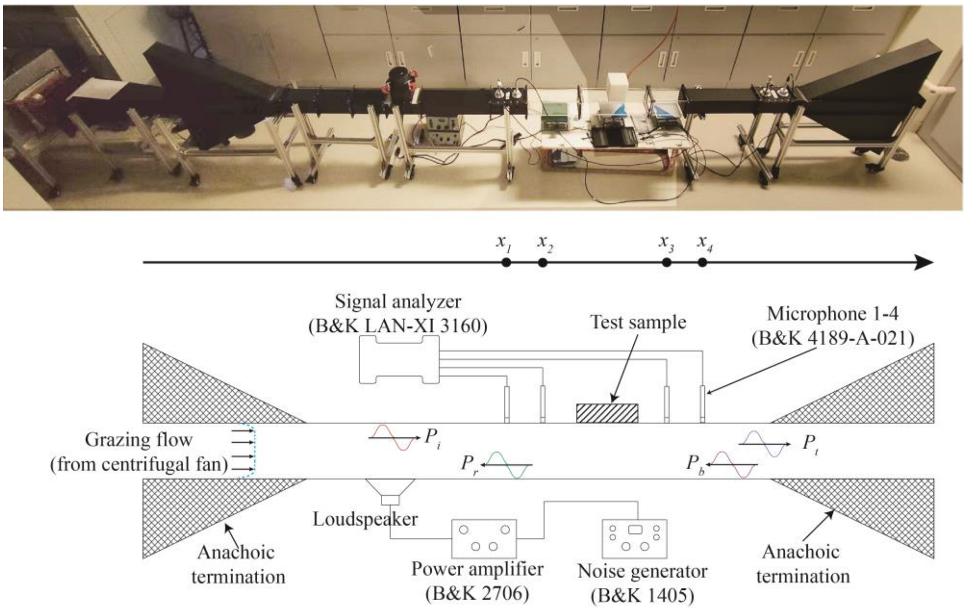

Figure 5.6. Sound transmission loss test in a grazing flow duct.

The four-microphone method is used to calculate the sound transmission loss per unit length (TL/L). At the same time, the absorption coefficient (α) of the side-branch mounted HRA is also calculated. After turning the acoustic pressure signal to the transfer function between each channel, TL/L and α can be calculated by (Wu and Wan, 1996; Guo, Fang, Jiang, *et al.*, 2021):

$$\mathrm{TL}/L = \frac{20}{L} lg\left|\frac{P_i}{P_t}\right| = \frac{20}{L} lg \left| \frac{H_{21} e^{j\frac{k}{1-M_x}x_2} - e^{j\frac{k}{1-M_x}x_1}}{H_{23} e^{j\frac{k}{1-M_x}x_4} - H_{24} e^{j\frac{k}{1-M_x}x_3}} e^{j\frac{2kM_x}{1-M_x^2}(x_3-x_1)} \right| \tag{5.15a}$$

$$\alpha = 1 - \left|\frac{P_i}{P_t}\right|^2 - \left|\frac{P_i}{P_r}\right|^2 \tag{5.15b}$$

where P_i and P_t are the pressure amplitudes of the incident sound wave and the transmitted sound wave, respectively. k is the axial wavenumber. $x_1 - x_4$ represent the axial position of four microphones. In this flow duct system, the distance between x_1 to x_2 and x_3 to x_4 are 100mm, while the distance between x_2 to x_3 is 1500mm. M_x is the flow Mach number.

Figure 5.7 (a) illustrates the measured sound absorption coefficient of the side branch mounted HRA without background grazing flow. Compared to Figure 5.5 (a), there is a reduction in the absorption coefficient when the HRA is switched from normal installation to side branch mounting. This result suggests that the sound absorption performance of the HRA is somewhat lower in practical applications than in experimental testing. In Figure 5.8 (b), the TL/L result indicates that the HRA model can maintain a high TL performance of more than 20 dB/m between the prescribed frequency band of 200 to 800 Hz. The results suggest that the designed HRA can be an effective absorber when installed in an operational HVAC duct system.

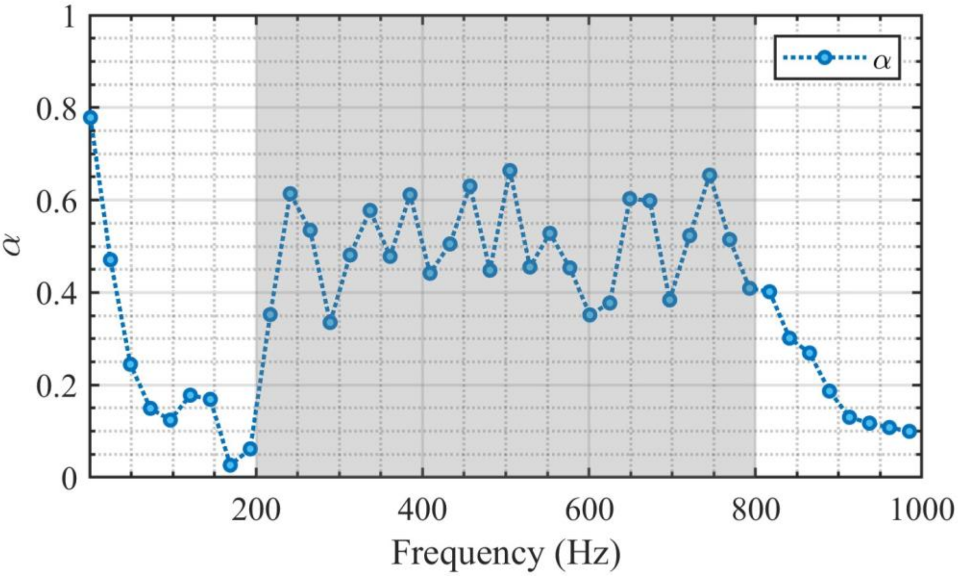

(a)

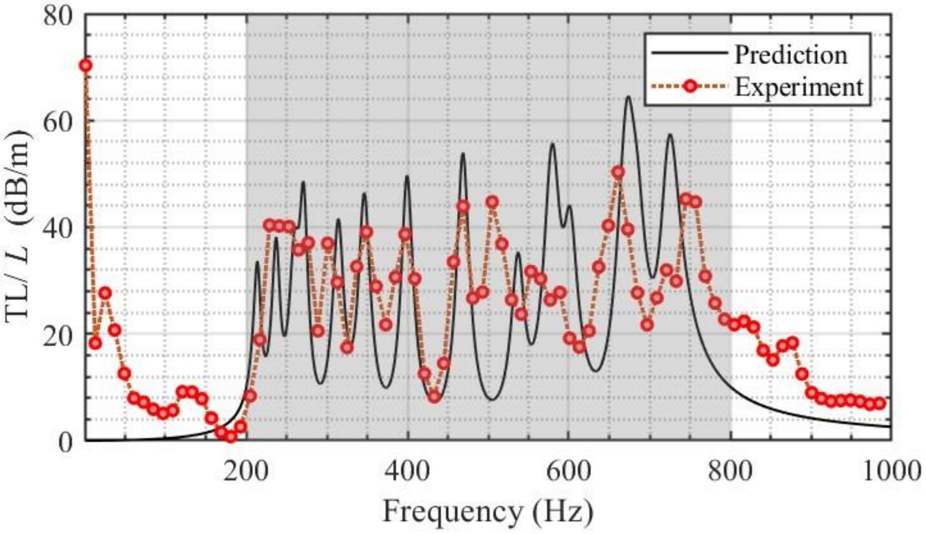

(b)

Figure 5.7 The acoustic performance of the side-branch mounted HRA model without grazing flow. (a) Sound absorption coefficient results. (b) Transmission loss spectra.

5.4.2 Acoustic performance of the HRA in the presence of grazing flow

A theoretical formula is presented here to calculate the TL/L results of the HRA under grazing flow conditions. According to Oh and Jeon (Oh and Jeon, 2022), the acoustic impedance of the HR model under different grazing flow conditions Z_{flow} can be influenced by adding a flow term:

$$Z_{flow} = Z'_{HR} + \frac{R_f}{\sigma} \tag{5.16}$$

where $R_f = M_x(\delta_v/2r_n)^{-0.2}/(2\beta^2)$ is the flow correction term, β is an empirical coefficient. Based on the research conducted by Seo *et al.*(Seo, Kim and Kim, 2018), $\beta = 3.64$ is a suitable value in our model. Z'_{HR} is the acoustic impedance in Equation (5.1) with a modification in radiation impedance Z_R:

$$Z'_{HR} = \frac{S_c}{S_n}(Z_v + \mathrm{Z}'_R + Z_{cav}) \tag{5.17a}$$

$$\mathrm{Z}'_R = kr_n^2 + j[k(l_n + (\frac{16r_n}{3\pi})\phi_I\phi_G\phi_R)] \tag{5.17b}$$

where $\phi_R = 1/305M_x^2$ is neck length correction owing to the grazing flow rate.

Equation (5.17) is utilized to compute the acoustic impedance of each layer of the HREN. Then, Equation (5.16), Equation (5.8), Equation (5.9) and Equation (5.13) are combined to calculate the total impedance of the HRA under grazing flow conditions. The TL per unit length results can be determined by:

$$\mathrm{TL}/L = \frac{20}{L} lg \left|1 + \frac{\rho c}{2S_{all}Z_{flow}}\right| \tag{5.18}$$

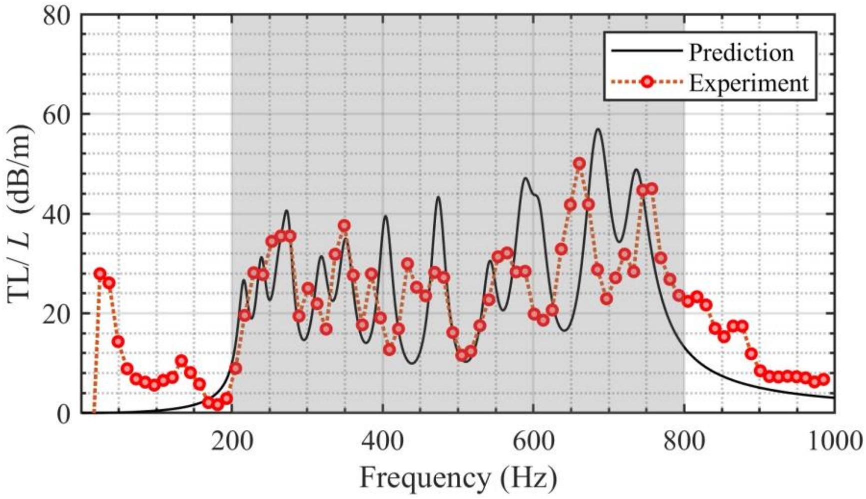

(a) U=5 m/s

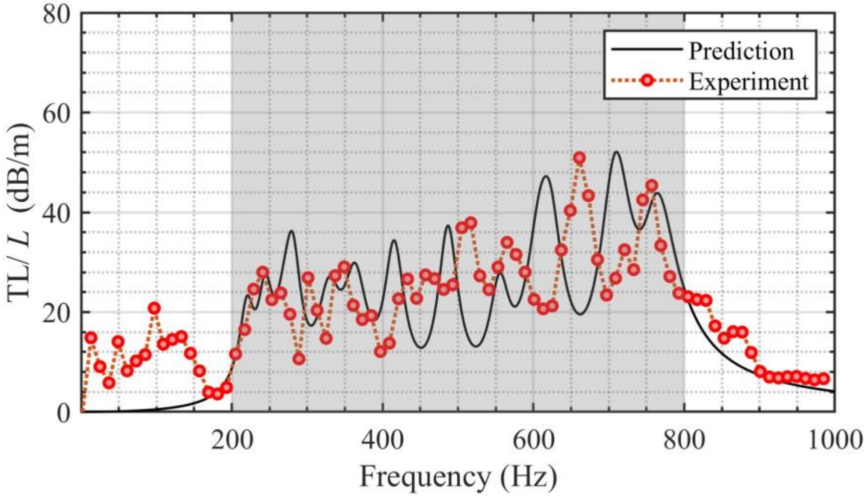

(b) U=10 m/s

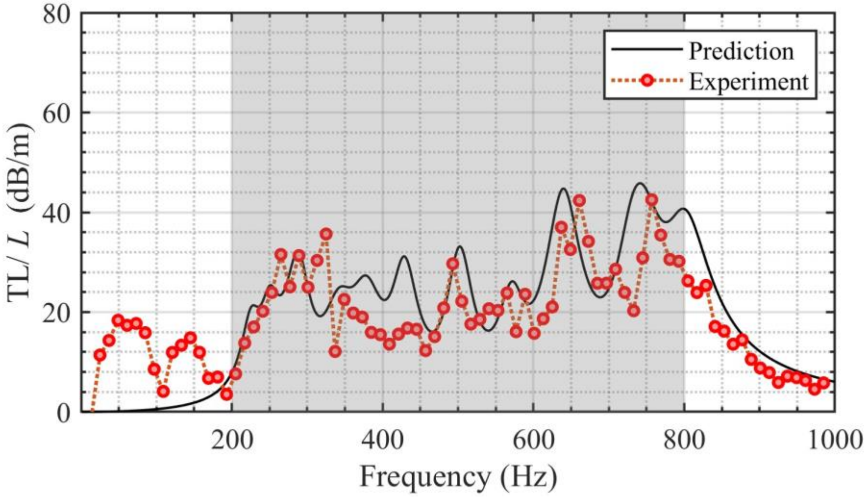

(c) U=15 m/s

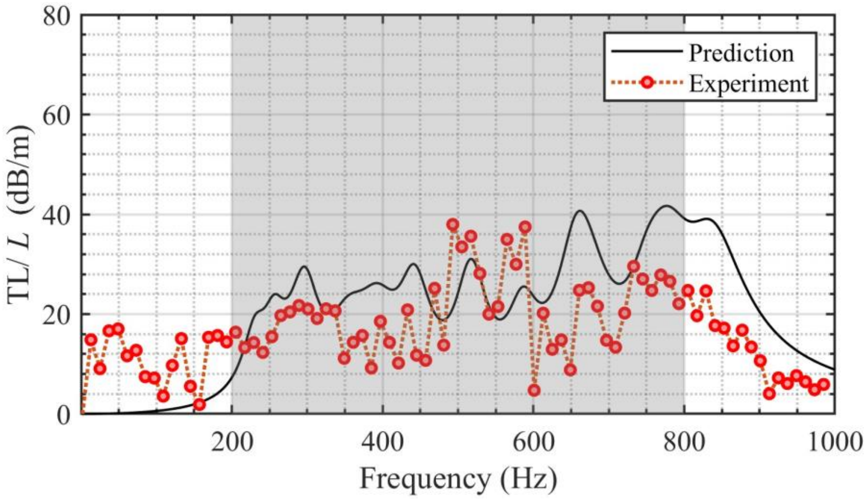

(d) U=20 m/s

Figure 5.8 Transmission loss performance of the side branch mounted HRA under different flow speeds. (a) U=5 m/s, (b) U=10 m/s, (c) U=15 m/s, (d) U=20 m/s.

Figures 5.8 (a)-(d) present the TL/L results at various grazing flow speeds: 5 m/s, 10 m/s, 15 m/s, and 20 m/s. The black solid lines illustrate the TL/L results derived from Equation (5.18), while the red dashed lines represent the measurement results. It is important to note that the loudspeaker used in this experiment is unable to generate a consistent white noise in the frequency range below 100 Hz. Therefore, the experimental TL/L data below 100 Hz are not available. The experimental TL/L results between the specified frequency bands of 200 to 800 Hz reasonably fit well with the analytical results from Equation (5.18). This indicates the effectiveness of incorporating a flow term modification in Equation (5.18) for accurately predicting the influence of grazing flow on the transmission loss results of the HRA model. The TL/L results can achieve around 20 dB/m between 200 to 800 Hz under 20 m/s grazing flow speeds, demonstrating that our optimized HRA can be an effective low-frequency broadband absorber.

5.5 Summary

In this chapter, we propose a Helmholtz Resonator Array (HRA) aiming at attenuating broadband low-frequency noise in the HVAC duct system under low-speed grazing conditions. The absorber is constructed by single and double-layer Helmholtz Resonator with Embedded Neck (HREN). A theoretical model is presented for determining the normal absorption coefficient of the designed HREN. The accuracy of the theoretical prediction is validated by experiments. An optimization process is employed to design an HRA with broadband low-frequency noise attenuation performance. The optimized HRA is composed of 8 single HRENs, and can achieve a sound absorption capacity of around 0.78 of the designed frequency band between 200 to 800 Hz. Then, the designed HRA is side branch mounted on a flow duct to investigate its noise attenuation performance under grazing flow conditions. A flow correction term has been added to the theoretical model to consider the effect of different grazing flow speeds on the transmission loss performance of the designed HRA. The results show that the proposed theoretical model can effectively predict the transmission loss performance of the HRA under different grazing flow conditions. The designed array can achieve around 20 dB/m of the prescribed frequency band between 200 to 800 Hz under flow speeds lower than 20 m/s, demonstrating that optimized HRA can be an effective low-frequency broadband absorber. The total work can provide a systematic procedure for designing metamaterial-based absorbers for the duct systems.

Chapter 6

Conclusion and Suggestions for Future Work

6.1 Conclusion

The HVAC ductwork system has become an essential part of modern buildings as it can provide fresh air to indoor environments. However, the ventilation ductwork system often becomes a significant noise source, as it can propagate low-frequency sound over long distances into the room. The traditional design strategy for duct silencers focused on static, no-flow conditions, overlooking the background grazing flow. Additionally, noise transmitted from the fan and flow-generated noise at duct discontinuities have been recognized as the primary noise sources in the ventilation ductwork system. Therefore, enhancing low-frequency noise attenuation performance in the ventilation ductwork system under grazing flow conditions is vital for improving the indoor acoustic environment. This thesis aims to use the Helmholtz resonators array to control low-frequency noise in the HVAC ductwork system in the presence of grazing flow. Experimental, analytical and numerical investigations are adopted to examine the fluid dynamics and acoustic performance of the Helmholtz resonator under various flow conditions.

First of all, a flow duct is designed and manufactured to investigate the acoustic and flow dynamic performance of the side-branch mounted HRs model under grazing flow conditions. This system enables a steady and silent background flow, with velocities ranging from 0 to 20 m/s, which is typical for building acoustics in ventilation ductwork design. Two anechoic terminations can attenuate 90% of the reflected acoustic wave between the frequency band of 50-1600 Hz, ensuring the correctness of the transmission loss measurement. The test section is constructed from an acrylic plate, allowing for effective flow visualization using particle image velocimetry.

Secondly, the noise attenuation performance of a dual HR system under different grazing flow conditions has been examined numerically. The study first examines the effect of neck length. The results indicate that both the second resonant frequency and the maximum transmission loss (TL_{max}) increase when the length of the second neck extends. In comparison to a single HR system, dual HR provides an additional TL peak and is more effective as noise mufflers under higher flow rate conditions. Modifying the cavity volume significantly affects the resonance frequency and TL_{max} at lower flow rates; however, it is less effective at higher flow rates. Acoustic pressure field results show that a secondary acoustic wave source emerges downstream of the neck. By increasing the grazing flow Mach number, TL_{max} of both peaks has been decreased, and the second resonance frequency increased. Transmission loss results reveal that the flow Mach number has a greater impact on the first TL peak than on the second. Velocity field analysis indicates that as the Mach number increases, more air enters the first cavity, resulting in a higher average velocity in that space, while the velocity magnitude within the second neck and cavity approaches zero.

Thirdly, the sound transmission loss performance of a single HR model has been investigated experimentally. A semi-empirical formula has been proposed to estimate the TL results of the Helmholtz resonator model under different grazing flow speeds. The non-dimensional transmission loss correction term is fitted from measurement data to determine the transmission loss correction term. The proposed semi-empirical formula has been applied to the prediction of the TL results of the single Helmholtz resonator model under the grazing flow speed range of 0-20 m/s. Besides, the semi-empirical formula has been used to predict the TL results of the periodic Helmholtz resonators array under different grazing flow speeds. The fluid dynamics of the neck region of the Helmholtz resonator model under different flow speeds are investigated experimentally. As the grazing flow speed increases, the sound attenuation performance of the HR model decreases due to the increase in the shear layer area.

Finally, a noise muffler consisting of a Helmholtz Resonator Array (HRA) has been proposed to reduce broadband low-frequency noise in the ductwork system under grazing flow conditions. The absorber consists of single and double-layer Helmholtz Resonators with Embedded Necks (HREN). A theoretical model is proposed to calculate the normal sound absorption coefficient of the designed HREN, and an experiment test is conducted to validate the theoretical model. An optimization process is employed to design an HRA capable of achieving effective broadband low-frequency noise attenuation. The optimized HRA comprises eight single HRENs and demonstrates a sound absorption capacity of approximately 78% across the target frequency range of 200 to 800 Hz. The designed

HRA is then side-branch mounted on a flow duct to evaluate its noise attenuation performance under grazing flow conditions. A flow correction term is incorporated into the theoretical model to predict the transmission loss result of the HRA under varying grazing flow rates. The results indicate that the theoretical model effectively predicts the TL results of the HRA under different grazing flow speeds. The designed array can achieve around 20 dB/m of the prescribed frequency band between 200 to 800 Hz under flow speeds lower than 20 m/s, demonstrating its effectiveness as a low-frequency broadband absorber. This work provides a systematic procedure for designing metamaterial-based absorbers for duct systems. The total work can provide a systematic procedure for designing metamaterial-based absorbers for the HVAC duct systems.

6.2 Recommendations for future study

Based on the current studies, several suggestions for future research are proposed as follows:

In Chapter 5, the Helmholtz resonator-based acoustic metamaterial has proven to be a useful method for reducing low-frequency noise. The ventilation ductwork systems are often located in constrained spaces, and acoustic metamaterial can achieve perfect absorption with a light and compact geometry. Therefore, acoustic metamaterial represents a prospective solution for controlling low-frequency noise in the HVAC duct system. However, existing studies seldom consider the grazing flow conditions in the design stage of the acoustic metamaterials. In this study, we have conducted both experimental and theoretical investigations into the noise attenuation ability of an HR-based acoustic metamaterial in the presence of grazing flow. Further research should be conducted to develop high-performance acoustic metamaterials for controlling low-frequency flow noise in HVAC duct systems.

In this research, time-averaged Particle Image Velocimetry (PIV) has been performed to measure the velocity field and vorticity distributions near the neck of the Helmholtz resonator. Research shows that vortex convection of the side-branch mounted structures is highly associated with the acoustic cycles of the oscillation of the shear layer. The experimental techniques need to be improved to finish a phase-averaged PIV measurement to discuss the acoustic response of a side-branch mounted Helmholtz resonator in a complete acoustic cycle. The results could help us to understand the sound production mechanisms of the shear layer, and enable us to develop a more accurate theoretical model for predicting sound attenuation characteristics in the Helmholtz resonator under grazing flow conditions.

References

Allam, A., Elsabbagh, A. and Akl, W. (2017) “Experimental demonstration of one-dimensional active plate-type acoustic metamaterial with adaptive programmable density”, *Journal of Applied Physics*, 121(12), p. 125106. Available at: https://doi.org/10.1063/1.4979020.

Alster, M. (1972) “Improved calculation of resonant frequencies of Helmholtz resonators”, *Journal of Sound and Vibration*, 24(1), pp. 63–85. Available at: https://doi.org/10.1016/0022-460X(72)90123-X.

Au Yeung, Y.N., Yiu, P.C.H. and Chow, W.K. (1996) “Active noise control: Evaluation in ventilation systems”, *Building Services Engineering Research and Technology*, 17(4), pp. 191–198. Available at: https://doi.org/10.1177/014362449601700404.

Bolt, R.H. (1947) “On the Design of Perforated Facings for Acoustic Materials”, *The Journal of the Acoustical Society of America*, 19(5), pp. 917–921. Available at: https://doi.org/10.1121/1.1916641.

Burgess, J.C. (1981) “Active adaptive sound control in a duct: A computer simulation”, *The Journal of the Acoustical Society of America*, 70(3), pp. 715–726. Available at: https://doi.org/10.1121/1.386908.

Cai, C. and Mak, C.M. (2016) “Noise control zone for a periodic ducted Helmholtz resonator system”, *The Journal of the Acoustical Society of America*, 140(6), pp. EL471–EL477.

Cai, C. and Mak, C.M. (2018a) “Acoustic performance of different Helmholtz resonator array configurations”, *Applied Acoustics*, 130, pp. 204–209. Available at: https://doi.org/10.1016/j.apacoust.2017.09.026.

Cai, C. and Mak, C.M. (2018b) “Hybrid noise control in a duct using a periodic dual Helmholtz resonator array”, *Applied Acoustics*, 134, pp. 119–124.

Cai, C. and Mak, C.M. (2018c) “Noise attenuation capacity of a Helmholtz resonator”, *Advances in Engineering Software*, 116, pp. 60–66. Available at: https://doi.org/10.1016/j.advengsoft.2017.12.003.

Cai, C., Mak, C.M. and Wang, X. (2017) “Noise attenuation performance improvement by adding Helmholtz resonators on the periodic ducted Helmholtz resonator system”, *Applied Acoustics*, 122, pp. 8–15.

Cambonie, T., Mbailassem, F. and Gourdon, E. (2018) “Bending a quarter wavelength resonator : Curvature effects on sound absorption properties”, *Applied Acoustics*, 131, pp. 87–102. Available at: https://doi.org/10.1016/j.apacoust.2017.10.004.

Carmona, J.C. and Alvarado, V.M. (2000) “Active noise control of a duct using robust control theory”, *IEEE Transactions on Control Systems Technology*, 8(6), pp. 930–938. Available a t: https://doi.org/10.1109/87.880596.

Catapane, G. *et al.* (2023) “Coiled quarter wavelength resonators for low-frequency sound absorption under plane wave and diffuse acoustic field excitations”, *Applied Acoustics*, 209, 109402. Available at: https://doi.org/10.1016/j.apacoust.2023.109402.

Červenka, M. and Bednařík, M. (2018) “Optimized reactive silencers with narrow side-branch tubes”, *The Journal of the Acoustical Society of America*, 144(4), pp. 2015–2021. Available at: https://doi.org/10.1121/1.5056175.

Červenka, M. and Bednařík, M. (2020) “Optimized compact wideband reactive silencers with annular resonators”, *Journal of Sound and Vibration*, 484, 115497. Available at: https://doi.org/10.1016/j.jsv.2020.115497.

Cummings, A. and Chang, I.-J. (1988) “Sound attenuation of a finite length dissipative flow duct silencer with internal mean flow in the absorbent”, *Journal of Sound and Vibration*, 127(1), pp. 1–17. Available at: https://doi.org/10.1016/0022-460X(88)90347-1.

Dai, X., Jing, X. and Sun, X. (2012) “Discrete vortex model of a Helmholtz resonator subjected to high-intensity sound and grazing flow”, *The Journal of the Acoustical Society of America*, 132(5), pp. 2988–2996. Available at: https://doi.org/10.1121/1.4757736.

Dastourani, H. and Bahman-Jahromi, I. (2021) “Evaluation of Aeroacoustic Performance of a Helmholtz Resonator System with Different Resonator Cavity Shapes in the Presence of a Grazing Flow”, *Journal of Aerospace Engineering*, 34(5), 04021061. Available at: https://doi.org/10.1061/(asce)as.1943-5525.0001309.

Ding, H. *et al.* (2022) “Broadband acoustic meta-liner with metal foam approaching causality-governed minimal thickness”, *International Journal of Mechanical Sciences*, 232, 107601. Available at: https://doi.org/10.1016/j.ijmecsci.2022.107601.

Du, L. *et al.* (2016) “Sound amplification at a rectangular T-junction with merging mean flows”, *Journal of Sound and Vibration*, 367, pp. 69–83.

Duan, H. *et al.* (2021) “Acoustic multi-layer Helmholtz resonance metamaterials with multiple adjustable absorption peaks”, *Applied Physics Letters*, 118(24), 241904. Available at: https://doi.org/10.1063/5.0054562.

Elnady, T. and Boden, H. (2003) “On Semi-Empirical Liner Impedance Modeling with Grazing Flow”, in *9th AIAA/CEAS Aeroacoustics Conference and Exhibit*. American Institute of Aeronautics and Astronautics, p. 3304. Available at: https://doi.org/10.2514/6.2003-3304.

El-Sharkawy, A.I. and Nayfeh, A.H. (1978) “Effect of an expansion chamber on the propagation of sound in circular ducts”, *The Journal of the Acoustical Society of America*, 63(3), pp. 667–674. Available at: https://doi.org/10.1121/1.381792.

EN ISO 5136:2009 - Acoustics - Determination of sound power radiated into a duct by fans and other air-moving devices (2009).

Fang, X. *et al.* (2022) “A nonlinear metamaterial plate for suppressing vibration and sound ra diation", *International Journal of Mechanical Sciences*, 228, 107473. Available at: https://doi.org/10.1016/j.ijmecsci.2022.107473.

Félix, F.B., Magalhães, M. de C. and Papini, G. de S. (2021) "An Improved ANC Algorithm for the Attenuation of Industrial Fan Noise", *Journal of Vibration Engineering & Technologies*, 9(2), pp. 279–289. Available at: https://doi.org/10.1007/s42417-020-00225-2.

Gao, N. *et al.* (2022) "Acoustic Metamaterials for Noise Reduction: A Review", *Advanced Materials Technologies*, 7(6), 2100698. Available at: https://doi.org/10.1002/admt.202100698.

Ghanadi, F. *et al.* (2015) "Analysis of the turbulent boundary layer in the vicinity of a self-excited cylindrical Helmholtz resonator", *Journal of Turbulence*, 16(8), pp. 705–728. Available at: https://doi.org/10.1080/14685248.2015.1024839.

Gikadi, J., Föller, S. and Sattelmayer, T. (2014) "Impact of turbulence on the prediction of linear aeroacoustic interactions: Acoustic response of a turbulent shear layer", *Journal of Sound and Vibration*, 333(24), pp. 6548–6559.

Groeneweg, J.F. (1969) "Current understanding of Helmholtz resonator arrays as duct boundary conditions", in *Basic Aerodynamic Noise Research, NASA SP-207*, pp. 357–368.

Guess, A.W. (1975) "Calculation of perforated plate liner parameters from specified acoustic resistance and reactance", *Journal of Sound and Vibration*, 40(1), pp. 119–137. Available at: https://doi.org/10.1016/S0022-460X(75)80234-3.

Guo, J. *et al.* (2020) "A compact low-frequency sound-absorbing metasurface constructed by resonator with embedded spiral neck", *Applied Physics Letters*, 117(22), 221902. Available at: https://doi.org/10.1063/5.0031891.

Guo, J., Fang, Y., Qu, R., *et al.* (2021) "An extra-broadband compact sound-absorbing structure composing of double-layer resonator with multiple perforations", *The Journal of the Acoustical Society of America*, 150(2), pp. 1370–1380. Available at: https://doi.org/10.1121/10.0005912.

Guo, J., Fang, Y., Jiang, Z., *et al.* (2021) "An investigation on noise attenuation by acoustic liner constructed by Helmholtz resonators with extended necks", *The Journal of the Acoustical Society of America*, 149, pp. 70–81.

Guo, J., Zhang, X., *et al.* (2021) "Wideband low-frequency sound absorption by inhomogeneous multi-layer resonators with extended necks", *Composite Structures*, 260, 113538. Available at: https://doi.org/10.1016/j.compstruct.2020.113538.

Hasan, Md.Z. (2023) "An experimental study on the sound transmission loss of dissimilar fuselage sandwich panels of turbojet aircraft", *Thin-Walled Structures*, 184, 110417. Available at: https://doi.org/10.1016/j.tws.2022.110417.

Ho Man Yu (2020) "Characteristics of Side-branch Array Aeroacoustics and Its Application in Low Mach Number Flow Duct Noise Control," The Hong Kong Polytechnic University.

Huang, S. *et al.* (2019) "Acoustic perfect absorbers via Helmholtz resonators with embedded apertures”, *The Journal of the Acoustical Society of America*, 145(1), pp. 254–262.

Huang, S. *et al.* (2021) “Broadband sound attenuation by metaliner under grazing flow”, *Applied Physics Letters*, 118(6), 063504.

Ih, J. and Lee, B. (1985) “Analysis of higher-order mode effects in the circular expansion chamber with mean flow”, *The Journal of the Acoustical Society of America*, 77(4), pp. 1377–1388. Available at: https://doi.org/10.1121/1.392029.

Ingard, U. (1953) “On the Theory and Design of Acoustic Resonators”, *The Journal of the Acoustical Society of America*, 25(6), pp. 1037–1061.

Ingard, U. and Ising, H. (1967) “Acoustic Nonlinearity of an Orifice”, *The Journal of the Acoustical Society of America*, 42(1), pp. 6–17. Available at: https://doi.org/10.1121/1.1910576.

“ISO 10534-2:2023 - Acoustics — Determination of acoustic properties in impedance tubes — Part 2: Two-microphone technique for normal sound absorption coefficient and normal surface impedance” (2023). Geneva, Switzerland.

Kim, H. and Selamet, A. (2020) “Effect of flow on a dual Helmholtz resonator”, *Journal of Mechanical Science and Technology*, 34(2), pp. 581–588. Available at: https://doi.org/10.1007/s12206-020-0106-7.

Kim, S.-H. and Lee, S.-H. (2014) “Air transparent soundproof window”, *AIP Advances*, 4(11), 117123. Available at: https://doi.org/10.1063/1.4902155.

Kinsler, L.E. *et al.* (1999) Fundamentals of Acoustics, 4th ed. New York: John Wiley & Sons Inc.

Larsson, M. *et al.* (2009) “A module-based active noise control system for ventilation systems, Part II: Performance evaluation”, *International Journal of Acoustics and Vibrations*, 14(4), pp. 196–206. Available at: https://doi.org/10.20855/ijav.2009.14.4250.

Lee, S.-H. and Ih, J.-G. (2003) “Empirical model of the acoustic impedance of a circular orifice in grazing mean flow”, *The Journal of the Acoustical Society of America*, 114(1), pp. 98–113.

Li, F. *et al.* (2022) “Adaptive active noise feedforward compensation for exhaust ducts using a FIR Youla parametrization”, *Mechanical Systems and Signal Processing*, 170, 108803. Available at: https://doi.org/10.1016/j.ymssp.2022.108803.

Li, H. *et al.* (2024) “Laminated acoustic metamaterials for low-frequency broadband ultra-strong sound insulation”, *Thin-Walled Structures*, 202, 112151. Available at: https://doi.org/10.1016/j.tws.2024.112151.

Li, X., Mak, C.M., Ma, K.W., *et al.* (2021) “Evaluating flow-field and expelled droplets in the mockup dental clinic during the COVID-19 pandemic”, *Physics of Fluids*, 33(4), 047111.

Li, X., Mak, C.M., Wai Ma, K., *et al.* (2021) “How the high-volume evacuation alters the flow-field and particle removal characteristics in the mock-up dental clinic”, *Building and Envir* *onment*, 205, 108225.

Li, Y. and Assouar, B.M. (2016) “Acoustic metasurface-based perfect absorber with deep subwavelength thickness”, *Applied Physics Letters*, 108(6), 063502. Available at: https://doi.org/10.1063/1.4941338.

Li, Y. and Choy, Y.S. (2024) “Acoustic behaviour of micro-perforated panel backed by shallow cavity under fully developed grazing flow”, *Journal of Sound and Vibration*, 569, 117985. Available at: https://doi.org/10.1016/j.jsv.2023.117985.

Liu, F. *et al.* (2008) “Acoustic energy harvesting using an electromechanical Helmholtz resonatora)”, *The Journal of the Acoustical Society of America*, 123(4), pp. 1983–1990. Available at: https://doi.org/10.1121/1.2839000.

Liu, Y. *et al.* (2024) “Ultra-thin ventilated metasurface pipeline coating for broadband noise reduction”, *Thin-Walled Structures*, 200, 111916. Available at: https://doi.org/10.1016/j.tws.2024.111916.

Lueg, P. (1936) “Process of silencing sound oscillations”, US patent.

Maa, D.-Y. (1998) “Potential of microperforated panel absorber”, *The Journal of the Acoustical Society of America*, 104(5), pp. 2861–2866. Available at: https://doi.org/10.1121/1.423870.

Mei, Z. *et al.* (2024) “Parallel-coupled hierarchical and reconfigurable structure for broadband sound absorption”, *Applied Acoustics*, 221, 109990. Available at: https://doi.org/10.1016/j.apacoust.2024.109990.

Memoli, G. *et al.* (2017) “Metamaterial bricks and quantization of meta-surfaces”, *Nature Communications*, 8(1), 14608. Available at: https://doi.org/10.1038/ncomms14608.

Miles, J. (1944) “The Reflection of Sound due to a Change in Cross Section of a Circular Tube”, *The Journal of the Acoustical Society of America*, 16(1), pp. 14–19. Available at: https://doi.org/10.1121/1.1916257.

Morse, P.M. (1939) “The Transmission of Sound Inside Pipes”, *The Journal of the Acoustical Society of America*, 11(2), pp. 205–210. Available at: https://doi.org/10.1121/1.1916024.

Morse, P.M. and Ingard, K.U. (1986) Theoretical Acoustics. Princeton University Press.

Nayfeh, A.H., Kaiser, J.E. and Telionis, D.P. (1975) “Acoustics of Aircraft Engine-Duct Systems”, *AIAA Journal*, 13(2), pp. 130–153. Available at: https://doi.org/10.2514/3.49654.

Neise, W. and Koopmann, G.H. (1980) “Reduction of centrifugal fan noise by use of resonators”, *Journal of Sound and Vibration*, 73(2), pp. 297–308. Available at: https://doi.org/10.1016/0022-460X(80)90697-5.

Oh, T.S. and Jeon, W. (2022) “Acoustic metaliners for sound insulation in a duct with little flow resistance”, *Applied Physics Letters*, 120(4), 044103.

Olny, X. and Boutin, C. (2003) “Acoustic wave propagation in double porosity media”, *The Journal of the Acoustical Society of America*, 114(1), pp. 73–89. Available at: https://doi.org/10.1121/1.1534607.

Olson, H.F. and May, E.G. (1953) “Electronic Sound Absorber”, *The Journal of the Acoustical Society of America*, 25(6), pp. 1130–1136. Available at: https://doi.org/10.1121/1.1907249.

Pavan, G. and Singh, S. (2024) “In-depth investigations into symmetrical labyrinthine acoustic metamaterial with two micro-slit entries for low-frequency sound absorption”, *The Journal of the Acoustical Society of America*, 155(1), pp. 496–510. Available at: https://doi.org/10.1121/10.0023962.

Rayleigh, L. (1916) “The Theory of the Helmholtz Resonator”, *Proceedings of the Royal Society of London, Series A*, 92(638), pp. 265–275.

Rohlfing, J. and Gardonio, P. (2014) “Ventilation duct with concurrent acoustic feed-forward and decentralised structural feedback active control”, *Journal of Sound and Vibration*, 333(3), pp. 630–645. Available at: https://doi.org/10.1016/j.jsv.2013.09.022.

Romero-García, V., Theocharis, G., Richoux, O., Merkel, A., *et al.* (2016) “Perfect and broadband acoustic absorption by critically coupled sub-wavelength resonators”, *Scientific Reports*, 6(1), 19519. Available at: https://doi.org/10.1038/srep19519.

Romero-García, V., Theocharis, G., Richoux, O. and Pagneux, V. (2016) “Use of complex frequency plane to design broadband and sub-wavelength absorbers”, *The Journal of the Acoustical Society of America*, 139(6), pp. 3395–3403. Available at: https://doi.org/10.1121/1.4950708.

Ryoo, H. and Jeon, W. (2018) “Dual-frequency sound-absorbing metasurface based on visco-thermal effects with frequency dependence”, *Journal of Applied Physics*, 123(11), 115110.

Ryoo, H., Yong Lee, K. and Jeon, W. (2024) “Broadband sound absorption using hybrid resonators with embedded necks and micro-perforations in parallel”, *Mechanical Systems and Signal Processing*, 211, 111205. Available at: https://doi.org/10.1016/j.ymssp.2024.111205.

Selamet, A. and Lee, I. (2003) “Helmholtz resonator with extended neck”, *The Journal of the Acoustical Society of America*, 113(4), pp. 1975–1985.

Selamet, A. and Radavich, P.M. (1997) “THE EFFECT OF LENGTH ON THE ACOUSTIC ATTENUATION PERFORMANCE OF CONCENTRIC EXPANSION CHAMBERS: AN ANALYTICAL, COMPUTATIONAL AND EXPERIMENTAL INVESTIGATION”, *Journal of Sound and Vibration*, 201(4), pp. 407–426. Available at: https://doi.org/10.1006/jsvi.1996.0720.

Seo, S.-H., Kim, Y.-H. and Kim, K.-J. (2016) “Transmission loss of a silencer using resonator arrays at high sound pressure level”, *Journal of Mechanical Science and Technology*, 30(2), pp. 653–660. Available at: https://doi.org/10.1007/s12206-016-0119-4.

Seo, S.-H., Kim, Y.-H. and Kim, K.-J. (2018) “Design of silencer using resonator arrays with high sound pressure and grazing flow”, *Applied Acoustics*, 138, pp. 188–198.

Shahzad, H., Hickel, S. and Modesti, D. (2023) “Turbulence and added drag over acoustic liners”, *Journal of Fluid Mechanics*, 965, A10. Available at: https://doi.org/10.1017/jfm.2023.397.

Shi, X. (2016) A study of the effect of periodic structure on the attenuation performance of the mufflers. Hong Kong Polytechnic University.

Shi, X. and Mak, C.M. (2015) “Helmholtz resonator with a spiral neck”, *Applied Acoustics*, 99, pp. 68–71.

Spillere, A., Cordioli, J.A. and Boden, H. (2017) “On the Effect of Boundary Conditions on Impedance Eduction Results”, in *23rd AIAA/CEAS Aeroacoustics Conference*. American Institute of Aeronautics and Astronautics (AIAA AVIATION Forum). Available at: https://doi.org/10.2514/6.2017-3185.

Stewart, G.W. (1945) “The Theory of the Herschel-Quincke Tube”, *The Journal of the Acoustical Society of America*, 17(2), pp. 107–108. Available at: https://doi.org/10.1121/1.1916304.

Stinson, M.R. (1991) “The propagation of plane sound waves in narrow and wide circular tubes, and generalization to uniform tubes of arbitrary cross-sectional shape”, *The Journal of the Acoustical Society of America*, 89(2), pp. 550–558. Available at: https://doi.org/10.1121/1.400379.

Sugimoto, N. (1992) “Propagation of nonlinear acoustic waves in a tunnel with an array of Helmholtz resonators”, *Journal of Fluid Mechanics*, 244, pp. 55–78. Available at: https://doi.org/10.1017/S0022112092002969.

Tonon, D. *et al.* (2011) “Aeroacoustics of pipe systems with closed branches”, *International Journal of Aeroacoustics*, 10(2–3), pp. 201–276. Available at: https://doi.org/10.1260/1475-472X.10.2+3.201.

Utley, W.A. and Mulholland, K.A. (1968) “The transmission loss of double and triple walls”, *Applied Acoustics*, 1(1), pp. 15–20. Available at: https://doi.org/10.1016/0003-682X(68)90004-2.

Wang *et al.* (2018) “A renewable low-frequency acoustic energy harvesting noise barrier for high-speed railways using a Helmholtz resonator and a PVDF film”, *Applied Energy*, 230, pp. 52–61. Available at: https://doi.org/10.1016/j.apenergy.2018.08.080.

Wang, C., Huang, L. and Zhang, Y. (2014) “Oblique incidence sound absorption of parallel arrangement of multiple micro-perforated panel absorbers in a periodic pattern”, *Journal of Sound and Vibration*, 333(25), pp. 6828–6842. Available at: https://doi.org/10.1016/j.jsv.2014.08.009.

Wang, G. *et al.* (2023) “Low-frequency broadband absorber with coherent coupling based on perforated panel and space-coiling channels”, *Journal of Physics D: Applied Physics*, 56(49), 495102. Available at: https://doi.org/10.1088/1361-6463/acf676.

Wang, P. *et al.* (2018) “Influence of vortex-excited acoustic resonance on flow dynamics in channel with coaxial side-branches”, *Physics of Fluids*, 30(9), 095105.

Wang, X. and Mak, C.M. (2012) “Acoustic performance of a duct loaded with identical resonators”, *The Journal of the Acoustical Society of America*, 131(4), pp. EL316–EL322. Available at: https://doi.org/10.1121/1.3691826.

Wang, Z. and Mak, C.M. (2018a) “Application of a movable active vibration control system on a floating raft”, *Journal of Sound and Vibration*, 414, pp. 233–244. Available at: https://doi.org/10.1016/j.jsv.2017.11.026.

Wang, Z. and Mak, C.M. (2018b) “Optimization of geometrical parameters for periodical structures applied to floating raft systems by genetic algorithms”, *Applied Acoustics*, 129, pp. 108–115. Available at: https://doi.org/10.1016/j.apacoust.2017.07.018.

Wu, L. *et al.* (2022) “Hybrid active and passive noise control in ventilation duct with internally placed microphones module”, *Applied Acoustics*, 188, 108525. Available at: https://doi.org/10.1016/j.apacoust.2021.108525.

Wu, T.W. and Wan, G.C. (1996) “Muffler Performance Studies Using a Direct Mixed-Body Boundary Element Method and a Three-Point Method for Evaluating Transmission Loss”, *Journal of Vibration and Acoustics*, 118(3), pp. 479–484. Available at: https://doi.org/10.1115/1.2888209.

Xu, M.B., Selamet, A. and Kim, H. (2010) “Dual Helmholtz resonator”, *Applied Acoustics*, 71(9), pp. 822–829. Available at: https://doi.org/10.1016/j.apacoust.2010.04.007.

Yang, M. and Sheng, P. (2023) “Acoustic metamaterial absorbers: The path to commercialization”, *Applied Physics Letters*, 122(26), p. 260504. Available at: https://doi.org/10.1063/5.0147941.

Yu, G. *et al.* (2021) “Underwater Acoustic Stealth by a Broadband 2-Bit Coding Metasurface”, *Physical Review Applied*, 15(6), 064064. Available at: https://doi.org/10.1103/PhysRevApplied.15.064064.

Yu, X., Cheng, L. and You, X. (2015) “Hybrid silencers with micro-perforated panels and internal partitions”, *The Journal of the Acoustical Society of America*, 137(2), pp. 951–962. Available at: https://doi.org/10.1121/1.4906148.

Zhang, X. *et al.* (2024) “Modular reverse design of acoustic metamaterial and sound barrier engineering applications: High ventilation and broadband sound insulation”, *Thin-Walled Structures*, 196, 111498. Available at: https://doi.org/10.1016/j.tws.2023.111498.

Zhou, Z. *et al.* (2022) “Broadband impedance modulation via non-local acoustic metamaterials”, *National Science Review*, 9(8), p. nwab171. Available at: https://doi.org/10.1093/nsr/nwab171.